Kinetic Modeling of Carbon Oxidation

by

Zhiyou Du

B.Eng. in Mechanical Engineering
Shanghai Jiao Tong University, Shanghai, PRC
(1982)

M.S. in Mechanical Engineering
Massachusetts Institute of Technology
(1985)

Submitted to the Department of Mechanical Engineering
in Partial Fulfillment of
the Requirements of the Degree of

Doctor of Science in Mechanical Engineering

at the
Massachusetts Institute of Technology

February 1990

Signature of Author _____
Department of Mechanical Engineering
Feb., 1990

Certified by_____
Adel F. Sarofim
Thesis Supervisor

Certified by_____
John P. Longwell
Thesis Supervisor

Certified by_____
James C. Keck
Chairman, Thesis committee

Accepted by_____
Ain A. Sonin
Chairman, Departmental committee on Graduate Students

Kinetic Modeling of Carbon Oxidation

by

Zhiyou Du

Submitted to the Department of Mechanical Engineering
in February 1990 in Partial Fulfillment of
the Requirements for the Degree of Doctor of Science
in Mechanical Engineering at the
Massachusetts Institute of Technology

Abstract

This study was undertaken to develop a comprehensive kinetic model for the carbon-oxygen reaction. To accomplish this, desorption as well as oxidation of two model carbon materials, uncatalyzed soot (ST1) and catalyzed soot (ST2), were systematically investigated by means of a thermogravimetric analyzer (TGA) and a mass spectrometer (MS).

It was found from the temperature programmed desorption (TPD) study that multi-activation-energies were involved in the desorption of (C-O) complexes due to the complexity of the carbon surface structure. This multi-activation-energy process could be described by introducing an energy distribution function, f(E), where $f(E)\Delta E$ is the fraction of total (C-O) population with activation energy between E and $E+\Delta E$. The energy distribution function is determinable from the TPD experimental data, and was found to be close to normal and bimodal Gaussian distributions for the ST1 and ST2 samples respectively, i.e.,

for ST1 $$f(E) = \frac{1}{\sqrt{2\pi}\,\sigma} \exp\left[-\frac{(E - \bar{E})^2}{2\sigma^2}\right]$$

with $\bar{E} = 69.7$ kcal/mol, $\sigma = 7.81$ kcal/mol;

for ST2 $$f(E) = \frac{1}{\sqrt{2\pi}}\left\{\frac{0.74}{\sigma_1}\exp\left[-\frac{(E - \bar{E}_1)^2}{2\sigma_1^2}\right] + \frac{0.26}{\sigma_2}\exp\left[-\frac{(E - \bar{E}_2)^2}{2\sigma_2^2}\right]\right\}$$

with $\bar{E}_1 = 67.9$ kcal/mol, $\sigma_1 = 7.82$ kcal/mol

and $\bar{E}_2 = 79.7$ kcal/mol, $\sigma_2 = 3.70$ kcal/mol.

It was also found that both CO and CO_2 are primary products during carbon oxidation, but they are generated via different mechanisms.

Separate examination of CO and CO_2 formation revealed some new insights about the carbon oxidation. The CO formation was found to follow the conventional adsorption-desorption path which usually has a feature of fractional order with respect to the partial pressure of O_2; while the CO_2 formation was found to be a first order reaction with respect to the partial pressure of O_2. The fractional order for CO formation and the first order for CO_2 formation, therefore, resulted in the observed fractional order of ~ 0.83 for the overall oxidation.

Reactivity of the carbon oxidation can be effectively catalyzed by calcium. An increase of about 50 fold in reactivity around 763K was experimentally observed on a 2 wt% Ca added soot sample, ST2. A further study of the individual CO and CO_2 rates in the ST2 oxidation revealed that the addition of Ca had little effect on the rate of CO formation, and the increase in the overall reactivity was primarily attributed to the increase in the rate of CO_2 formation.

Incorporating the preceding discussions, a carbon oxidation model is proposed to explain the experimental results for the ST1 and ST2 samples, and leads to the following conclusions:

1) The controlling factor for a non-catalytic carbon oxidation is the carbon structure which may be appropriately represented by the site energy distribution of that carbon.

2) The controlling factor for a Ca catalyzed carbon oxidation is the Ca loading on the carbon surface. The CO/CO_2 ratio provides a measure of the importance of the catalytic effect in the oxidation.

Thesis advisors:

Prof. Adel F. Sarofim, Professor of Chemical Engineering.
Prof. John P. Longwell, Professor of Chemical Engineering.

Acknowledgements

I gratefully acknowledge the guidance from Professor Adel F. Sarofim and Professor John P. Longwell. Without their encouragement and invaluable guidance, this thesis would never have been completed. I would also like to express my gratitude to the members of my thesis committee, Professor James Keck, Professor Jack Howard, and Doctor Charles Mims, for their suggestions and helpful criticisms during the course of this study.

The friendships and the technical discussions with other members of my research group as well as my fellow students will long be remembered. Although this list is far from complete, I wish to especially acknowledge the discussions I have had with Bob Hurt, Tony Modestino, Guangxi Yue, Jirong Xiao, Tong Chen, Joe Floess, Alan Feitelberg, Shin-Gyoo Kang, Jean DeHemptinne, Karl Graham, Judy Wornat, Dave Dudek, Vic Gobbell, and Tom Griffin.

Special thanks to Long-qing Chen, Fannie Mui, and Shiao-ming Chu for the time and care they put into typing a portion of this manuscript.

Financial support from Exxon Corporation and Dr. G. Y. Chu during my stay at MIT is gratefully acknowledged.

Finally, I would like to thank my parents and my brother for their love, support and encouragement of my studies. In particular, I wish to thank my wife, Ling Ma, for her constant support, understanding, encouragement, and love throughout my years at MIT. This thesis is as much the result of her efforts as mine. To her, I dedicate this thesis.

TO:

Ling Ma

Table of Contents

List of Figures

List of Tables

Chapter 1. Introduction & Background

1.1 Introduction

Carbon, as the term will often be used in this thesis, refers not to an entry in the periodic table, but to a class of solid materials containing primarily carbon, with varying amounts of impurities including hydrogen, oxygen nitrogen, sulfur, and inorganic material. Carbons can be found in nature, such as natural graphite, or can be made by heating an organic substance in the absence of oxygen. Much of the organic material which is rich in hydrogen and oxygen is lost to the gas phase upon heating, leaving a porous solid residue, carbon or char, containing some hydrogen and oxygen in amounts that decrease with increasing the charring temperature.

Carbons participate in high temperature reactions with a variety of gaseous species, in which the solid carbon is consumed and new gaseous species are produced. These are the so-called gas reactions of carbon, and the set of gaseous reactants includes oxygen, carbon dioxide, hydrogen, and water vapor. The oxygen-carbon reaction is the subject studied in this thesis.

The carbon oxidations are important to many practical applications, including coal gasification and combustion in entrained flow gasifier, pulverized-coal-fired cyclone burner and coal-water-slurry boiler. The gasification reactivity of carbon is especially important in many gasification processes, determining equipment size and/or carbon conversion efficiency [1].

Many different gasification processes have been proposed. For the optimal design and selection of processes, an understanding of gasification kinetics is important. Under most conditions, the total time required for

the gasification of a coal particle is dominated by the burn-out of the residual char remaining after devolatilization. The design of many gasifiers is carbon reactivity limited and, in fact, many gasifiers operate with significantly less than 100% carbon conversion despite strong economic incentives to use coal efficiently. (The cost of coal has been estimated to be about 40% of the total cost of conversion to pipeline quality gas [2].) Carbon conversion for several industrial gasification systems are given in Table 1.1.

Table 1.1

Carbon Conversion in Industrial Gasification Processes [1]

Gasifier Type	Koppers-Totzek Entrained Flow	B+W du Pont Entrained Flow	Winkler Fluidized Bed
Fuel Carbon Conversion[a]	88.6%	84.1	80%

(a) Fuel carbon conversion is defined as carbon in gases/carbon in input fuel.

Note that the carbon losses in fluidized bed system are largely due to entrainment of dust and increase with the friability of the fuel [1].

Because of its importance there has accumulated a large body of research on the coal char gasification kinetics, much of which is very empirical. Many recent studies are attempting to obtain more fundamental kinetic information which will hopefully be widely applicable. The common goal of the empirical and fundamental approaches is to predict the effect of reactant gas composition, pressure, temperature, coal type, char preparation and prior reaction history on the reactivity and the

product distribution. A review of the current literature on carbon oxidation, with an emphasis on phenomena that determine the carbon oxidation rate, is the subject of the next section.

1.2 Literature Review

The literature on carbon is truly enormous, with the literature on the carbon oxidations being a substantial contributor. Fortunately, many good review articles are available on the topic of the carbon-gas reactions , each with a somewhat different emphasis [3], [4], [5], as are more comprehensive reviews on important subtopics such as catalyzed reaction [6] and carbon graphitization [7]. These are the sources to which to turn for general information or as a starting point. The following discussions will be focused on those aspects of carbon structure and carbon oxidation which are especially relevant to the thesis work.

1.21 Carbon Structure

Crystalline graphite is composed of sheets of aromatically bonded carbon, stacked together with a uniform interlaryer spacing, and aligned in such a way as to produce a regular three-dimensional crystal structure. Graphite is almost pure carbon, impurities residing only in defects, at crystallite boundaries, or as physically incorporated inclusions.

Non-graphitized carbons are also composed of stacked sheets of aromatically bonded carbon, which, however, are small, often imperfect, often misaligned, and without three dimensional order. The lack of a three dimensional crystal structure, even among regular stacks of perfect graphitic layers, is the characteristic of the "turbostratic" structure of lower temperature carbons. Hydrogen, oxygen, and other heteroatoms are

relatively common in low temperature carbons, existing at the edges of graphitic layers, as cross linkages between layers, or as defects within layers. For a variety of coal chars prepared at 973K the atomic ratio of carbon to hydrogen was about 5 to 1, and the atomic ratio of carbon to heteroatoms about 20 to 1 [8]. The hydrogen content in graphite is much lower [8].

X-ray diffraction is perhaps the most powerful tool for the investigation of carbon structure, yielding information on average layer diameter, layer diameter distribution, interlayer spacing, average stacking depth, and fraction non-crystalline or X-ray amorphous material [9-13]. A model of carbon structure, arising primarily from these X-ray studies, is depicted in Fig.1.1 [14]. The lines in the diagram are small, graphitic layers, viewed from the side, whose imperfect packing arrangement is responsible for carbon micropores. The circles in the diagram are not part of the structure, but rather indicate regions which would be identified as crystalline by X-ray diffraction. (Note that the crystallite size determined by X-ray diffraction is smaller than the true dimension of the continuous but kinked graphitic layers.) Not shown in the diagram are cross linkages between layers and some amorphous material, possible heteroatoms or tetrahedral carbon.

Whereas the imperfect packing arrangement of graphitic layers is responsible for carbon microporosity, larger pores are physical rather than chemical cracks in the solid matrix. Carbon contains pores with diameters from several microns or larger to several angstroms, with many carbons having significant pore volume throughout the entire range of pore diameter [15].

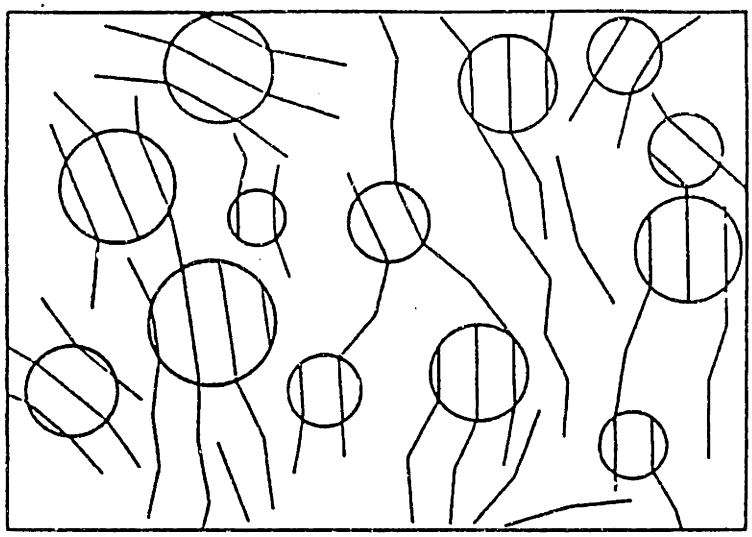

Fig. 1.1 Amorphous carbon structure [14].

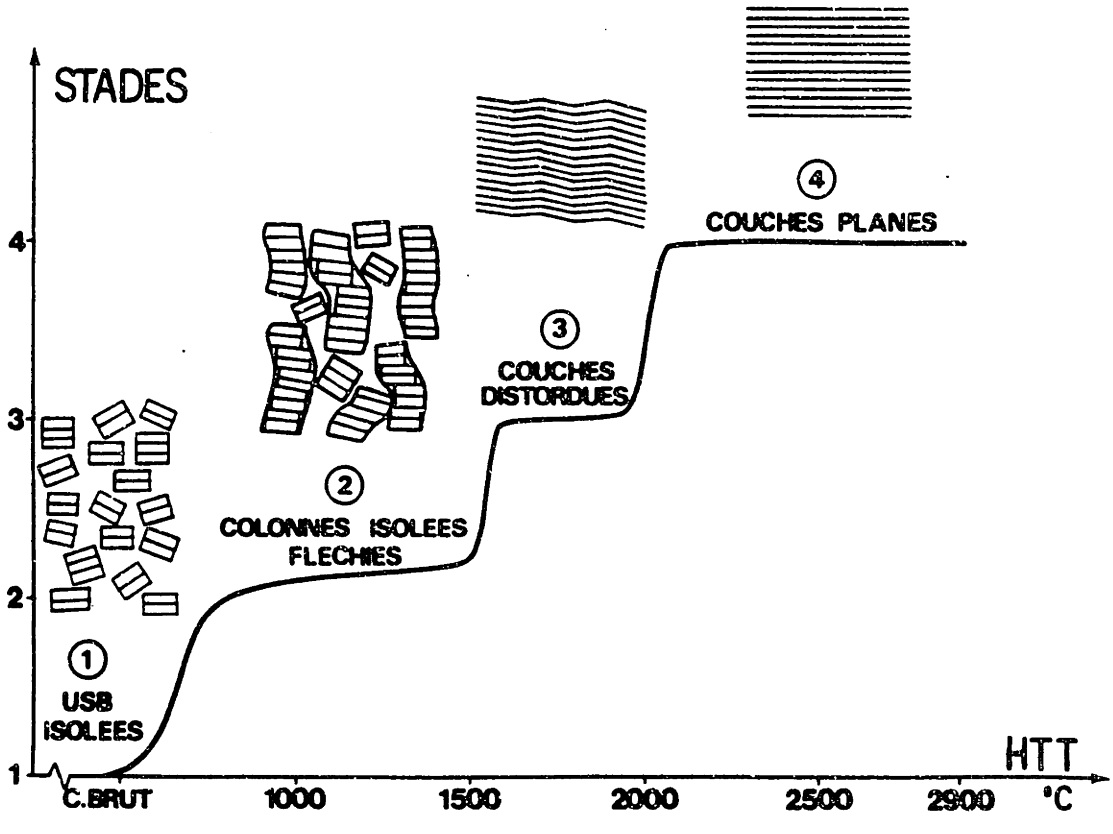

Fig. 1.2 Various steps of graphitization and sketch of the process [16].

The imperfect, disordered structures in amorphous carbon will gradually disappear upon heat treatment or graphitization. Fig. 1.2 [16] shows how the imperfect packing is rearranged at different graphitization stages. All the carbonaceous materials follow the same graphitization process, regardless of the degree of crumpling of their layers. Before the semi-coke stage, bulk mesophases made of individual BSU's (basic structural unit) are formed. Then, distorted and wrinkled layers appear below 2273K. These layers stiffen rapidly and dewrinkle above 2373K. When HTT (heat treatment temperature) increases further, flat lamellae result in flat polycrystalline graphite [7].

1.22 Studies of the oxidation of graphite and pure carbons

The current fundamental understanding of factors that determine carbon oxidation reactivity comes primarily from the literature on graphite and pure carbons. Important factors include the following:

1.221 Crystallite orientation.

Several researchers [17], [18] have found large differences between the reactivities of the different crystalline faces of graphitized carbons. Walker et al. [17] have established a qualitative correlation between the reactivity of graphitized carbon plates and the proportion of the exposed surface composed of crystallite edges. Smith and Polley [18] have found a higher reactivity by a factor of about 200 for a carbon black surface containing many exposed edge sites compared to a graphitized sample composed entirely of crystallites with their basal planes oriented parallel to the surface. Attack can occur on basal planes if active sites are provided by surface imperfections such as dislocations. Reaction on such sites

creates active surface area in the form of edge sites, and in the presence of a catalyst particle these sites of attack can grow into hexagonal pits which have been observed optically [19].

1.222 Crystallite size

It is generally difficult to distinguish between crystallite size and orientation effects because the two variables are often coupled in practice. Armington [20]. however, has been able to change crystallite size independently by looking at the special system of graphitized carbon black, which forms non-porous polyhedral particles whose surfaces are composed almost entirely of carbon basal planes. He measured the reactivity of different sized particles (which are composed of different sized crystallites) and found that specific reactivity (gram/min-m^2) increasing crystallite size. He theorizes that the larger the crystallite, the greater number of impurity atoms capable of affecting any given edge carbon via π-electron transfer through the basal plane. This effect is probably less important than that of crystallite orientation.

1.223 Structural Sensitivity

In light of the preceding discussion, it is expected that reactivity of the carbon oxidation will largely depend on the structure of the carbon. Smith [5] studied the carbon-oxygen reaction using various carbon materials, and reported that there exists a significant variation in reactivity among different carbons even though the effects due to different pore sizes and surface areas have been eliminated (see Fig. 1.3a). In particular, those disordered amorphous carbons were found to correspond to the higher oxidation reactivity and lower apparent activation energy,

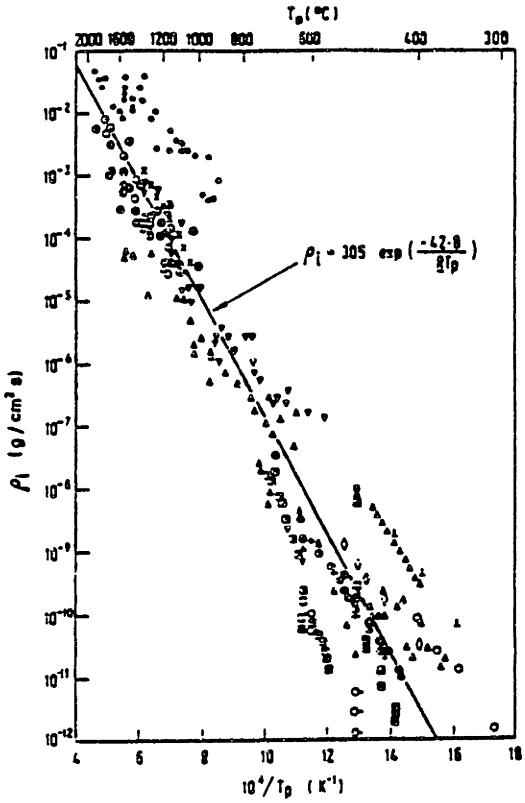

Fig. 1.3a Intrinsic reactivity of various carbon when P_{O_2} = 1 atm [5].

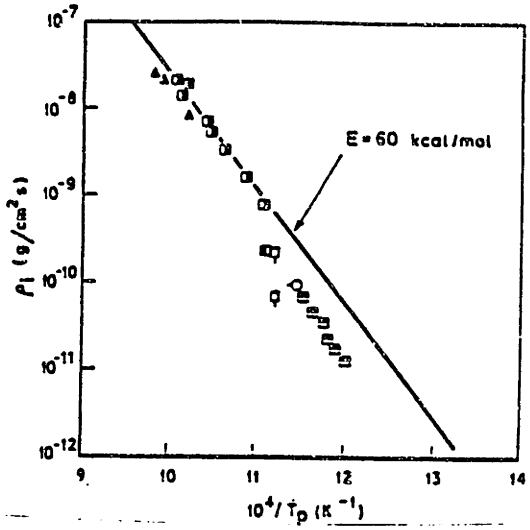

Fig. 1.3b Oxidation rate of highly purified carbons when P_{O_2} = 1 atm [5].

key for Fig. 1.3:

- Petroleum coke
- Brown-coal char
- Lignite char
- Anthracite
- Semi-anthracite
- Bituminous-coal char
- Metallurgical coke
- Soot
- Pitch coke
- Pitch resin
- Nuclear graphite
- Cracker carbon (uncatalysed)
- Cracker carbon (catalysed)
- AGKSP graphite
- AGKSP graphite
- AUF
- SPI
- SPI
- Spectroscopic graphite
- Graphon
- Purified carbons
- Sterling FT
- Acheson NC
- Acheson AFC 4

compared with the highly-ordered graphitic carbons (see also Fig. 1.3a & 1.3b).

1.224 CO/CO_2 Ratio

The CO/CO_2 ratio in the product of carbon oxidation has been considered by many researchers [1], [21-28]. The consensus is that both CO and CO_2 are primary products, with the CO/CO_2 ratio increasing substantially at higher temperatures and lower pressures [4]. A possible explanation is that CO is formed at carbon edges while CO_2 is formed at inorganic sites [27], [29]. Lower temperatures favor CO_2 due to catalytic activity; higher temperatures promote utilization of carbon edges. The CO/CO_2 ratio can be correlated by [23-28]:

$$\frac{CO}{CO_2} = Ae^{-E/RT}$$

The results from the previous studies are tabulated in Table 1.2.

1.225 Reaction Order

Previous investigations of carbon oxidation indicate that the intrinsic reaction order varies between zero and one, depending on oxidation conditions and carbon samples. Suuberg et al [30] reviewed the intrinsic reaction order for low temperature oxidation of carbons, and their results are summarized in Table 1.3.

1.226 Mechanism for the Uncatalyzed Carbon Oxidation

Although the kinetics of carbon-oxygen reaction has been extensively studied over several decades, understanding of the reaction mechanism, in terms of elementary processes of adsorption, migration,

Table 1.2

CO/CO_2 Ratio during Oxidation of Carbons

Author	Material	P_{O_2} (atm)	T (K)	A	E (kcal/mol)
Arthur [23]	Natur. Graph. & coal char	0.05-0.25	733 1173	$10^{3.4}$	12.4
Rossberg [24]	electrode carbons	—	793 1693	$10^{3.3}$ $10^{3.9}$	14.3 18.3
Bonnetain et al [25]	graphites	0.01-0.1	673 973	—	6.0 8.5
Otterbein et al [26]	vitreus carbon	0.025-0.15	773 923	—	6.0
Phillips et al [27]	Graphon	0.013-0.26	798 948	140 200	6.4
Tognotti et al [28]	Spherocarb	0.05 0.20 1.00	673-1673	93 68 50	5.93 6.10 6.10

Table 1.3
Intrinsic Reaction Order for Carbon Oxidation [30]

Material	Surface Area (m^2/g)	Impurities (ppm)	Pyrolysis Temp.(K)	Oxidation Temp.(K)	Pressure O_2(kPa)	log(t) (s)	Measurement	E (kJ/mol)	n
GRAPHITE	-	-	-	880-925	0.4-6	9.2	TGA	226	0.77
GRAPHITE	0.4-1	<6	-	963-993	2-33	10.4	GAS	268	0.19 -0.34
GRAPHITE	0.8	<10	-	843	$5x10^{-3}$-0.03	9.5	GAS	209	0.5
GRAPHITE	4.3	<1(B)	-	898	0.3-26	9.2	TGA	221	0.6
GRAPHITE	3	[B/C=10^{-2}]	-	898	0.3-26	9.0	TGA	192	0.59
GRAPHITE-M	-	-	-	1023	0.8-8	9.4	TGA	197	0.6
GRAPHITE-P	-	-	-	998	0.8-8	10.4	TGA	222	0.5
GRAPHITE	<0.9	<6	-	693-803	21-101	7.4	GAS	149	0.6
GRAPHITE	0.4	200	-	723-773	0.2-13	7.2	TGA	153	1
GRAPHITE	-	1	-	973	0.3-101	9.5	TGA	163	1
GRAPHITE	2.4	<6	-	837-933	6-100	10.4	GAS	286	0.51
GRAPHITE	-	-	-	848-928	2.5-20	8.7	GAS	186	0.54 -0.6
GRAPHITE	-	150	-	848-898	4-17	8.2	GAS	167	0.65
GRAPHITE-ARMCHAIR[a]	-	-	-	1085	1.3-13	9.5[c]	PIT	259	0.21
ZIG-ZAG[b]	-	-	-	1085	1.3-12	9.4[c]	PIT	276	0.3
GRAPHON	81	150	-	773	0.3-3	7.6	TGA	180	0.5
GRAPHITE	-	<10	-	973	0.1-101	-	GAS	-	0.52-0.73
GRAPHITE	-	~0	-	844	5.3-101	-	GAS	-	0.57
GRAPHITE	-	16(Pb)	-	642	5.3-101	-	GAS	-	0.24-0.53
SUCROSE CHAR	-	10	2773	1005	0.1-101	-	GAS	-	0.66
GLASSY CARBON	0.5	<50	-	805-873	$9x10^{-3}$-0.02	8.8	GAS	209	0.5
PVA[c] CHAR	<5	~0	3200	921	1.7-7.1	10.8	TGA	248	0.66

Material	Surface Area (m^2/g)	Impurities (ppm)	Pyrolysis Temp.(K)	Oxidation Temp.(K)	Pressure O_2(kPa)	log(t) (s)	Measurement	E (kJ/mol)	n
PVA CHAR	<5	~0	1200	730-795	1.4-6.2	6.7	TGA	127	0.40
ACN[f] CHAR	-	-	1200	825-850	0.4-6.0	7.8	TGA	174	0.7
PFA[g] CHAR	300	-	1200	793	0.4-6.0	5.2	TGA	149	0.98
PFA CHAR	<5	-	2100	860-930	0.4-6.0	8.4	TGA	198	0.67
PVA CHAR	<5	55(Co)	1200	750-760	1.4-4.7	6.0	TGA	157	0.62
PVA CHAR	<5	3150(Co)	1200	630-645	0.6-6.7	5.5	TGA	148	0.37
PVA CHAR	<5	105(Fe)	1200	700-800	0.7-7.3	5.7	TGA	126	0.8
PVA CHAR	<5	3400(Fe)	1200	700-800	0.7-7.3	6.3	TGA	204	0.8
CALGON RC	1210	<1%	-	748	2-100	5.9	TGA	135	0.7
PET COKE	0.9-1.6	0.4-0.8%	-	750	24-51	5.5	GAS	159	0.59
PYRO. FILM	-	-	1000	823-973	2.7-15.9	4.8	GAS[d]	159	1
ANTHR. CHAR	1.7	11.2%[h]	1273	773-873	2-100	6.0	TGA	137	0.9
BIT. COAL CHAR	15	7.8%[h]	1273	748-823	2-100	4.4	TGA	121	0.75
LIGNITE CHAR	109	9.3%[h]	1073	673-748	1-20	3.1	TGA	115	0.7
LIGNITE CHAR	-	7.7%[h]	1273	678	2-21	3.4	TGA	-	0.63
BROWN COAL CHAR	432-816	2.2%	1600	<730	5-9	2.6	GAS	134	0.25 -0.5
PF[i] CHAR	326	~200	1273	573-623	0.5-101	4.6	TGA	131	0.68

a. 11$\bar{2}$0 face
b. 10$\bar{1}$0 face
c. If rate constants applied to 1 mm nonporous particles
d. Also film thickness
e. Polyvinyl acetate
f. Acenaphthylene
g. Polyfurfuryl alcohol
h. Ash in raw coal
i. Phenol-formaldehyde

TGA refers to thermogravimetric analysis
GAS refers to measurements of CO + CO_2
PIT refers to measurements of pit sizes

B refers to boron content of char

dissociation, and desorption, is still preliminary. Blyholder and Eyring [31] recommended the following mechanism in 1959:

$$2C_f + O_2 \rightleftharpoons 2(C\text{-}O)' \qquad (R1.1)$$

$$(C\text{-}O)' \longrightarrow (C\text{-}O) \qquad (R1.2)$$

$$(C\text{-}O) \longrightarrow CO + C_f \qquad (R1.3)$$

where C_f denotes the free carbon site available for O_2 chemisorption. This set of mechanisms is consistent with quantum mechanical calculations which favor mobile (two-site) chemisorption [32]. Reaction (R1.2) has also been postulated by Marsh et al [33] and Walker et al [34,35]. Blyholder and Eyring [31] suggested that (C-O)' represents a mobile ionic bond while (C-O) represents an immobile covalent (carbonyl) bond. Unfortunately, the Blyholder and Eyring's mechanism can not account for the rapidity of the carbon-oxygen reaction at lower temperatures. Moreover, the reverse of reaction (R1.1) can not occur since experimental work has shown O_2 adsorption to be irreversible for temperatures greater than 203K [36-38].

A possible alternative was proposed by Laurendeau [4],

$$2C_f + O_2 \longrightarrow 2(C\text{-}O)' \qquad (R1.1)$$

$$(C\text{-}O)' \longrightarrow (C\text{-}O) \qquad (R1.2)$$

$$(C\text{-}O) \longrightarrow CO + C_f \qquad (R1.3)$$

$$(C\text{-}O)' \longrightarrow CO + C_f \qquad (R1.4)$$

$$(C\text{-}O)' + (C\text{-}O)' \longrightarrow CO_2 + C_f \qquad (R1.5)$$

Reaction (R1.4) is an attempt to provide faster conversion to CO at lower temperatures than allowed by reaction (R1.3). Reaction (R1.5) has been found by Walker et al [34] to be responsible for the primary CO_2 formation. In addition, reaction (R1.5) is also consistent with Blackwood and McTaggart's observation that CO_2 is produced during reaction between carbon and atomic oxygen [39].

A set of more sophisticated two-site mechanisms can be found in [40] as

$$C_{f,a} + O_2 \longrightarrow 2(C\text{-}O_2)_a \qquad (R1.6a)$$

$$C_{f,b} + O_2 \longrightarrow 2(C\text{-}O_2)_b \qquad (R1.6b)$$

$$C_{f,a} + (C\text{-}O_2)_a \longrightarrow 2(C\text{-}O)_a \qquad (R1.7)$$

$$C_{f,b} + (C\text{-}O_2)_a \longrightarrow (C\text{-}O)_a + (C\text{-}O)_b \qquad (R1.8)$$

$$(C\text{-}O)_b \longrightarrow CO + C_{f,b} \qquad (R1.9)$$

$$C_{f,b} + (C\text{-}O)_b + O_2 \longrightarrow CO_2 + (C\text{-}O)_b + 2C_{f,b} \qquad (R1.10a)$$

$$C_{f,b} + (C\text{-}O)_a + O_2 \longrightarrow CO_2 + (C\text{-}O)_b + C_{f,b} \qquad (R1.10b)$$

$$C_{f,b} + (C\text{-}O)_a + O_2 \longrightarrow CO_2 + (C\text{-}O)_b + C_{f,a} \qquad (R1.10c)$$

where subscripts a and b denote fast and slow oxygen adsorption sites, respectively. Note that CO_2 is generated in the carbon oxidation through reactions (R1.10a), (R1.10b) and (R1.10c). These reactions may occur through loose adsorption of O_2 on a free carbon site adjacent to a (C-O) complex, and then recombination of the weakly adsorbed O_2 with the (C-O) complex to form CO_2 [41]. Since the "type a" sties are very active in terms of O_2 adsorption and are rapidly saturated at the beginning of the oxidation, only $C_{f,b}$ will be significantly involved in the subsequent reactions (R1.10a,b,c) producing CO_2 [40]. It is also noted that the rate of CO_2 formation by (R1.10a,b,c) is directly related to the O_2 partial pressure, which is consistent with the observations presented in Chapter 5 of this thesis. Khan [42] recommended the similar direct oxidation mechanism.

1.23 Studies of Catalyzed Carbon Oxidation

1.231 An Overview

The substantial literature, in which the catalytic effect of many different elements on char and graphite reaction rates has been

investigated, has been reviewed by Walker et al. [43]; Wen [43]; McKee [6]; and Wood and Sancier [45].

A wide range of inorganic materials have been found to be active gasification catalysts, with the magnitude of the catalytic effect being a function of the metal, its dispersion, its chemical state, and the gaseous environment [6]. Active catalysts for the reaction between carbon and molecular oxygen include alkali metal oxides and salts and the alkaline earth oxides and salts [6], with Amariglio and Duval [46] reporting catalytic efficacy in the order Na > Ba > Sr > Mg > Ca. Many transition metals and oxides are also active, with Ni > Co > Cu > Ag > Fe > Ca (inactive), at an impurity level of 400 ppm as reported by Marsh and Adair [47]. Note that this group of transition metals is much more active than the alkaline earths, Ca being regarded as inactive at the 400 ppm level. Other active catalysts include compounds involving Ag, Pt, Ir, Rh, Pd, Au, Cu, Pd, As, Sb, and Bi [6]. The effect of various metal catalysts on the ignition temperature of graphite-oxygen reaction is listed in Table 1.4 [48].

The effect of certain additives has been observed to inhibit the oxygen reaction including phosphorus pentoxide and certain compounds containing halogens. A more detailed discussion and information on catalyzed gasification in other environments can be found in McKee [6]

Catalyst dispersion is critical to catalyst efficacy, as illustrated by the work of Floess [49]. Addition of 3.6 wt% initially atomically dispersed Ca to a sucrose carbon, increased the carbon's gasification reactivity in air by almost two orders of magnitude, while addition of 1μ sized $CaCO_3$ inclusions by physical mixing increased reactivity by only a factor of two. In addition, Radovic [50], has related the gasification reactivity of a lignite

Table 1.4

Effect of Catalysts on the Ignition Temperature of Graphite-O_2 Reaction [48]

Catalyst (acetate or oxide)	w/o as metal	Ignition temp (°C)	Direction of attack
Pb	0·15	382	*a, c*
V	0·20	490	*a*
Mn	0·45	523	*c*
Co	0·33	525	*a*
Cr	0·95	540	
Cu	0·20	570	*a*
Mo	0·15	572	*a, c*
Ag	0·16	585	*c*
Cd	0·21	590	*a*
Fe	0·13	593	*c*
Pt	0·03	602	*a, c*
Ni	0·45	613	*a*
Ir	0·40	638	*a, c*
Rh	0·20	622	*a, c*
Ru	0·30	640	*a, c*
Pd	0·30	659	*a, c*
Ce	0·72	692	
Zn	50·00	700	
W	0·02	718	
Hg	0·10	720	
Sn	0·10	738	
Uncatalyzed		740	*c*

char to the degree of CaO dispersion measured by X-ray diffraction line broadening.

The presence of catalysts generally results in a decrease in the CO/CO_2 ratio in the product at a given temperature, whereas inhibitors of carbon oxidation have the opposite effect [6]. For example, Harker et al. [51] showed that potassium impurity, introduced either electrochemically or from the vapor phase, had a marked effect in accelerating the gasification of neutron-irradiated graphite by oxygen. The higher combustion rate appeared to be due almost entirely to a higher rate of formation of CO_2, the rate of formation of CO remaining essentially unchanged on addition of the alkali metal. Interpretation of these changes in product ratio is complicated by the fact that many carbon-oxidation catalysts, for example CuO, NiO, Ag, and Pt are also excellent catalysts for CO oxidation to CO_2, where compounds such as $POCl_3$ inhibit both the oxidation of solid carbon and that of gaseous CO [6]. Hence change in the CO/CO_2 ratio upon addition of catalysts may be a result of secondary processes rather than a consequence of elementary steps occurring at the carbon surface.

1.232 Mechanism for Catalyzed Carbon Oxidation

Attempts to explain the catalytic activity in terms of a chemical mechanism .have been directed toward establishing a broad ranging explanation that encompasses the numerous species that act as catalysts. The two most widely supported explanations to date are the electron transfer and the oxygen transfer mechanisms.

The electron transfer mechanism, the details of which were originally proposed by Long and Sykes [52], postulates that the catalyst affects the

general energy level of solid. It proposes that the catalyst acts by withdrawing a π-electron from the graphitic structure. Calculations with molecular orbital theory show that such an electron deficient ring would induce a stronger carbon-oxygen bond and weaken the adjacent carbon-carbon bonds. Long and Sykes suggest that transition elements, which have unfilled d-bands, could withdraw a π-electron from the ring structure and that the alkali and alkaline earth elements could form covalent bonds at points of high electron density and thereby withdraw a π-electron. This mechanism does not require the catalyst to be situated directly at a reactive site; the catalyst only alters the electron distribution of the carbon substrate. Floess [49], after an intensive study of calcium catalyzed carbon oxidation, found that the apparent activation energy of the catalyzed char is systematically lower than that of the uncatalyzed char. He argued that a calcium catalyst acts through an alteration of the electron distribution in the carbon, thereby changing the overall activation energy level of the carbon [49].

The oxygen transfer mechanism proposes that the catalyst undergoes oxidation reduction cycles with the reactant and the carbon and thereby acts as an intermediate to supply oxygen to the carbon. McKee [6] lists as support for this mechanism the observation of Amariglio and Duval [46] who suggest that only metals that can oscillate between two or more oxidation states can act as oxidation catalysts. McKee also notes that transition elements that can be reduced by carbon at temperatures below 1273K are active catalysts, whereas stable oxides such as those of aluminum, silica, and tungsten are not. Further evidence for this mechanism are the CAEM (controlled atmosphere electron microscopy) experiments, which usually show mobile catalyst particles on the carbon

surface and extensive pitting of the carbon near the particle. This phenomena is interpreted as evidence of cyclic oxidation and reduction of the catalyst particle as it migrates across the carbon surface [53]. For the alkali and alkaline earth elements, evidence for this mechanism are the observations that carbon accelerates the decomposition of the carbonate to the oxide and that the oxide form is the active species during the catalyzed carbon-oxygen reaction. McKee [6] [53] suggests that a possible reaction sequence involving these elements could be:

$$M_2CO_3 + C + O_2 \longrightarrow M_2O + 2CO_2 \qquad \text{(R1.11)}$$

$$M_2O + 1/2\ O_2 \longrightarrow M_2O_2 \qquad \text{(R1.12)}$$

$$2M_2O_2 + C \longrightarrow 2M_2O + CO_2 \qquad \text{(R1.13)}$$

where the active intermediary compound is a peroxide or higher oxide. M is assumed to be any group IA element.

Based on experimental data which show the alkaline earth (group IIA) elements to behave analogously to the group IA elements as carbon catalysts, McKee [54, 55] suggests that an analogous mechanism applies to these elements. Radovic et al. [56] extent above oxidation-reduction mechanism to the Ca catalyzed carbon oxidation.

Wood and Sancier [45] point out that much of the recent experimental data support a mechanism whereby the catalyst acts to supply oxygen to the carbon but indicate that there is insufficient data to establish a possible reaction sequence. Evidence for a mechanism involving oxygen transfer is based to a larger extent on Wood's study of the carbon-alkali reaction and on the work of Mims and Pabst [57,58]. Mims and Pabst have clearly demonstrated that K_2CO_3 will react with the carbonaceous substrate to form a stable and distinct surface salt complex, which is assumed to be analogous to a phenolate salt [59]:

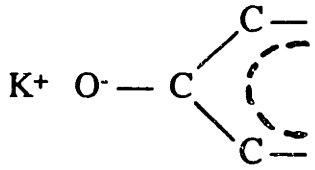

Their data provide strong evidence that the surface complexes participate directly in the catalytic reaction. They postulate that these surface salts accelerate the reaction by acting as oxygen transfer sites. Mims and Pabst argue that catalysis occurs because the catalyst increases the number of active sites on the carbon. Their studies, however, were concerned only with the steam and carbon dioxide reactions.

Objections to the oxygen transfer mechanism have been pointed out by a number of researchers. Walker et al. [43] note that the mechanism tacitly assumes that the rate-controlling step for the non-catalyzed reaction is oxygen chemisorption or that the catalyst particle acts as an active site center. Long and Sykes [52] conclude that since this mechanism consists of a series of steps completely different from those occurring in the non-catalyzed reaction, it would be expected that the kinetic parameters of the catalyzed reaction be widely different. This is usually not observed.

1.3 Problem Statement and Thesis Objective

The entire oxidation of carbon consists of two processes: (1) Chemical reaction, which involves that oxygen reacts with carbon on the carbon surface and generates CO and CO_2 gaseous products. The intrinsic chemical kinetics of the oxygen - carbon system determines the rate of this chemical reaction. (2) Heat and mass transfer, which generally involves transfers of the heat and gaseous products (CO and CO_2) generated in the chemical

reaction from carbon surface to bulk, as well as the reactant (oxygen) from bulk to carbon surface. The rates of these transfer processes depend on temperature and gas concentration fields as well as reactivity and heat release of the chemical reaction.

The focus of this thesis work will be on the chemical kinetics of carbon oxidation for the following two reasons: (1) The chemical kinetics of carbon oxidation is much more poorly understood so far, compared to the heat and mass transfer process. (2) The knowledge of chemical kinetics is crucial in understanding of the transfer processes in carbon oxidation because the chemical kinetics determines the rate of heat and mass generation during the reaction.

Despite of a large body of research on carbon oxidation kinetics, an approximate understanding of the reaction mechanism has not yet been obtained, and a quantitative understanding of primary variables that determine the reactivity of a specific carbon and how this reactivity changes with conversion are still unknown. The presence of inorganic species in carbon adds another complication to the understanding of carbon oxidation. Although a large increase in reactivity is often obtained by the addition of a small amount of certain compound to carbon, the detailed catalytic mechanism is not understood.

The objective of this thesis is to develop a comprehensive model to better understand the chemical kinetics during carbon oxidation, especially, this thesis will address the following aspects:

1) Reaction mechanism: Based on the available experimental results, a set of reaction mechanisms for carbon oxidation is proposed in Chapter 5. This set of mechanisms forms the base of the kinetic model.

2) Reactivity of the carbon oxidation: The intrinsic reactivity of the carbon oxidation is studied under different oxidation conditions. Temperature dependence (apparent activation energy) as well as oxygen partial pressure dependence (apparent reaction order) of the oxidation rate are especially examined.

3) CO/CO_2 ratio: Product ratio, CO/CO_2, at different reaction temperatures and O_2 partial pressures is studied in this thesis. Since the heat release involved in the formations of CO and CO_2 is pronouncedly different (27 kcal/mol for the CO formation and 94 kcal/mol for the CO_2 formation), the CO/CO_2 ratio governs the total heat release during carbon oxidation and is especially important for high temperature oxidation where heat and mass transfer becomes significant.

4) Effect of Ca catalyst on carbon oxidation: The role of a calcium catalyst in carbon oxidation is investigated in this study, because of the abundance of calcium in many coals and oil shales either as calcium carbonate or ion exchanged onto the organic matrix.

Chapter 2. Materials, Experimental Equipments & Procedures

2.1 Materials

Two model carbon materials, uncatalyzed soot as well as catalyzed soot, were used in this study to allow control over the physical properties and the chemical compositions of the carbon samples. The uncatalyzed soot was made from a premixed ethylene flame, and it has almost no mineral content (see Table 2.1). The lack of inorganic element in the uncatalyzed soot eliminates the possibility of catalytic effects on the carbon reaction, and makes the uncatalyzed soot a good non-catalytic carbon material. The catalyzed soot was made from ion exchange of calcium with the uncatalyzed soot. Since the catalyzed soot sample consists of only calcium as an inorganic component, it provides a well characterized catalytic system.

2.11 Uncatalyzed Soot

The uncatalyzed soot sample, referred as ST1 hereinafter, was generated in a premixed ethylene flame (C/O = 0.98), and collected on a water cooled copper plate placed at 38 mm above the flame holder. The flame was stabilized over an uncooled ceramic honeycomb burner plug, 47.6 mm in diameter, of corning CELCOR, 62 cell/cm^2 and 3.8 cm thick [60]. Care was taken during the collection process to reduce impurity level of the soot. A series of filters were installed along the gas line to make flame as 'clean' as possible, and pure nitrogen continuously flew around the flame to prevent any contaminations from the room air. After being collected from the premixed ethylene flame, all soot particles were

extracted in methyene-chloride solution for about 24 hours in order to eliminate most hydrocarbons, and then heat-treated in argon at 1173 K for about 15 minutes followed by at 573 K for about 20 hours. The soot after the heat treatment is called fresh ST1.

Elemental analysis for the fresh ST1, performed by Galbraith Laboratory, results in C/H/O = 1.0/0.13/0.02 and ash content < 32 ppm (see Table 2.1). A TEM picture of the fresh ST1 is presented in Fig. 2.1. It can be seen that the ST1 is aggregated by up to several hundreds of pseudo spherical primary particles which are quite uniform apparently with an average diameter around 43 nm.

Surface areas of ST1 was determined from carbon dioxide adsorption isotherms at room temperature (297 K) using Dubinin-Polanyi equation (see Chapter 3 for detail). Their values are given in Fig. 2.2 as a function of conversion*.

Table 2.1 Elemental Analyses for The Fresh ST1

job #	C(%)	H(%)	O(%)	ash(ppm)	H/C	O/C
1	94.31	0.93	2.46	< 32	0.118	0.020
2	94.33	1.11	2.32	< 31	0.141	0.018
average	94.32	1.02	2.39	< 31.5	0.130	0.019

* The conversion is defined here as the percentage of carbon weight loss with respect to the fresh ST1. By this definition, the fresh ST2 is about 5% conversion due to pre-oxidation.

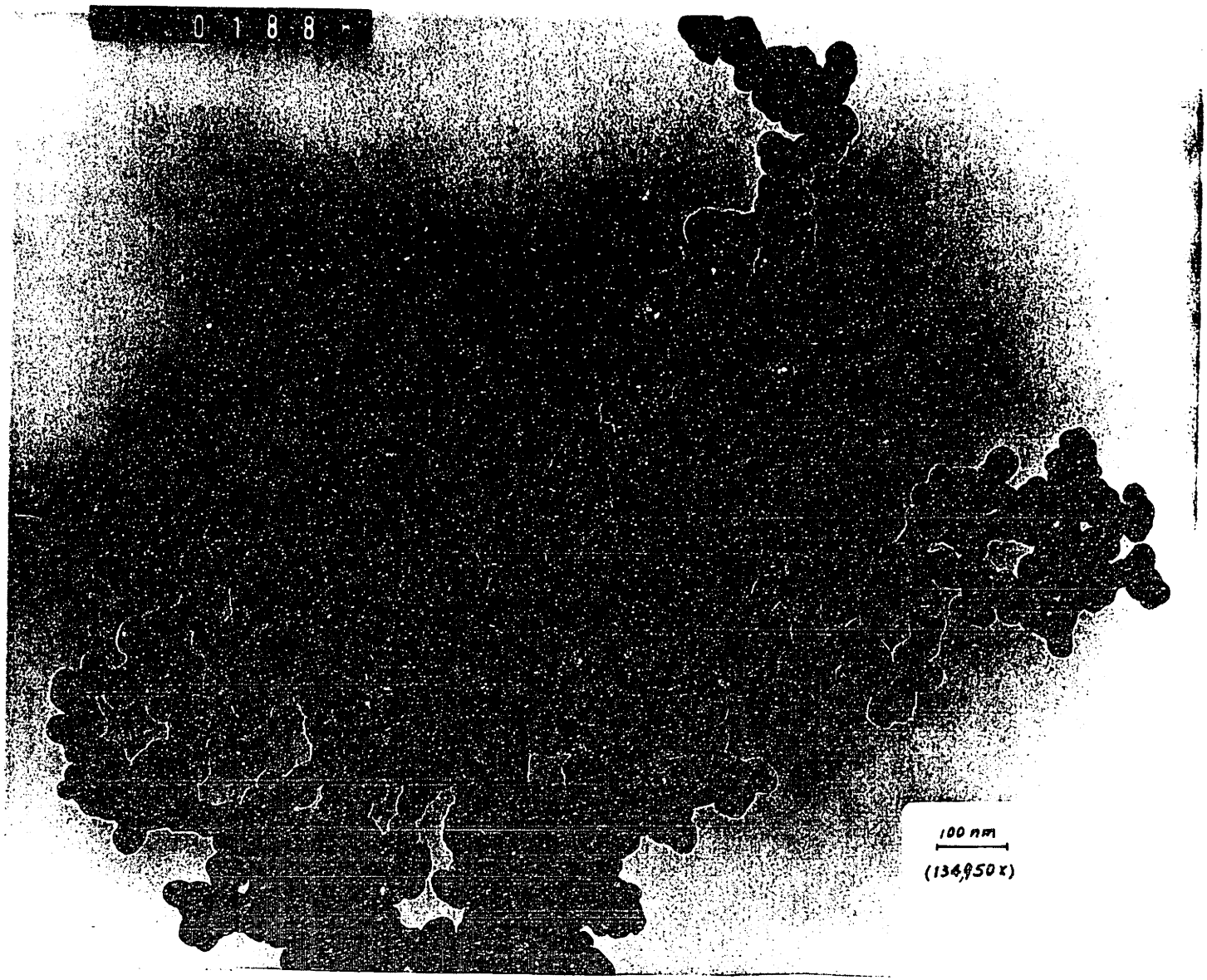

Fig. 2.1 Transmission electron micrograph of the fresh ST1.

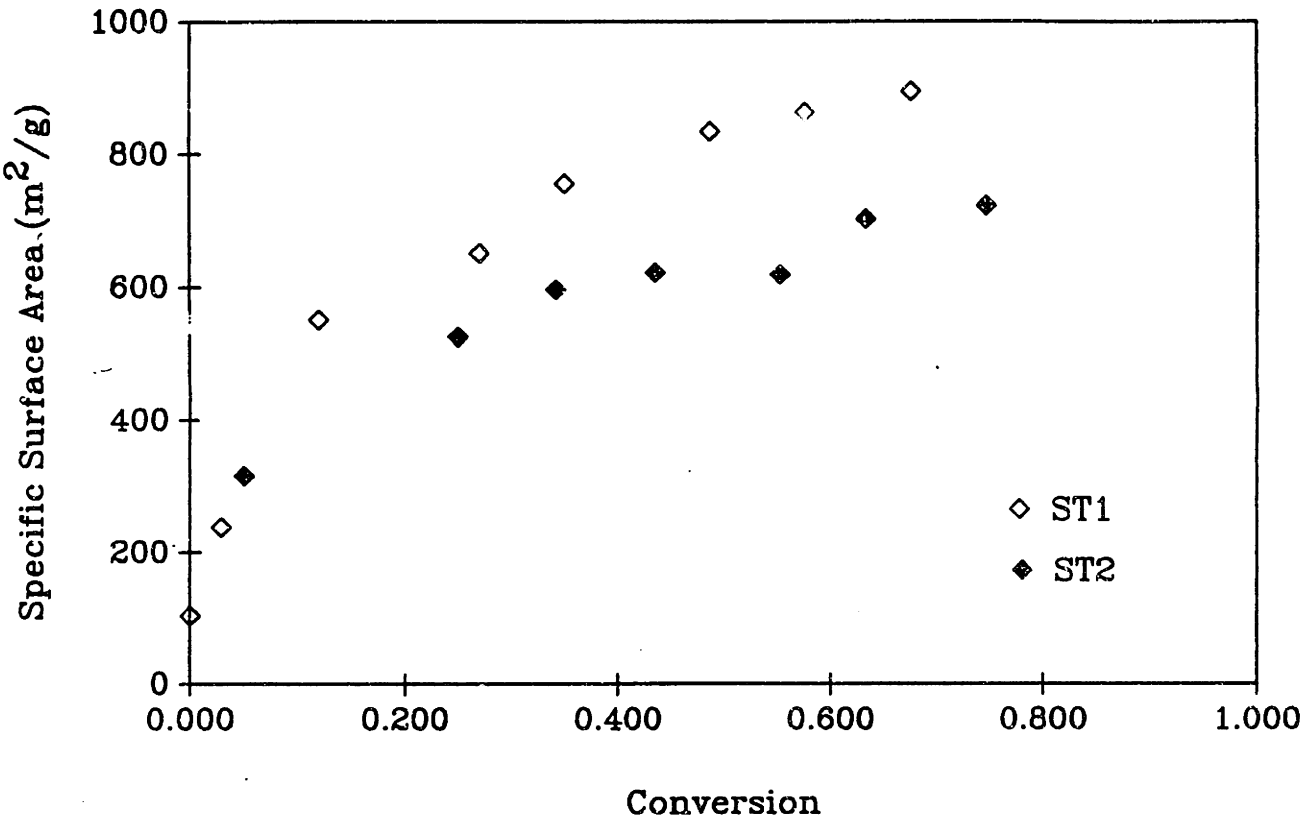

Fig. 2.2 Specific surface areas of ST1 and ST2 at different conversions.

2.12 Catalyzed Soot

The catalytic soot sample, referred as ST2 hereinafter, was made by directly adding calcium to ST1 using ion exchange technique. Pre-oxidation of the fresh ST1 at 733 K for about 90 minutes in one atm air (which is corresponding to about 5% conversion) was necessary to obtain sufficient exchange capacity [49]. The ion exchange reaction was conducted at T = 297 K for approximately 3 hours in a continuously stirred 0.64 M calcium acetate solution to which a small amount of calcium hydroxide had been added to raise the initial PH value to about 10.0. The whole reaction process was monitored by a PH meter, and the total amount of calcium added on soot particles was 2% by weight, calculated from the initial and final PH values of the solution [49] (see Appendix A). After the exchange process finished, the soot particles were vacuum-filtered from the solution, and vacuum-dried at 333 K for about 12 hours to form so-called 'fresh' ST2.

The calcium incorporated by the ion exchange technique will be well dispersed on the carbon surface [49],[56]. Floess [49] reported in his thesis that the catalyzed char prepared by the ion exchange exhibits the strongest catalytic effect among the three methods of calcium addition investigated.

Surface areas of ST2 sample at different conversions, were determined similarly to those of ST1, and plotted in Fig. 2.2. (see also Chapter 3 for detail).

2.13 Gases

All inert and reactant gases were purchased from Matheson Gas Products Inc. Liquid CO_2 (SFC grade) was used as adsorbate in the physisorption experiments. Pure N_2 (O_2 free grade) and air (CO_2 free grade) were used as inert and reactant gases, respectively, for the TGA system. Pure Ar (UHP grade) and a gas mixture of 21% Ar and 79% O_2 were used as inert and reactant gases, respectively, in the tube-furnace-MS and TGA-MS experiments. The calibration gas for MS was a gas mixture containing 215 ppm CO and 192 ppm CO_2 and balanced by Ar.

2.2 Experimental Apparatus

Reactivity data were obtained either by measuring the weight change of the carbon sample as a function of time with a Cahn Model 113 thermogravimetric analysis system (TGA), or by measuring the CO and CO_2 gaseous products with a HP 5970A series mass spectrometer (MS). The TGA is able to accurately measure a weight change on a sample amount as small as 10 μg, and MS is capable of detecting a minimum gas concentration on the order of 10 ppm. The reactivity measured by TGA is consistent with that measured by MS (see Fig. 2.3).

Carbon oxidations took place either in the TGA furnace or in a small-tube furnace. Both furnaces have the same type K thermocouple and are able to control the furnace temperature within 1 K around the set point. Under the same experimental setting, soot samples were oxidized at almost the same rate in both furnaces (see also Fig. 2.3), which makes the reactivity data obtained from these two furnaces compatible.

2.21 Thermogravimetric Analyzer

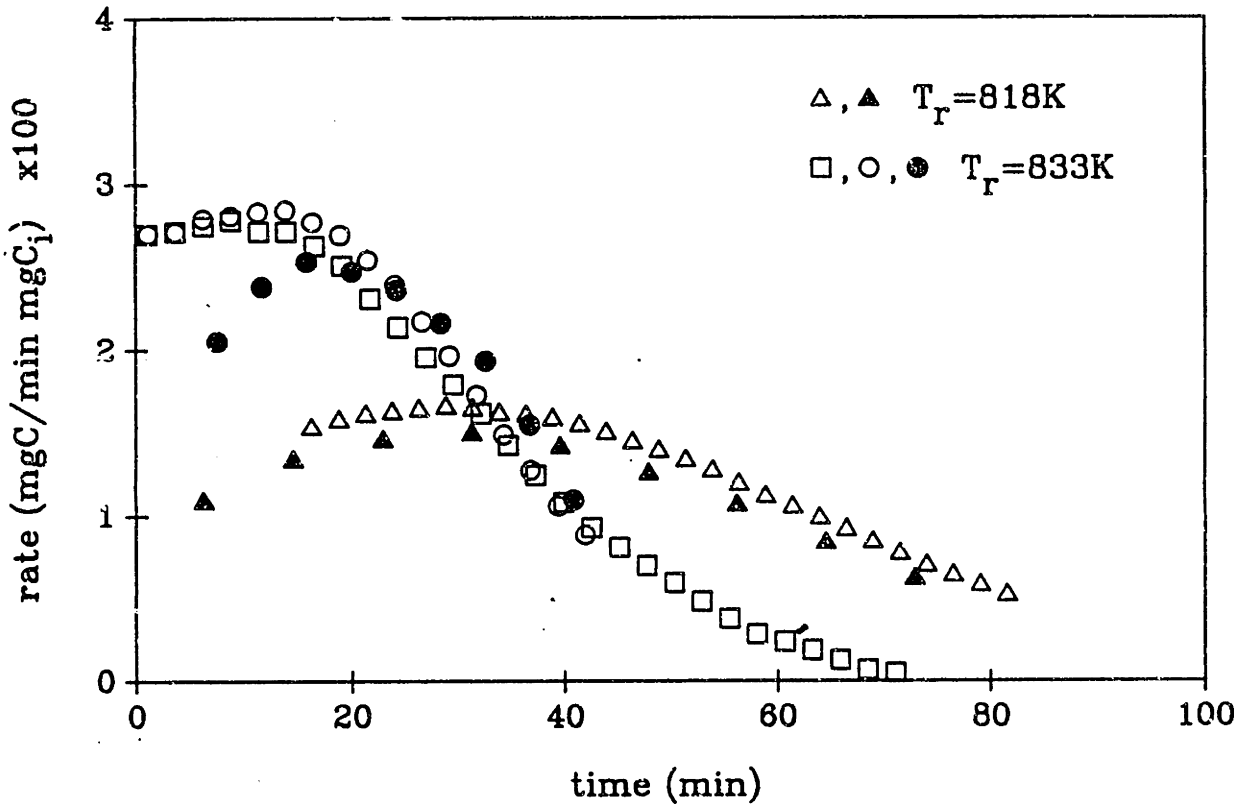

Fig. 2.3 Comparison of reactivities measured by TGA and MS.

key: □ — TGA-MS run, measured by MS, m_i = 3.43 mg
● — TGA-MS run, measured by TGA, m_i = 3.43 mg
o — Tube-furnace-MS run, measured by MS, m_i = 1.65 mg
Δ — Tube-furnace-MS run, measured by MS, m_i = 16.4 mg
▲ — TGA run, measured by TGA, m_i = 5.98 mg

A schematic of the thermogavimetric analyzer (TGA) system is shown in Figure 2.4 [49]. The microbalance, mounted inside a Pyrex glass housing, is an electro-mechanical transducer that measures the force applied onto the balance beam by the current a motor coil needs to counterbalance the applied torque. The ultimate sensitivity of the balance is about 0.1 μg. The quartz furnace tube is 1" in diameter with a 1 1/2" section of heavy wall 26 mm quartz tubing attached to one end. This end was precision ground and polished to the correct outside diameter to provide a tight connection to the Cajurn o-ring fitting. A type K thermocouple is mounted through the bottom of the furnace tube, which provides the input signal for the temperature controller. The sample pan is supported by a hang-down wire of 0.1 mm nichrome. Since the platinum sample pan was found to significantly catalyze the gas phase CO oxidation at about 773 K [61], a 1 x 1 cm^2 square ceramic sample pan was used to replace the platinum sample pan described in [49]. Gases from a gas flow system (see section 2.25), either inert or reactant, enter the TGA with a constant flow rate of 200 cc/min through the inlet port mounted just above the furnace tube, and exit at the bottom of the furnace tube (see Fig. 2.4). The pressure in the TGA is kept about 12 cm H_2O above atmospheric during operation, monitored with a water manometer that has a safety release at 42 cm H_2O. A detailed description about the TGA system can be found in Floess' thesis [49].

The furnace tube is heated with a standard resistance furnace. The temperature is controlled with a Micricon 823 process controller, which is able to maintain a steady state temperature within 1 K of the set point.

The weight versus time data were recorded on a Bascom-Turner model 4110 digital recorder and data storage system, which has a

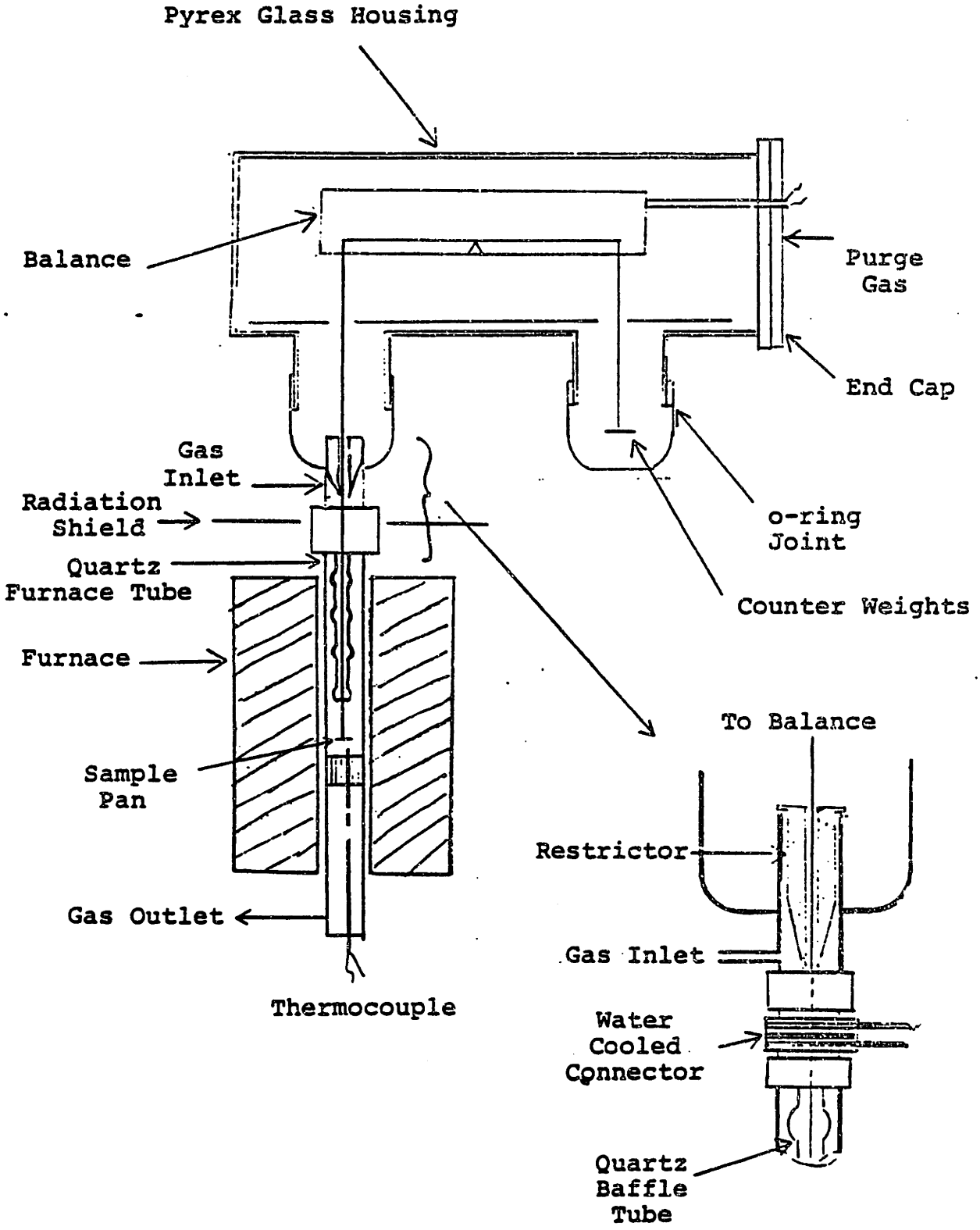

Fig. 2.4 A schematic of the thermogravimetric analyzer (TGA) [49].

maximum data acquisition rate of 100 milliseconds per datum point. The derivative of the TGA data (weight vs. time) was calculated using software available in the Bascom-Turner operating program. Smoothing of the derivative data was done using a 5 point moving average routine also available in the software. A visual best fit curve was drawn through the smoothed data and numerical values for the rate were determined directly from the graph paper.

2.22 Mass Spectrometer

The mass spectrometer (MS) used in this study is a HP 5970A series model, connected with a HP 59970C ChemStation to control the MS operation. An internal autotune program, which provides adequate sensitivity for any mass in the range of 10-800 m/z (amu) is employed to tune the MS using a tuning calibration compound PFTBA (perfluorotri-n-butylamine). The MS was operated under a vacuum pressure of $\sim 2.5 \times 10^{-6}$ torr.

During a MS run, the SIM (Selected Ion Monitoring) mode, which provides an accuracy of 0.05 m/z (amu), was used to analyze mass 28 and mass 44 signals at an acquisition rate of 2.5 seconds per datum point. The mass 28 and mass 44 signals can be displayed as a function of time on the ChemStation monitor and stored in the ChemStation hard disk. These MS data can be also transferred to a 3.5" floppy disk or printed out for further analysis.

CO concentration obtained from the MS is determined by subtracting 10% of the mass 44 signal from the mass 28 signal, while CO_2 concentration is determined directly from the mass 44 signal. Under the normal

experimental condition, sensitivity of the MS measurement is on the order of 10 ppm.

2.23 Characterization of the TGA reactor

The TGA reactor is made of a quartz tube of 12" long and 1" in diameter. The temperature profile in the reaction zone (near the sample pan) is virtually uniform [49]. Temperature measurements with a dual bead thermocouple assembly (ratio of bead diameters = 5) showed that the effective wall temperature and the gas temperature are approximately the same at gas velocities below 300 cc/min (see Fig 2.5a). The axial temperature profile near the sample pan region is presented in Fig. 2.5b.

Although it drifts due to thermal buoyance as the temperature in the TGA reactor changes, the base line of the TGA system is very stable under isothermal condition. Fig. 2.6 shows a base line taken at 598 K with nitrogen (200 cc/min) flowing through the TGA reactor. Over a two hour time period, the change in the base line is confined within 5 μg.

Kinetic experiments were made with samples weighing from 0.5 mg to 6 mg, depending on the temperature (i.e., the reaction rate) at which the measurement was made. Sample size was modulated to minimize the effects of bulk phase heat and mass transfer at different reaction rates. Calculations presented in [49] show that the effect of heat and mass transfer is negligible at reaction rate below ~ 0.2 mg/min. For the soot materials aforementioned in the Section 2.1, the effect of inter-particle diffusion between soot particles can be ruled out by the fact that reactivity of the soot material was independent of sample size in the TGA experiments (see Fig. 2.7); and the effect of intra-particle diffusion can also

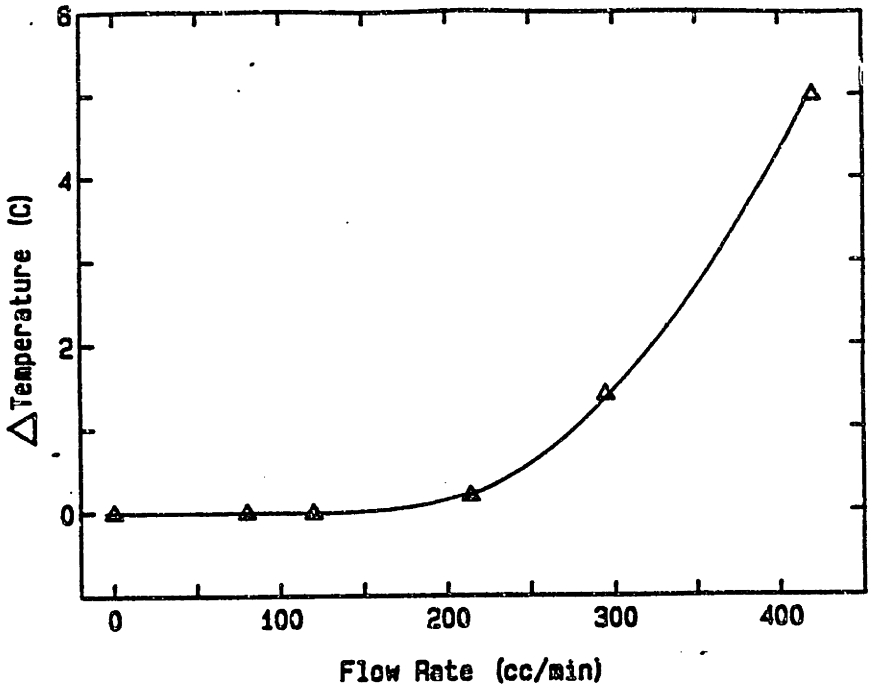

Fig. 2.5a The effect of gas velocity on the temperature difference measured by a dual bead thermocouple assembly [49].

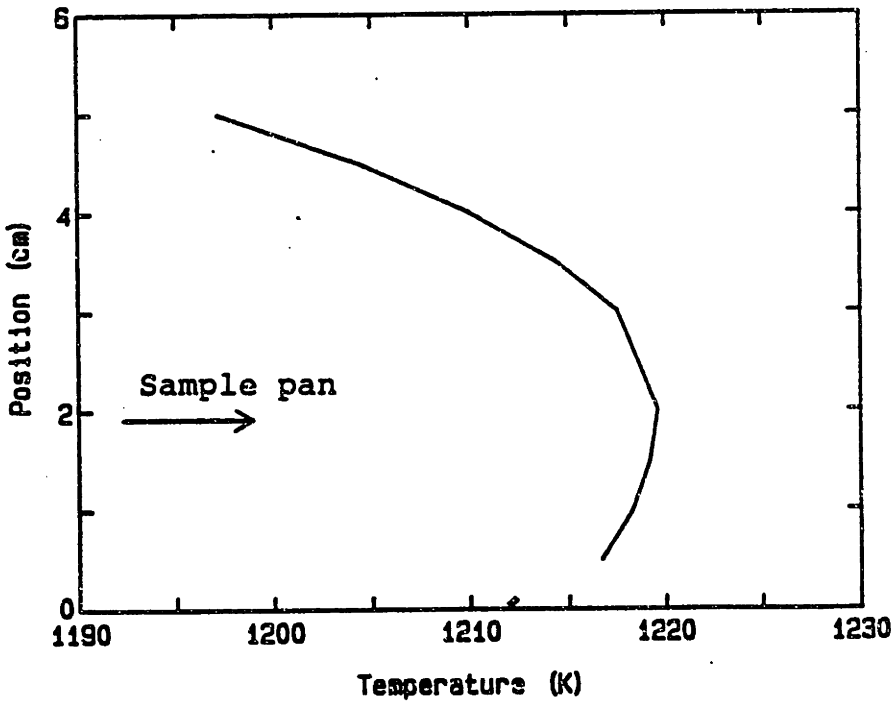

Fig. 2.5b Axial temperature profile in the reaction zone of the TGA [49].

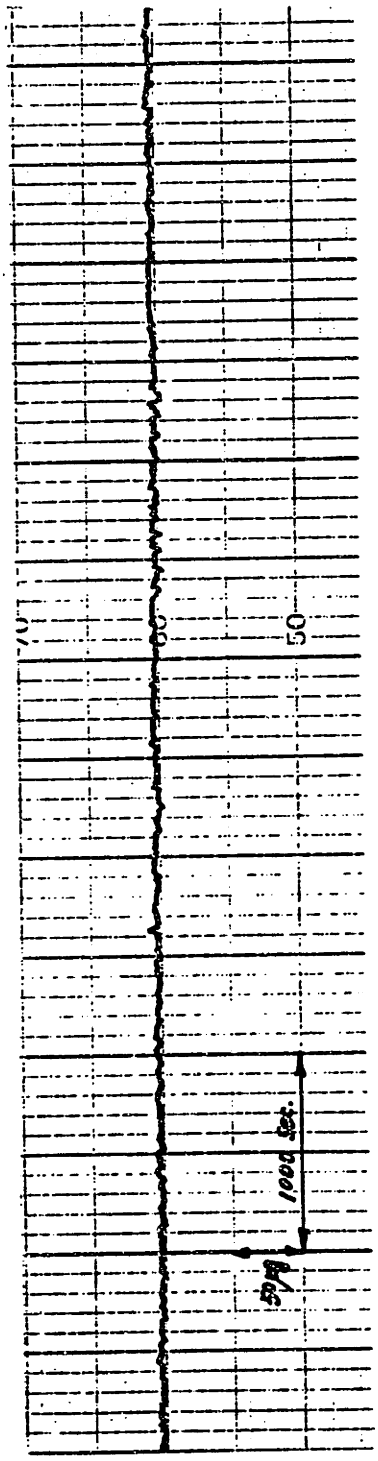

Fig. 2.6 Background signal of the TGA.
(N_2 flow rate=200 cc/min; T=598K)

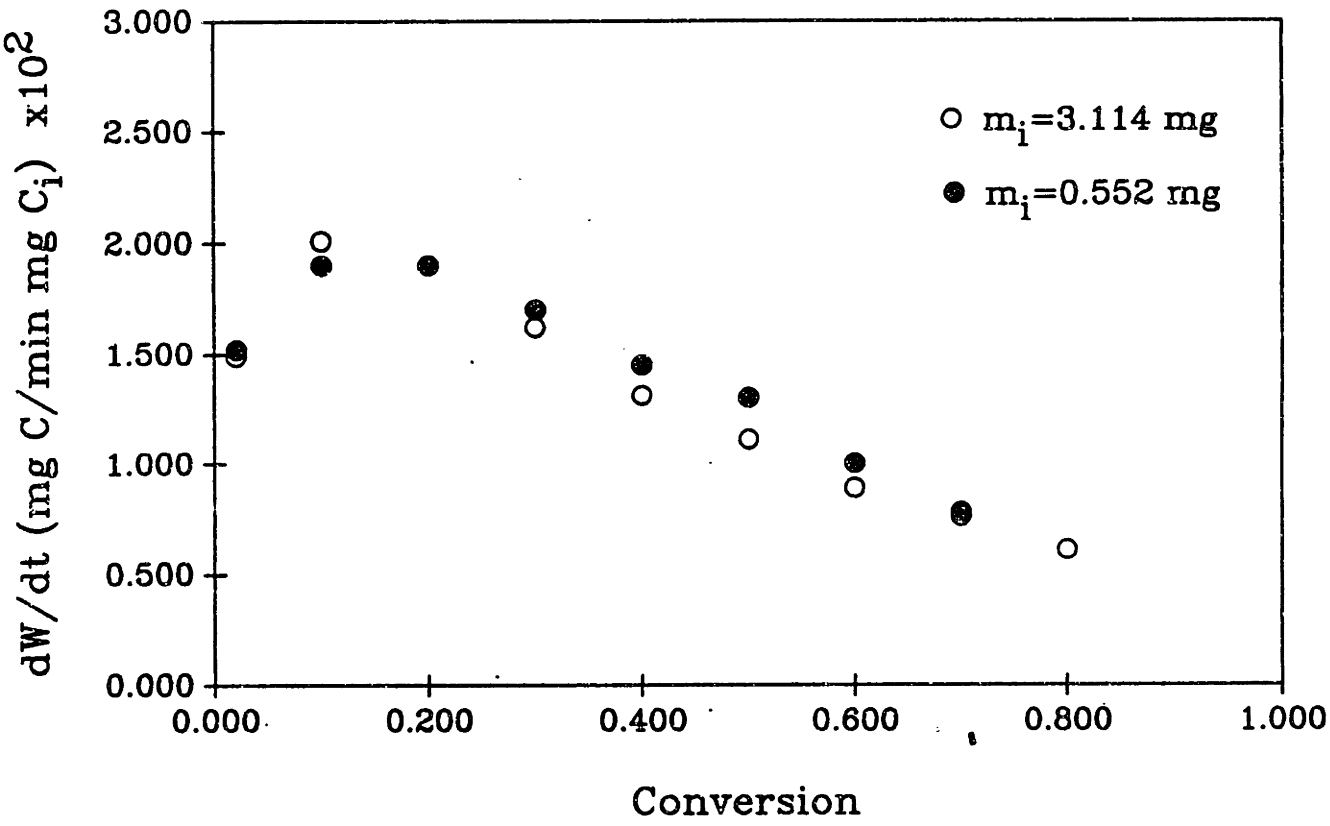

Fig. 2.7 Reactivity of ST2 in TGA system for different sample sizes.

be neglected from the Thiele modulus calculation for the temperature range used in our experiments (see Appendix B).

Gas flow through the vertical furnace tube is in a mixed laminar free-convection regime. At 1000 K and a flow rate of 200 cc/min of air, the Reynolds number based on the inside tube diameter is 5.4. Because of the baffle in the furnace tube, exact calculation of the Raleigh number is difficult. If a temperature differential of 100 K and a length of 5 cm are assumed, the corresponding Raleigh number is 8000. These values place the flow well within the mixed laminar free-convection regime [62]. Thus, small changes in the gas velocity will not significantly alter the mass transfer between the solid and the fluid. This was observed experimentally by Wigmans et al. [63] who report that the mass transfer rate does not change significantly if the flow direction in the reactor tube is changed.

2.24 Characterization of the Tube Furnace Reactor

The tube furnace reactor shown in Fig. 2.8 consists of a Lindberg 55035 electrical resistance furnace and a 1" o.d. and 22" long quartz furnace tube horizontally resting between the resistance elements. A 7/8" o.d. and 1 1/2" long quartz tube, which can easily slide in and out the furnace tube, serves as a sample holder in which carbon sample is sandwiched between two pieces of quartz wool (see also Fig. 2.8). A type K thermocouple, the same as the one used in TGA furnace, is placed very close to the sample providing a good measure of temperature near the reaction zone. The furnace temperature is controlled with an Omega 49 model controller which is able to maintain a steady state temperature within 1 K around the set point. Gases from a gas flow system (see section

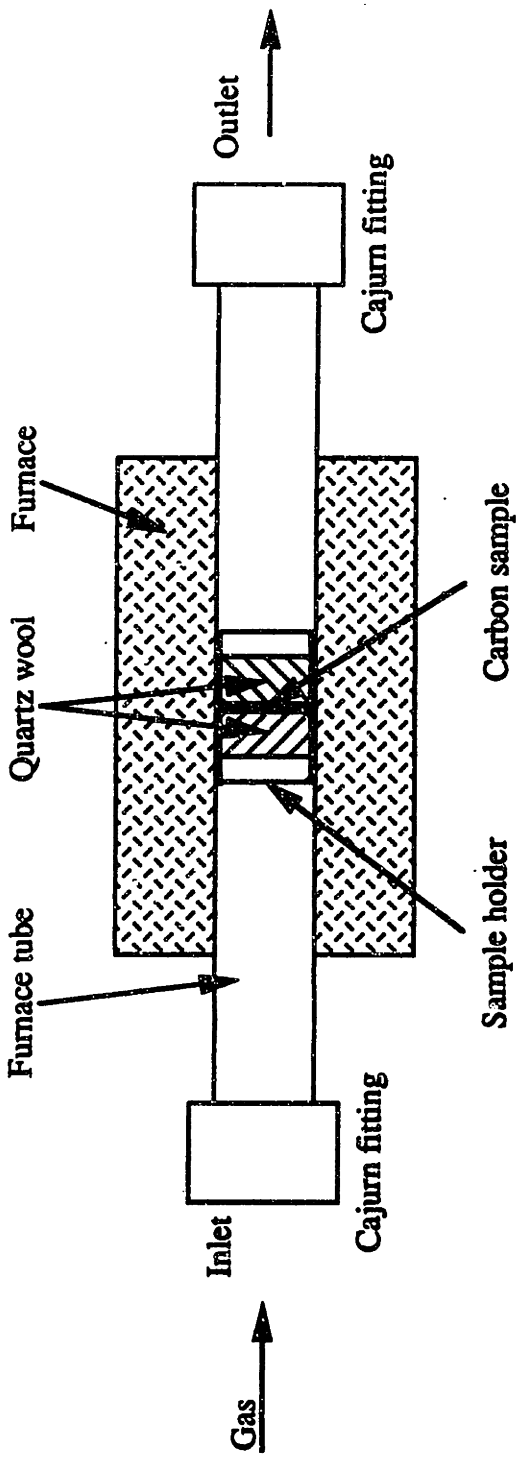

Fig. 2.8 A schematic of the tube furnace reactor.

2.25), either inert or reactant, enter the furnace tube with a constant flow rate of 200 cc/min from the left end and exit from the right end, then go to the MS for analysis. (see also Fig 2.8). The reactor is operated at the atmospheric pressure.

The axial temperature profile within the furnace was measured and presented in Fig. 2.9. It can be seen that the furnace temperature is uniform within ±1 inch from the carbon sample where the reaction took place. It was also found that the temperature field of the reactor does not change as the gas flow rate drops from 200 cc/min to 70 cc/min.

The background signal of the tube furnace reactor is quite stable over time and does not vary with furnace temperature. Fig. 2.10 shows background signals measured by the MS from a blank run (with everything in the reactor except carbon sample). As the furnace temperature increases from 296 K to 11273 K with a heating rate of ~20 K/min, no significant signal drifting was observed (see Fig. 2.10). (The signal jumping upward between t ~48 min and t ~68 min in Fig.2.10 is due to the electronic problem in the MS.)

Kinetic experiments in the tube furnace reactor were made with sample size from ~10 mg to ~20 mg. Again, the sample size was modulated to minimize the effects of heat and mass transfer during the experiments. Since soot samples were oxidized at the same rate in both TGA and tube furnaces (see Fig. 2.3), the oxidation conditions in the tube furnace would be similar to those in the TGA furnace. According to the discussion in Section 2.23, no heat and mass transfer effects exist in the TGA furnace. These effects, therefore, will not be expected to exist in the tube furnace under the similar experimental conditions.

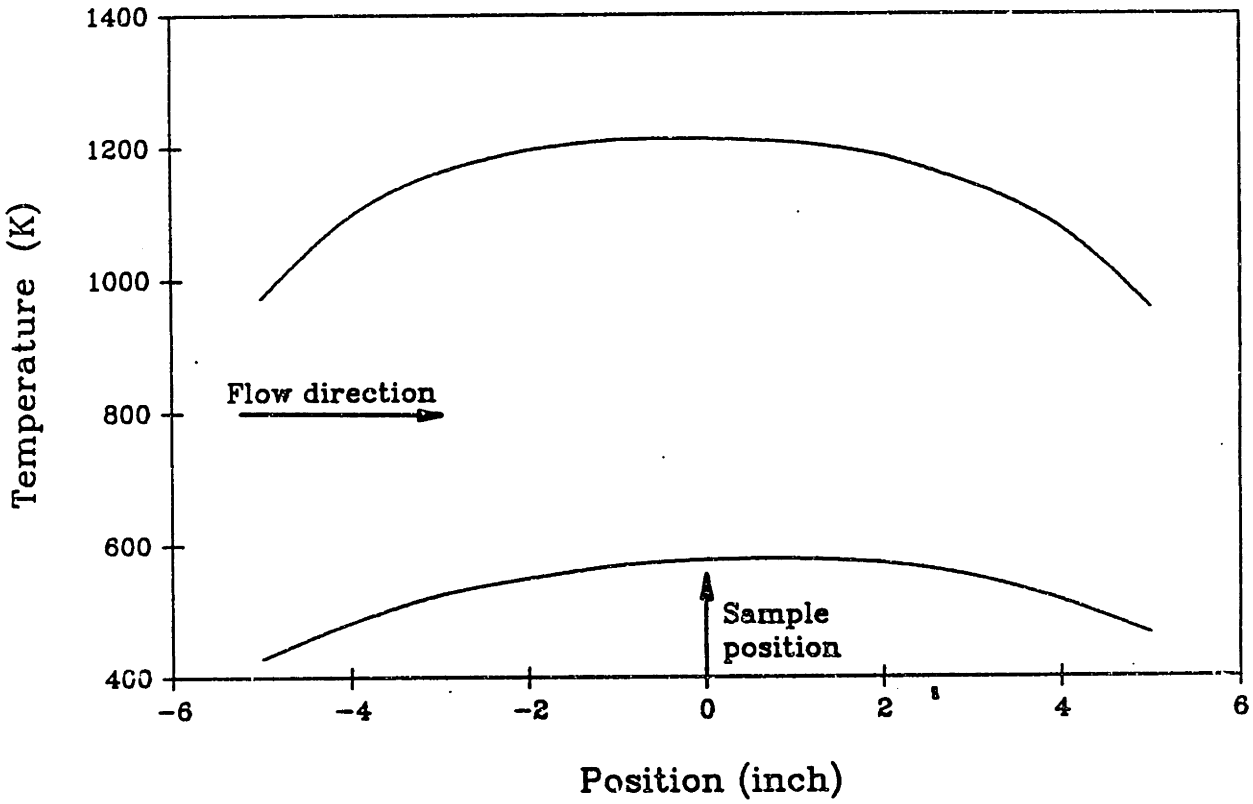

Fig. 2.9 Axial temperature profiles in the tube furnace reactor at two different temperatures of carbon sample.

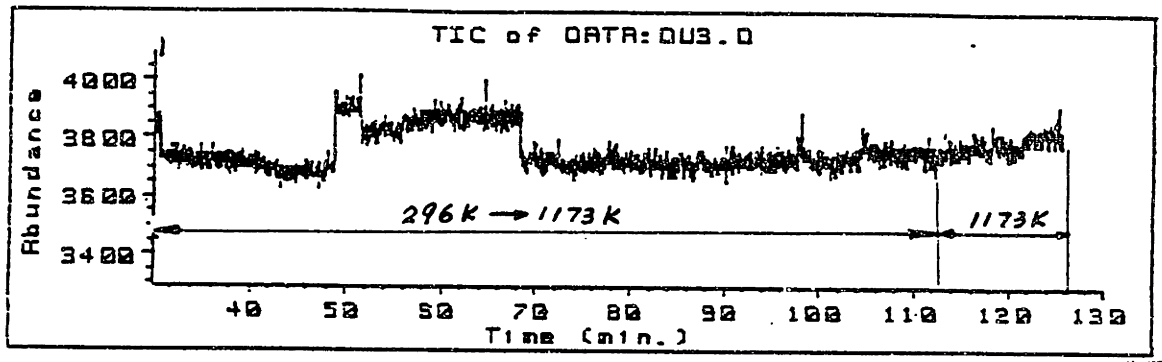

Fig. 2.10 Background signal of the tube furnace reactor.
(Ar flow rate=200 cc/min; furnace heating rate≈20 K/min)

Note: The jump upward between 48 min and 68 min is due to the electronic problem in the MS.

Time (min)	m/z=28 (arbitrary unit)	m/z=44 (arbitrary unit)
32.51	2250	1491
86.36	2157	1553
114.25	2200	1566
120.36	2181	1584
124.84	2237	1594

Carbon sample in the sample holder spreads little in the axial direction, so the tube furnace reactor can be considered as a differential reactor. Several tests were carried out to make sure that concentration profiles of CO and CO_2 would not be distorted as the gas stream traveled from the tube furnace to the MS sampling port. These tests showed that a set of pulse signals introduced at the inlet of the tube furnace could be well identified in both shape and intensity by MS at two different furnace temperatures (see Fig. 2.11a,b), and no distortions of these pulse signals were observed in MS.

2.25 Gas Flow System

The gas flow system, shared by the TGA and tube furnace, is shown schematically in Fig. 2.12 [49]. It consists of a reactant gas mixing system and a separate inert gas line. Both of these lines are directed to the inlet of the TGA or the tube furnace via a 4-way ball valve.

The gas mixing system consists of four ports that are connected into a mixing tee and four alternative bypass lines that are connected to a vent. The entire system is constructed from 1/8" stainless steel tubing; the on-off valves are ball valves, and the control valves are Nupro fine metering valves. Flow rates are adjusted manually and are measured with Brooks Model 5810 thermal mass flowmeters located on the high pressure side of each control valve. The flowmeters were calibrated against a standard laboratory bubble meter.

2.3 Experimental Set-ups and Procedures.

Three different experimental set-ups were employed for this thesis work:

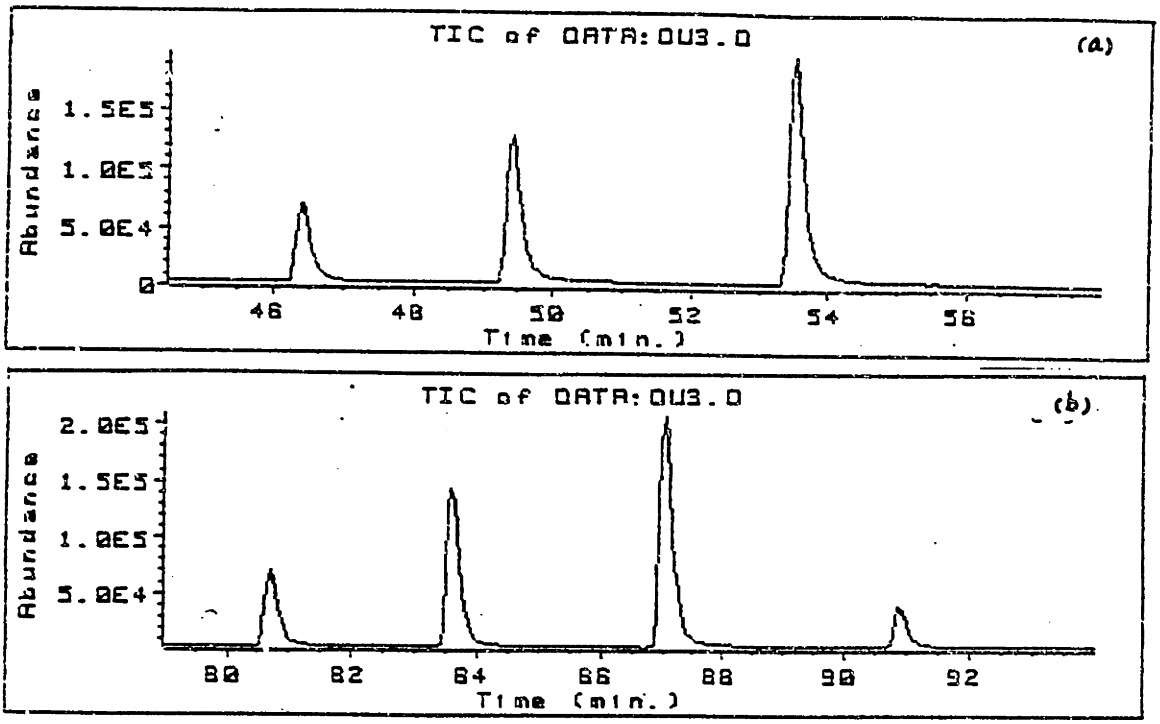

Fig. 2.11 Pulse signal detected by MS.
(a) Furnace temperature = 296 K, relative gas volume corresponding to each peak is 1:2:3
(b) Furnace temperature = 918 K, relative gas volume corresponding to each peak is 1:2:3:0.5

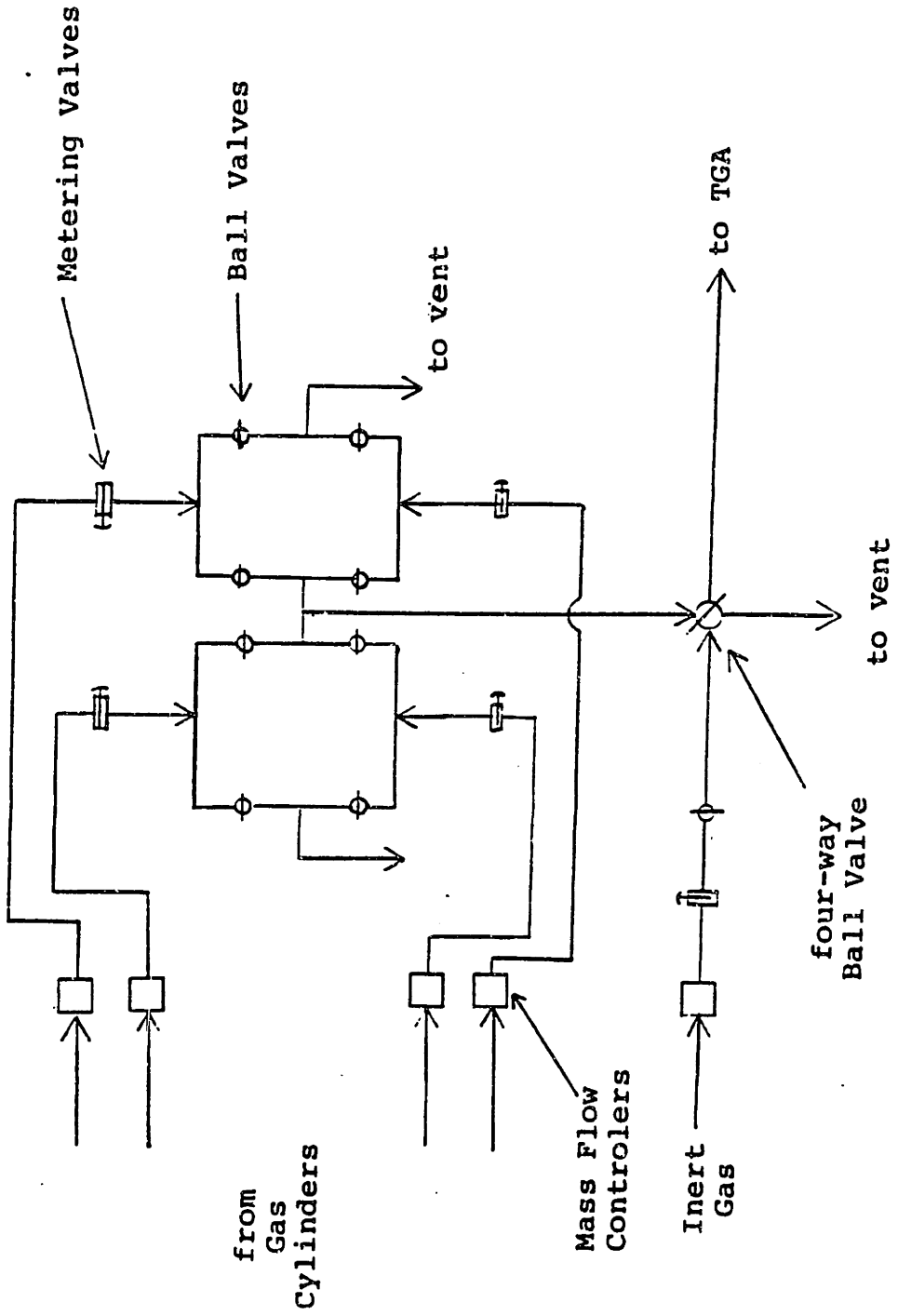

Fig. 2.12 A schematic of the gas flow system [49].

1) TGA alone (see Fig. 2.13a): TGA experiments were conducted isothermally under two modes, the physisorption mode and the reaction mode, to obtain CO_2 isotherms and reactivity data of the soot materials. In the physisorption mode, CO_2 adsorption isotherms of a soot sample were measured at room temperature in the TGA system, and surface area of the sample was calculated from the corresponding CO_2 isotherms using Dubinin-Polanyi equation. In the reaction mode, a soot sample in the TGA furnace was heated at 25 K/min in inert gas to a heat-treatment temperature, 1173 K, held isothermally for about 15 minutes, and then cooled down to the reaction temperature without any intermediate exposure to room air. The reaction run was started by switching the incoming gas from inert to reactant.

2) TGA-MS (see Fig. 2.13b): In the TGA-MS run, soot sample was placed and reacted in the TGA furnace, and reaction rate was independently measured by the TGA and MS. The experimental procedure is the same as that in the TGA experiment.

3) Tube-furnace-MS (see Fig. 2.13c): This arrangement was used for collecting the information about CO and CO_2 generations under oxidation and desorption conditions. In the tube-furnace-MS experiments, soot sample was placed in the center of the tube furnace, and the gas products were continuously sampled and analyzed by MS at an acquisition rate of 2.5 seconds per datum point. Only CO and CO_2 gas components were analyzed in MS. (The CO data from the MS were corrected by subtraction 10% of mass 44 signal from mass 28 signal, and no correction was made for the CO_2 data.) The experimental procedure for the oxidation runs is similar to that depicted in TGA runs. And the procedure for the desorption (TPD) runs is described as the following: Soot sample was heat-treated and

partially reacted according to the same procedure in the oxidation runs, then the sample was cooled in reactant to the initial desorption temperature T_i, which is 598 K for ST1 and 473 K for ST2. After the sample temperature reached T_i, the incoming gas was switched from reactant to inert, and the system was purged for about 30 minutes. Finally, the TPD run was started by ramping the temperature from T_i to either 1173 K or 1223 K in inert gas. Calibration of CO and CO_2 signals in MS was made after each tube-furnace-MS run, using a pre-calibrated CO CO_2 mixture.

After each fresh carbon sample was placed in either the TGA furnace or the tube furnace, the whole system was purged with inert gas for about 45 min. The purging flow rate is set at 200 cc/min for the tube furnace and about 1000 cc/min for the TGA system.

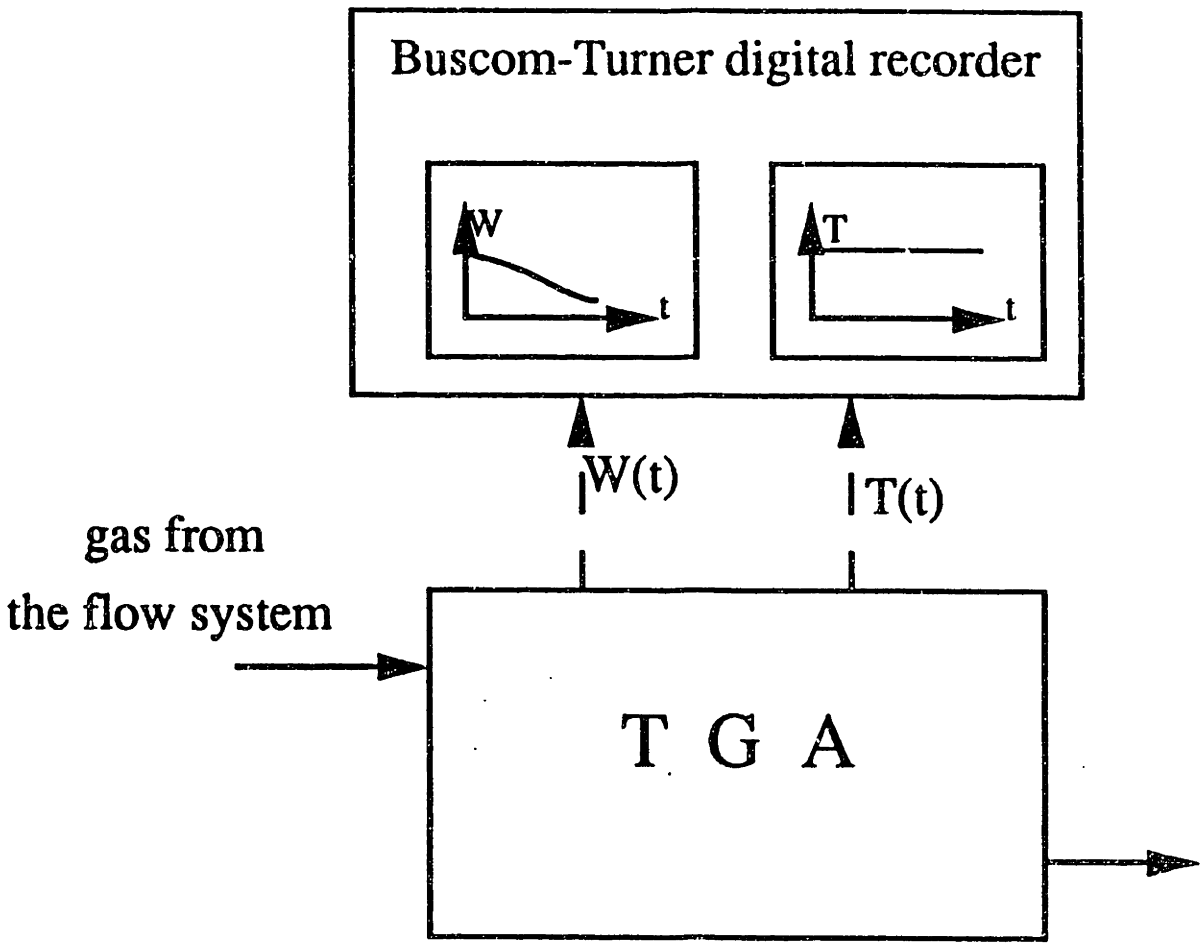

Fig. 2.13 Experimental set-up
(a) TGA arrangement

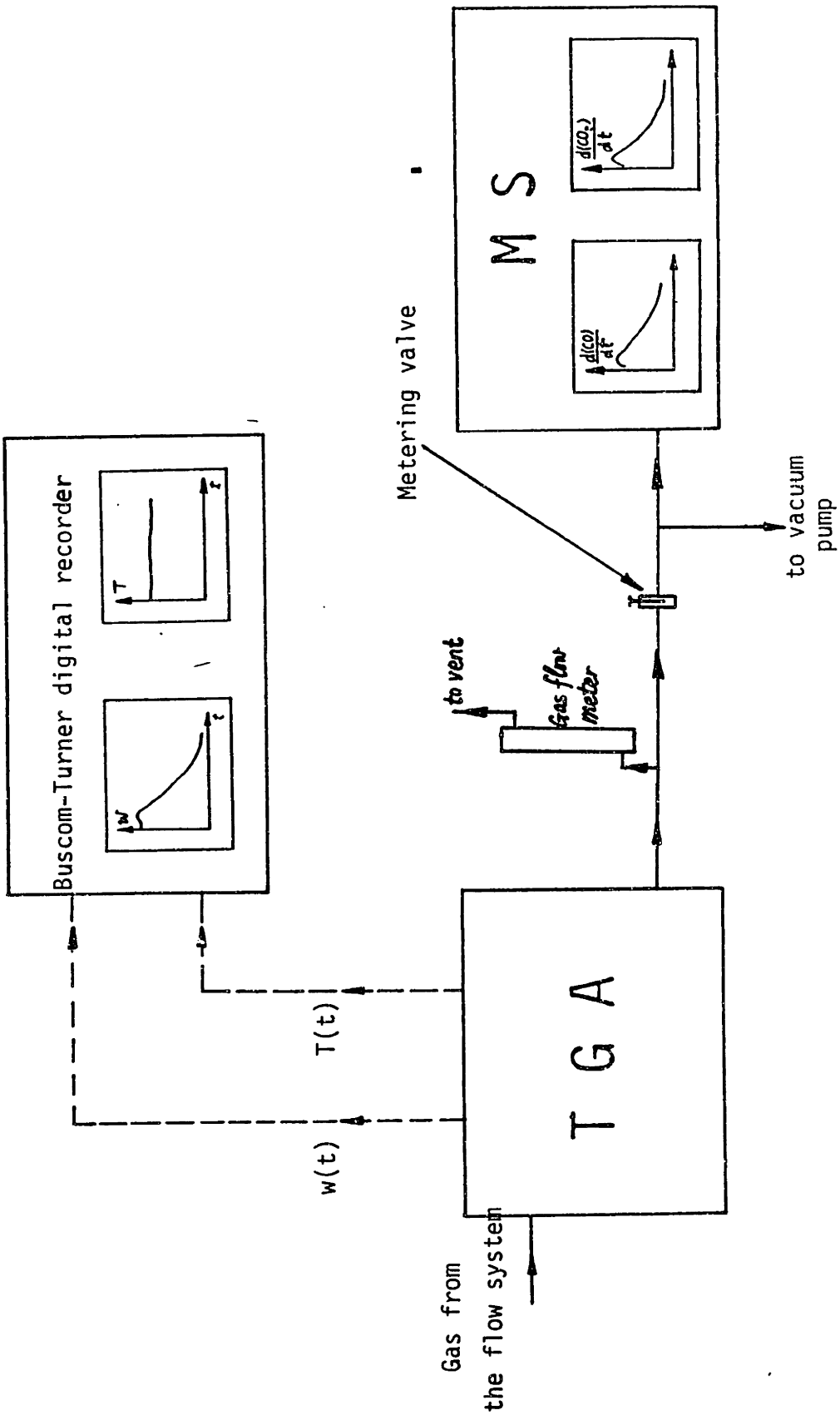

Fig. 2.13 Experimental set-up
(b) TGA-MS arrangement

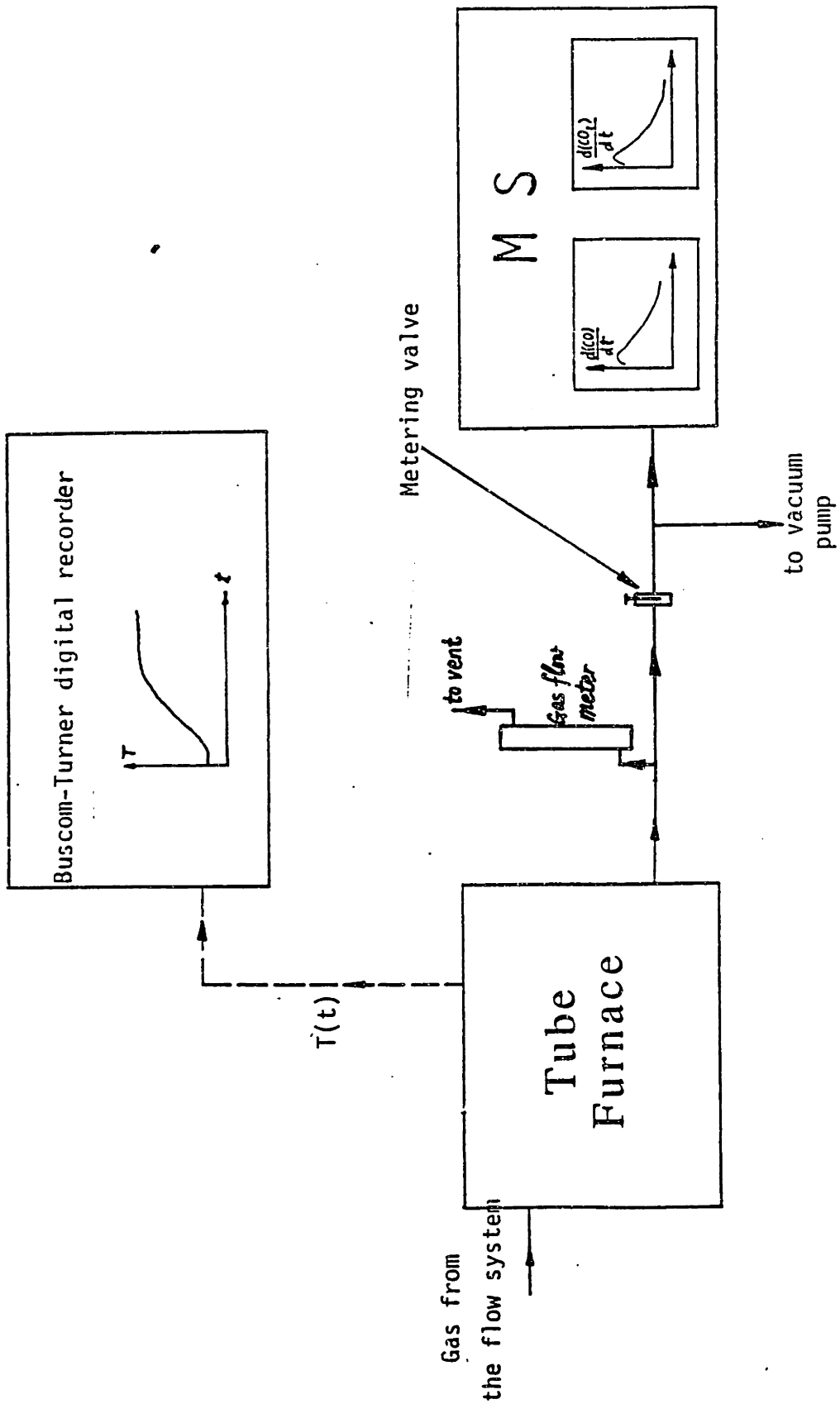

Fig. 2.13 Experimental set-up
(c) Tube-furnace-MS arrangement

Chapter 3. Surface Areas of the Soot Materials and Their Evolution During Oxidation

For a solid-gas reaction, the reaction rate is proportional to the solid surface area. Hence the information about the surface area of carbon is necessary for modeling of carbon oxidation.

3.1 Methodology

In this study, the surface areas of ST1 and ST2 at different conversions were calculated from CO_2 adsorption isotherms using Dubinin-Polanyi equation. (The area of an adsorbed CO_2 molecule was taken to be 24.4Å [64,65], and the saturation pressure of CO_2 at 297K was 62.33 atm according to $P_{sat} = 10^{-874.34/T+4.7386}$ (atm)). These CO_2 adsorption isotherms were determined in the TGA system by a gravimetric method. There are two advantages of the gravimetric method over the common used volumetric method: (1) This method is capable of dealing with small sample size, owing to the weighing sensitivity of the TGA system. (2) Both CO_2 adsorption and partial conversion of the soot sample can be carried out in the same TGA system to avoid any transportation of the sample.

A surface area measurement involves a series of measurements of CO_2 adsorption isotherms in different CO_2 partial pressures at 297 K. The set of CO_2 partial pressures used in the surface area study is 0.1, 0.2, 0.35, 0.5, and 1.0 atm.

A fresh soot sample, after its surface area was measured in the TGA, was partially oxidized isothermally in the same system to a desired conversion, and then this partially converted sample underwent a surface

area measurement. This area-measurement-oxidation-area-measurement cycle continued on the same sample until about 70% conversion was reached. The partially converted soot sample might have either 'clean' surface (desorption in inert gas (N_2) up to 1173 K after the oxidation) or oxygen partially covered surface (without desorption).

3.2 Accuracy of The Surface Area Measurements

The specific surface area of the soot sample was obtained from CO_2 adsorption isotherms, via a Dubinin-Polanyi plot. Two typical Dubinin-Polanyi plots are shown in Fig. 3.1a,b. The correlation coefficients in all Dubinin-Polanyi plots (including those not shown here) are at least 0.99, most of them are around 0.999, indicating little or no capillary condensation in the adsorption experiments.

A comparison was made between the surface areas obtained by the present gravimetric method and the conventional volumetric method. For the fresh ST1, a CO_2 area of 121 m^2/g was obtained by the gravimetric method. It is consistent with its N_2 BET area of 105 m^2/g obtained by a Quantasorb apparatus, and also agrees well with the N_2 BET data reported in the literature for the similar soot material [66].

3.3 Result

3.31 Surface Area Evolution of ST1

Fig. 3.2 shows the specific surface areas of ST1 at different conversions.* The surface condition of the soot sample, whether partially

---

* The conversion is defined as the same as in Chapter D2.

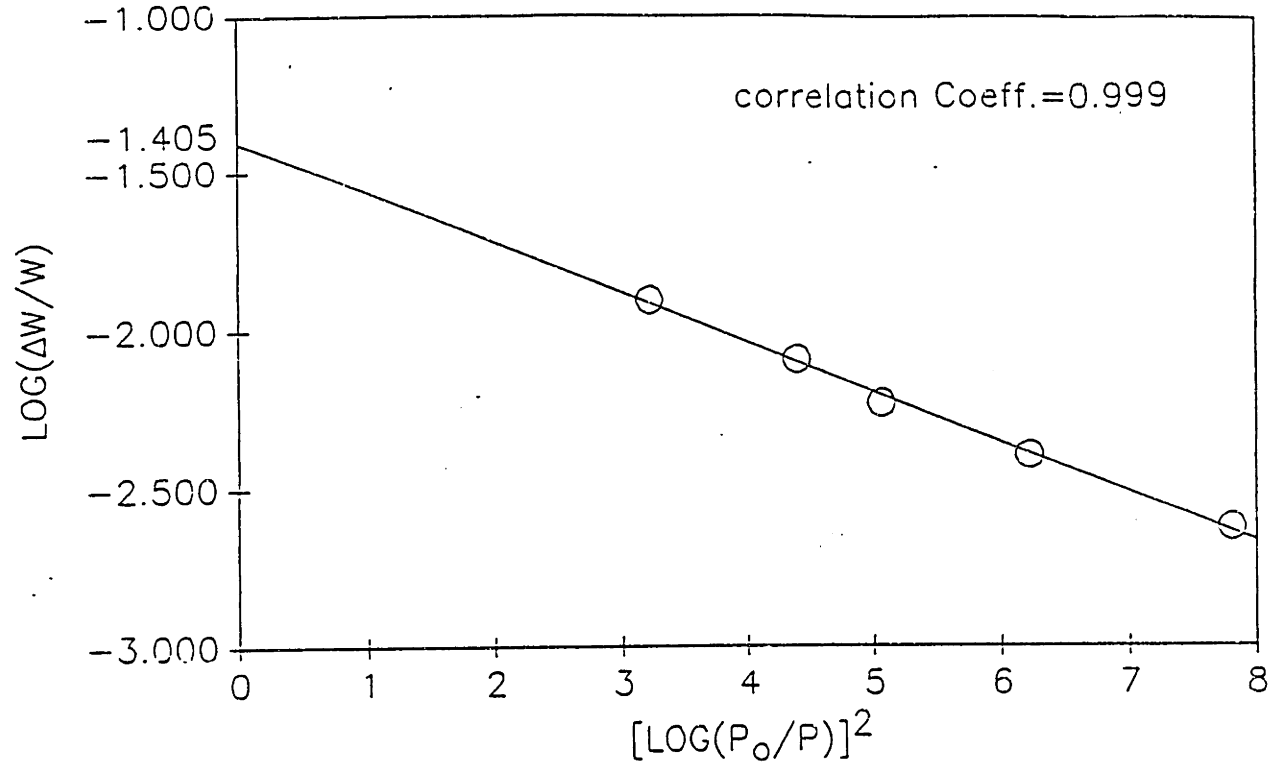

a) On the fresh non-catalytic soot.

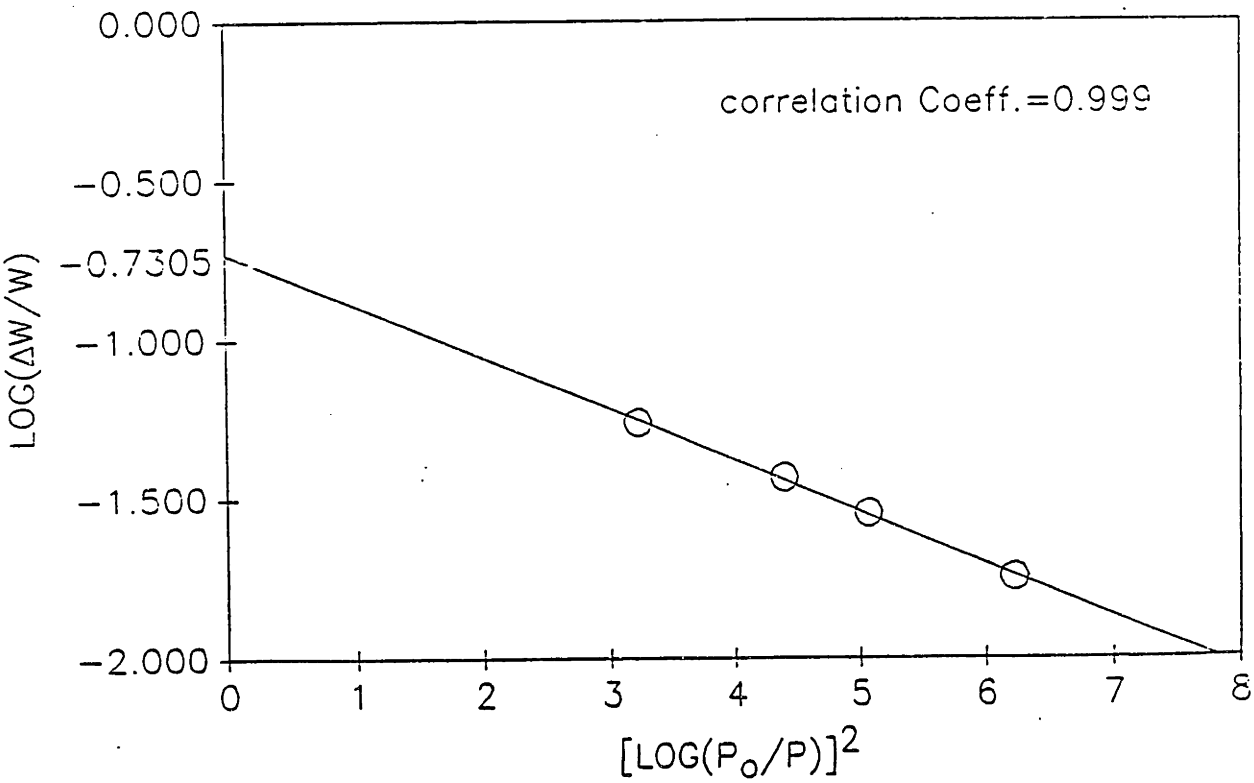

b) On the catalyzed soot after 25% conversion.

Fig. 3.1 Adsorption of CO_2 at 297 K.

covered by oxygen or clean, seems not to affect the surface area measurement. So, the surface area data will be presented without specifying its surface condition.

It is interesting to see from Fig. 3.2 that the surface area increases rapidly during the first 20% conversion. The moderate surface area at 0% conversion (121 m^2/g) implies that either micro-structure does not exist, or it is not accessible to the adsorbate (CO_2); and the measurable surface area results from the external of the soot particles. However, the high specific surface area (about 600 m^2/g) obtained at 20 % conversion indicates the existence of micropores in the partially converted soot, since this rapid increase in surface area can not be attributed in any way to the shrinkage of soot particle size during the reaction (see also Fig. 3.2).

3.32 Surface Area Evolution of ST2

Fig. 3.3 shows the specific surface areas of ST2 at different conversions. (The specific surface areas of ST1 are duplicated in the same figure for comparison.) The surface area evolution of ST2 sample exhibits the similar rapid increase during the first 20% conversion, and levels off at a relatively low value compared with those ST1 data.

3.4 Discussion

The rapid increase in surface area during the first 20% conversion was observed for both ST1 and ST2 materials (see Fig. 3.2 and 3.3). This surface area development during the oxidation can be explained by opening the inaccessible surface area *inside* the soot particle upon the chemical reaction. The micropores, which account for most of the surface area of the sample, may exist in the soot particle, but are not accessible

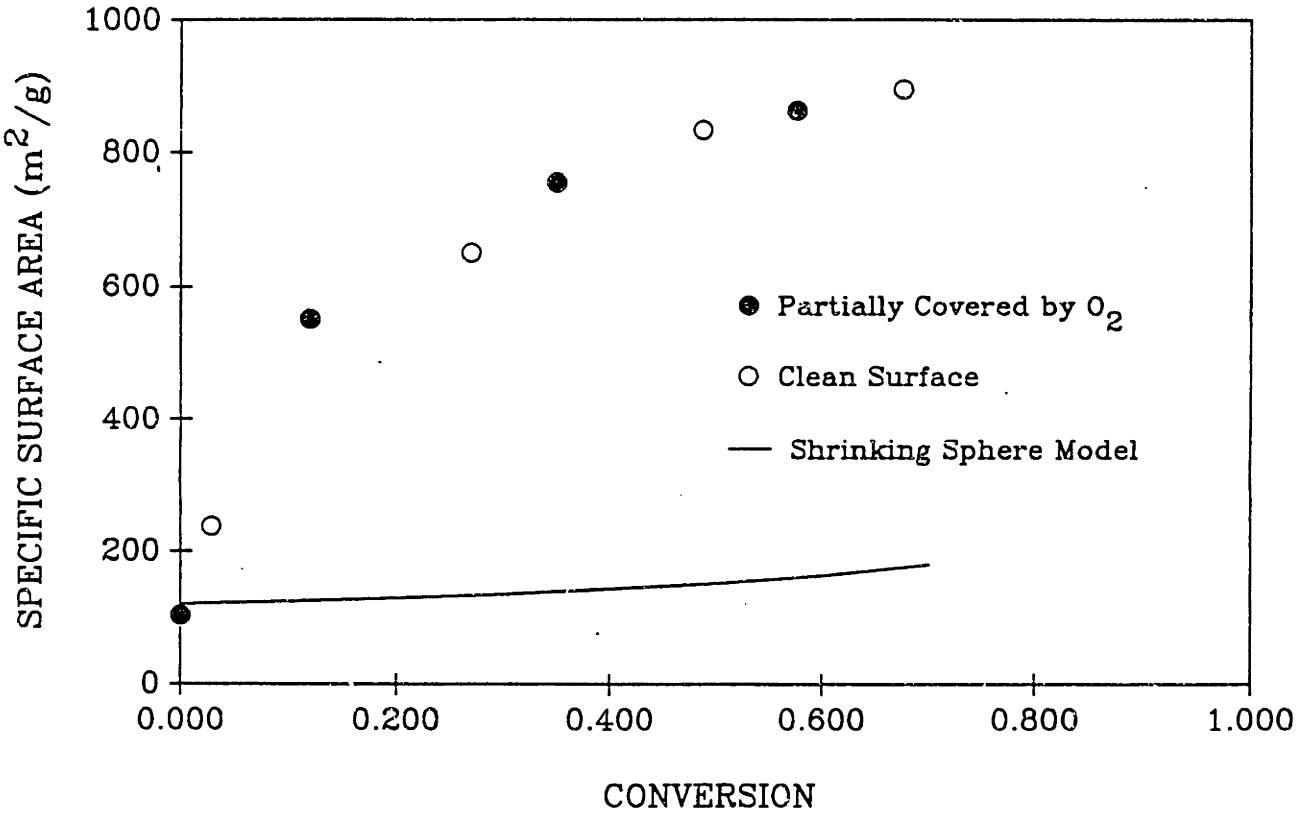

Fig. 3.2 Specific surface area of ST1 at different conversions.

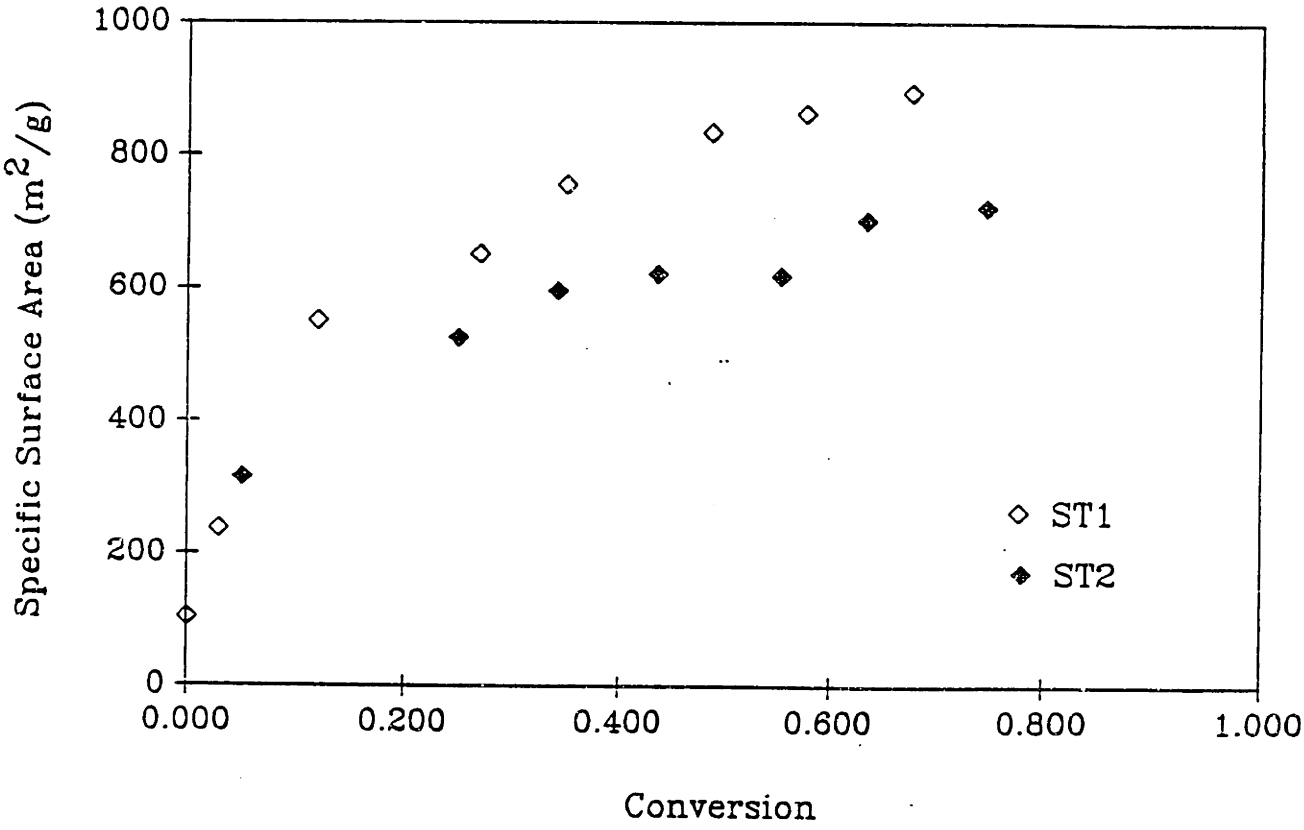

Fig. 3.3 Specific surface area of ST1 and ST2 at different conversions.

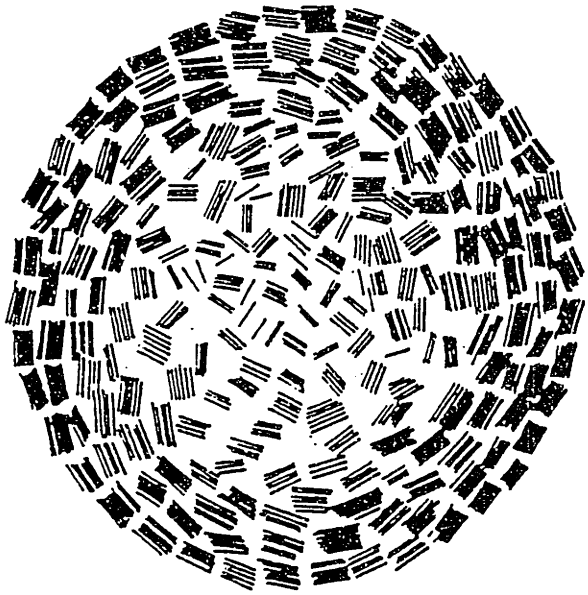

Fig. 3.4 A schematic of concentric crystallite model of carbon black microstructure [67].

initially. Oxidation will react away a thin blocking shell to make these micropores accessible and measurable. Furthermore, from the surface area of 121 m^2/g and the primary particle diameter of ~43 nm, the density of the fresh ST1 was estimated as 1.2 ± 0.4 g/cm^3, which is less than the density of nonporous carbon, a value about 2.0 g/cm^3. The low density of the fresh ST1 indicates the existence of porous structure inside the soot particle. A possible micro-structure of such kind, called the concentric crystallite model of carbon black micro-structure, was proposed by Heckman and Harling [67], and is illustrated in Fig. 3.4.

The continuous growth of the surface area of ST1 beyond 20% conversion implies that the oxidation of ST1 occurs uniformly on the entire carbon surface available, and as a result, enlarges the micropores inside the soot particle.

The behavior that the specific surface area of ST2 approaches an asymptotic value beyond 20% conversion can be explained as the catalytic reaction occurs only on those 'catalyzed active sites' most of which reside on the *external* surface of the carbon. As a result, the micro-structure inside the ST2 particle will not be altered upon oxidation, and the specific surface area of ST2 will not vary too much with the reaction.

3.5 Summary

The following aspects summarize the preceding discussions in this Chapter:

3.51 The present gravimetric method can be applied to accurately measure surface area of a small amount of sample in the TGA system.

3.52 The surface area evolutions of ST1 and ST2 during oxidation exhibit two features:

1) The specific surface areas of both ST1 and ST2 increase rapidly during the first 20% conversion, due to opening the inaccessible surface area inside the soot particle.

2) The specific surface area will either continue to growth or approach an asymptote beyond 20% conversion, depending on the oxidation occurs whether on the entire surface for the ST1 sample, or on those 'catalyzed active sites', which reside on the external surface of the carbon, for the ST2 sample.

3.53 For the modeling purpose, the specific surface area data for ST1 and ST2 are fitted with two analytical expressions: (see Fig. 3.5)

$$S_A=141.2+776.4[1-\exp(-4.407x)] \quad (m^2/g) \quad \text{for ST1}$$

and $$S_A=156.9+555.6[1-\exp(-4.507x)] \quad (m^2/g) \quad \text{for ST2}$$

where x is the conversion defined the same as in Chapter 2.

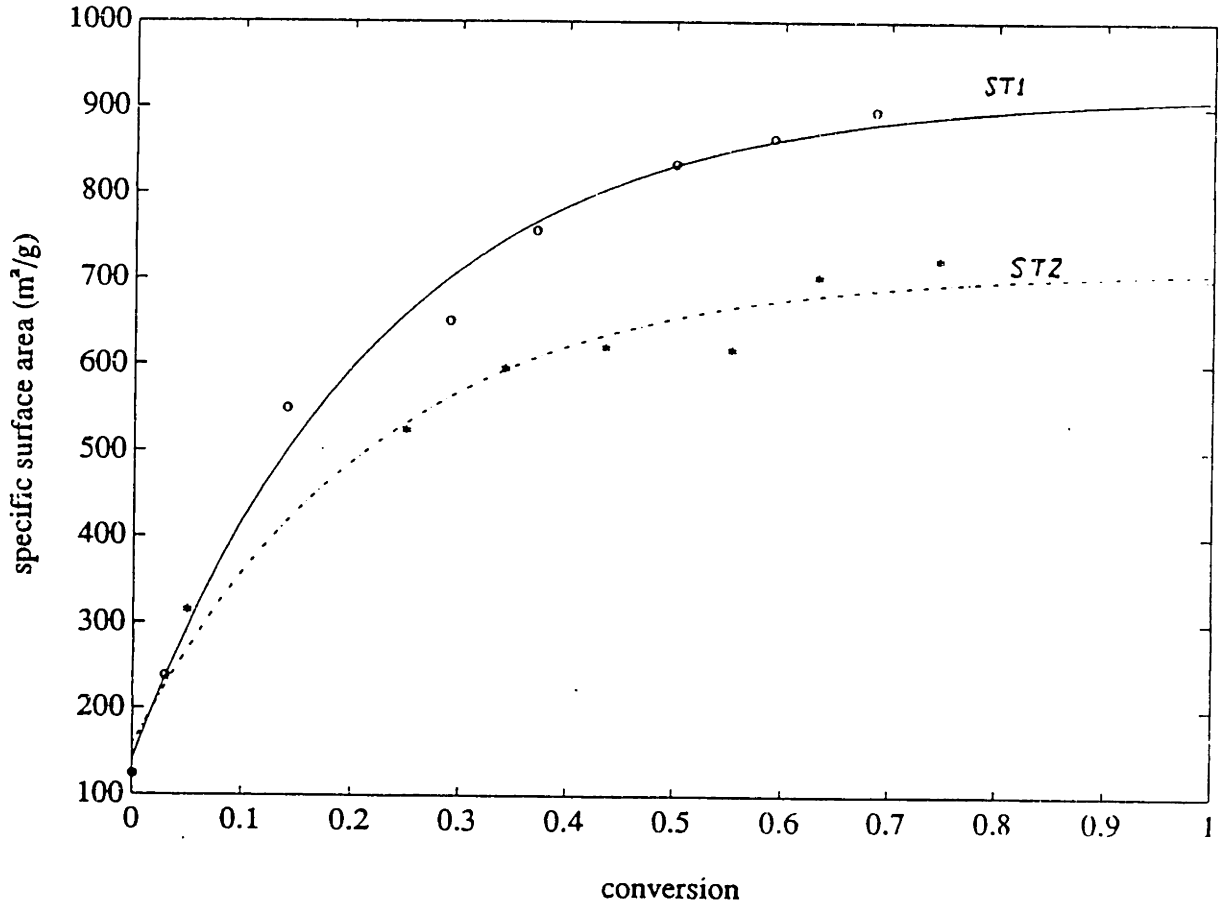

Fig. 3.5 Specific surface area of ST1 and ST2 as functions of conversion.

Chapter 4. Desorption Model

4.1 Introduction

4.11 Background

Carbon oxidation is a complicated process involving many elementary reaction steps. It is desired that these relatively simple elementary steps can be independently studied, and then combined together to provide a better understanding on the whole oxidation process. Desorption of (C-O) complex from the carbon surface is just one of these elementary steps which may be investigated and understood independently from the oxidation process.

Furthermore, the TPD (temperature programing desorption) technique, which is commonly used in the desorption study, has been also widely employed to investigate the nature of (C-O) complex on carbon surface. Applying the TPD technique, Kelemen and Freund [68] examined the thermal stability of surface oxygen complexes on glassy carbon formed by pre-oxidations in O_2 and CO_2 at 973K. Kyotani et al [69] conducted a series of TPD studies on H_2O-gasified and O_2-chemisorbed coal chars. By comparing the intensity and pattern of the TPD spectra, Kapteijn et al [70] investigated catalytic effects of alkaline earth elements on the CO_2 gasification of activated carbon, and Herman and Huttinger [71] studied the effects of heat treatment temperature on H_2O-gasified PVC cokes.

4.12 Problem Statement and Objective

The desorption information obtained from the TPD experiment is strongly coupled with the temperature history in the TPD process. The different temperature programs applied in TPD may result in different

intensities as well as patterns of the TPD spectra, even though the surface condition of the carbon is same. (Detailed experimental evidence can be found in Section 4.31 of this Chapter.) This coupling effect makes the comparison of TPD spectra obtained using different temperature programs very difficult.

The objective of the desorption modeling is to deconvolute the heating-method-dependence from the TPD spectrum, and to obtain intrinsic information about energetics of the surface oxygen complex.

A desorption model has been developed in this Chapter, using an approximation technique, to determine the energetics of surface complexes, e.g. the activation energy distribution of the (C-O) complex. Limited applications of a similar approximation technique may be found in those pyrolytic reaction models reviewed by Howard [72]. The work by Pitt [73] was applied only to isothermal coal pyrolysis to obtain the activation energy distribution, while the approximation method developed by Suuberg [74] to deal with the evolution of volatile products in non-isothermal coal pyrolysis assumed a Gaussian activation energy distribution. The major advantage of the present model is its ability to determine the activation energy distribution directly from the experimental data for both isothermal and non-isothermal processes.

4.2 Desorption Model

4.21 Description of a TPD Process.

During a typical TPD process, the temperature of a carbon sample is programmed to continuously increase to an ultimate value T_f, at which it is held for a certain period of time. As the sample heats up in an inert atmosphere, the (C-O) complexes, which are formed by a pre-

chemisorption of O_2 on the carbon surface, are thermally decomposed into either CO or CO_2. In accordance with the observation from our experiments, CO is the primary desorption product in TPD. The amount of CO produced is typically 10 times greater than CO_2 (see Table 4.1). And the emphasis in this study will be therefore on the CO generation during TPD.

Table 4.1

Total Amount of CO & CO_2 Desorbed in TPD

Heating Method (see Section 4.31)	Products Desorbed (mol/cm^2) x10^{10} CO	CO_2	$\frac{CO}{CO_2}$
Slow Heating	6.75	0.36	19
Fast Heating	7.39	0.43	17
Two-step Heating	5.36	0.34	16

Due to the complex surface structure of typical carbon material, the (C-O) complexes formed on its surface will possess a broad range of binding energies. Accordingly, the thermal desorption of these (C-O) complexes will exhibit a marked difference in a activation energy. Fig. 4.1 illustrates several possible (C-O) complexes on carbon surface [75], and Table 4.2 lists several activation energies for breaking C-C bond at different local structures [76] [77]. To describe such an activation energy range, the energy distribution function, f(E), is introduced, where $f(E)\Delta E$ denotes the fraction of total (C-O) complex population with activation

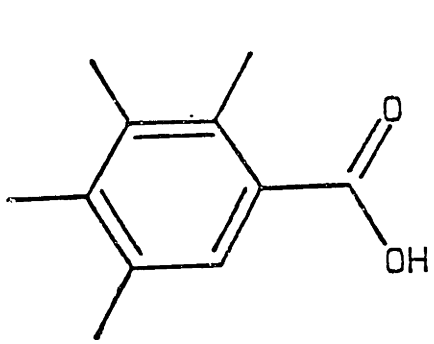

carboxyl

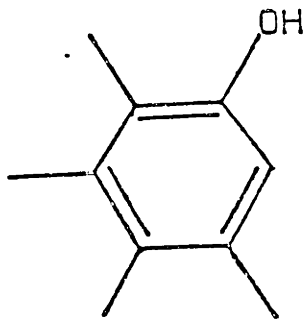

phenolic hydroxyl

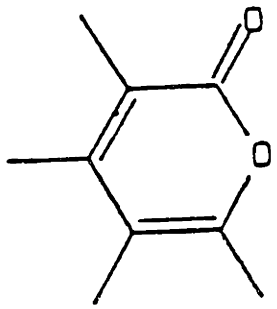

normal lactone

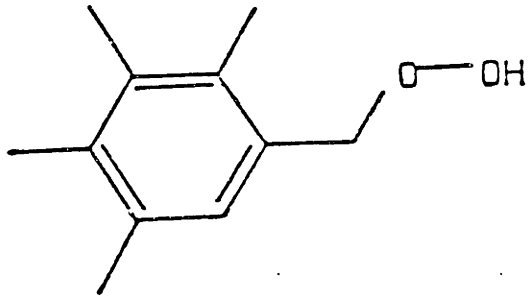

hydroperoxide

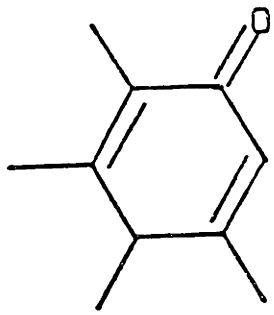

quinonic carbonyl

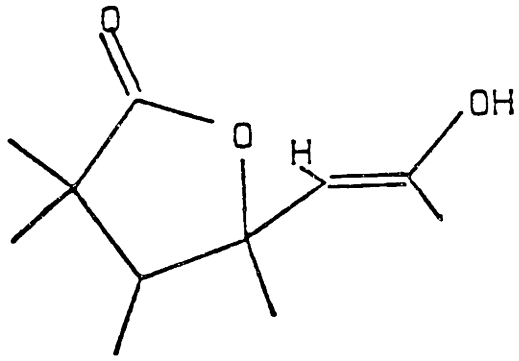

fluorescein lactone

Fig. 4.1 Postulated functional groups of the (C-O) complex.

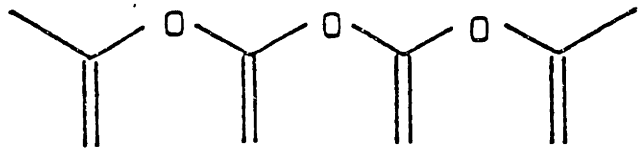

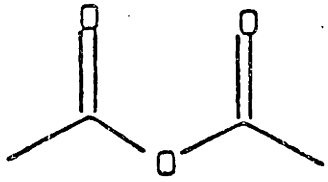

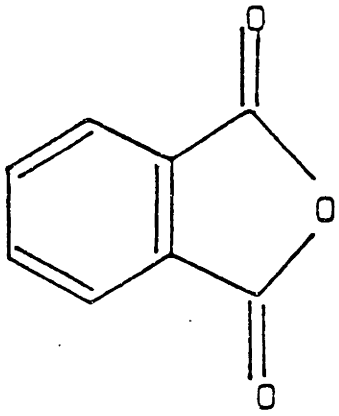

carboxylic acid
anhydride

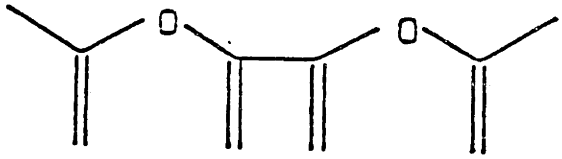

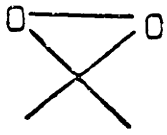

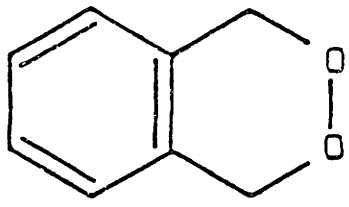

cyclic peroxide

Fig. 4.1 Postulated functional groups of the (C-O) complex.

Table 4.2

Representative Bridge Dissociation Reactions and Energies [77]

	Kcal/mol
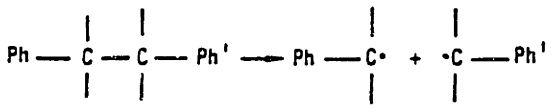	56
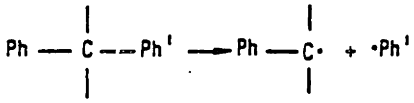	81
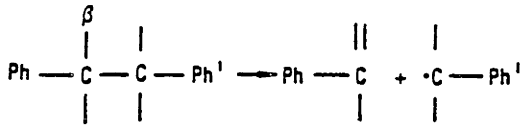	7
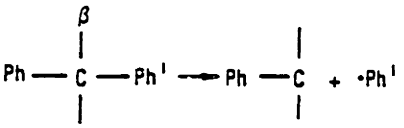	58
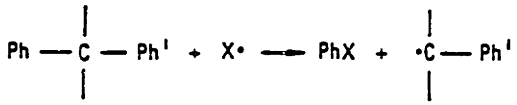	2-9
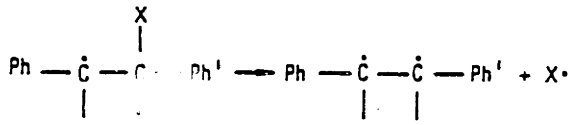	43-50
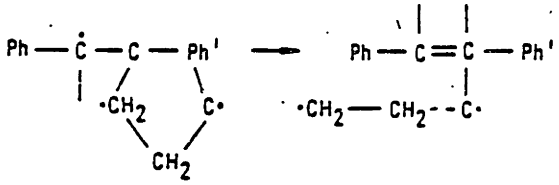	43

β denotes $\dot{C}H_2$ or > $\dot{C}H$ of hydro-aromatic structure.
Ph denotes an aromatic nucleus.

energy of desorption between E and E+ΔE, and integration of f(E) over all energies is one, i.e.,

$$\int_{-\infty}^{\infty} f(E)dE = 1 \qquad (4.1)$$

Having introduced the idea of distributed activation energies, we can divide the entire thermal decomposition of (C-O) complexes on carbon surface into a number of independent parallel reactions, each of which has its own activation energy and irreversibly produces the same product, CO. For each activation energy the rate is assumed to be proportional to the amount of uncreated material remaining, i.e.,

$$(C\text{-}O) \xrightarrow{k_E} CO$$

$$\frac{d[CO]_E}{dt} = k_E[C\text{-}O]_{E,t}\Delta E \qquad (4.2)$$

where k_E — rate constant (1/min)

$[C\text{-}O]_{E,t}\Delta E$ — number of (C-O) complexes remaining on the carbon surface with activation energy between E and E+ΔE at time t (mol).

$[CO]_E$ — amount of CO desorbed from those (C-O) complexes with activation energy between E and E+ΔE during time period 0 to t (mol).

4.22 Model Development (Desorption)

The principles which govern the CO evolution during TPD are the conservation of mass and the rate equation of CO generation. The former

states that the total CO produced equals the difference between the total initial (C-O) complexes and the (C-O) complexes remaining, i.e.,

$$[CO] = [C\text{-}O]_{tot} - \int_{-\infty}^{\infty} [C\text{-}O]_{E,t} dE \tag{4.3}$$

and the latter results from the integration of Eq. (4.2) over the entire range of activation energy,

$$\frac{d[CO]}{dt} = \int_{-\infty}^{\infty} k_E [C\text{-}O]_{E,t} dE \tag{4.4}$$

The initial conditions are:

at $t = 0$, $[C\text{-}O]_{E,0} = [C\text{-}O]_{tot} f(E)$ and $[CO] = 0$. Taking derivative with respect to t on the both sides of Eq. (4.3) generates

$$\frac{d[CO]}{dt} = - \int_{-\infty}^{\infty} \frac{\partial [C\text{-}O]_{E,t}}{\partial t} dE \tag{4.5}$$

And combining Eq. (4.4) and (4.5) gives

$$\int_{-\infty}^{\infty} \{ \frac{\partial [C\text{-}O]_{E,t}}{\partial t} + k_E [C\text{-}O]_{E,t} \} dE = 0$$

or

$$\frac{\partial [C\text{-}O]_{E,t}}{\partial t} + k_E [C\text{-}O]_{E,t} = 0 , \qquad \text{for all E} \tag{4.6}$$

The expression for $[C\text{-}O]_{E,t}$, obtained by solving Eq. (4.6) with initial conditions, is

$$[C\text{-}O]_{E,t} = [C\text{-}O]_{tot} f(E) \exp(- \int_{0}^{t} k_E dt) \tag{4.7}$$

We will assume that k_E is of the Arrhenius form, that is,

$$k_E = k_o \exp(- \frac{E}{RT})$$

and let

$$g(E,t) \equiv \exp(-\int_0^t k_E dt) = \exp[-\int_0^t k_o \exp(-\frac{E}{RT(\xi)})d\xi]$$

where x is a dummy variable corresponding to time in the integral, Since k_o is usually very large (larger than 10^{10}/min), the value of g(E,t) will increase from 0 to 1 over a small energy interval, ΔE (See Fig. 4.2). This steep slope of g(E,t) within ΔE suggests approximating g(E,t) as a step function with its jump point at a so-called critical activation energy E^*, where E^* satisfies $g(E^*, t) = e^{-1} = 0.368$ (see also Fig. 4.2). The criteria for this step function approximation will be discussed later.

Applying the step function approximation to g(E,t), we can rewrite Eq. (4.3) as

$$[CO] = [C\text{-}O]_{tot} - \int_{-\infty}^{\infty} [C\text{-}O]_{tot} f(E) g(E,t) dE$$

$$\approx [C\text{-}O]_{tot} (1 - \int_{E^*}^{\infty} f(E) dE) \qquad (4.8)$$

where the use of Eq. (4.7) was made. The physical significance of Eq. (4.6) is that those (C-O) complexes with the activation energy below E^* are very active in TPD and rapidly desorbed to CO, while those complexes with the activation energy above E^* are inactive and will remain on the carbon surface.

Differentiation of Eq. (4.8) with respect to t gives

$$\frac{d[CO]}{dt} = [C\text{-}O]_{tot} \frac{dE^*}{dt} f(E) \qquad (4.9)$$

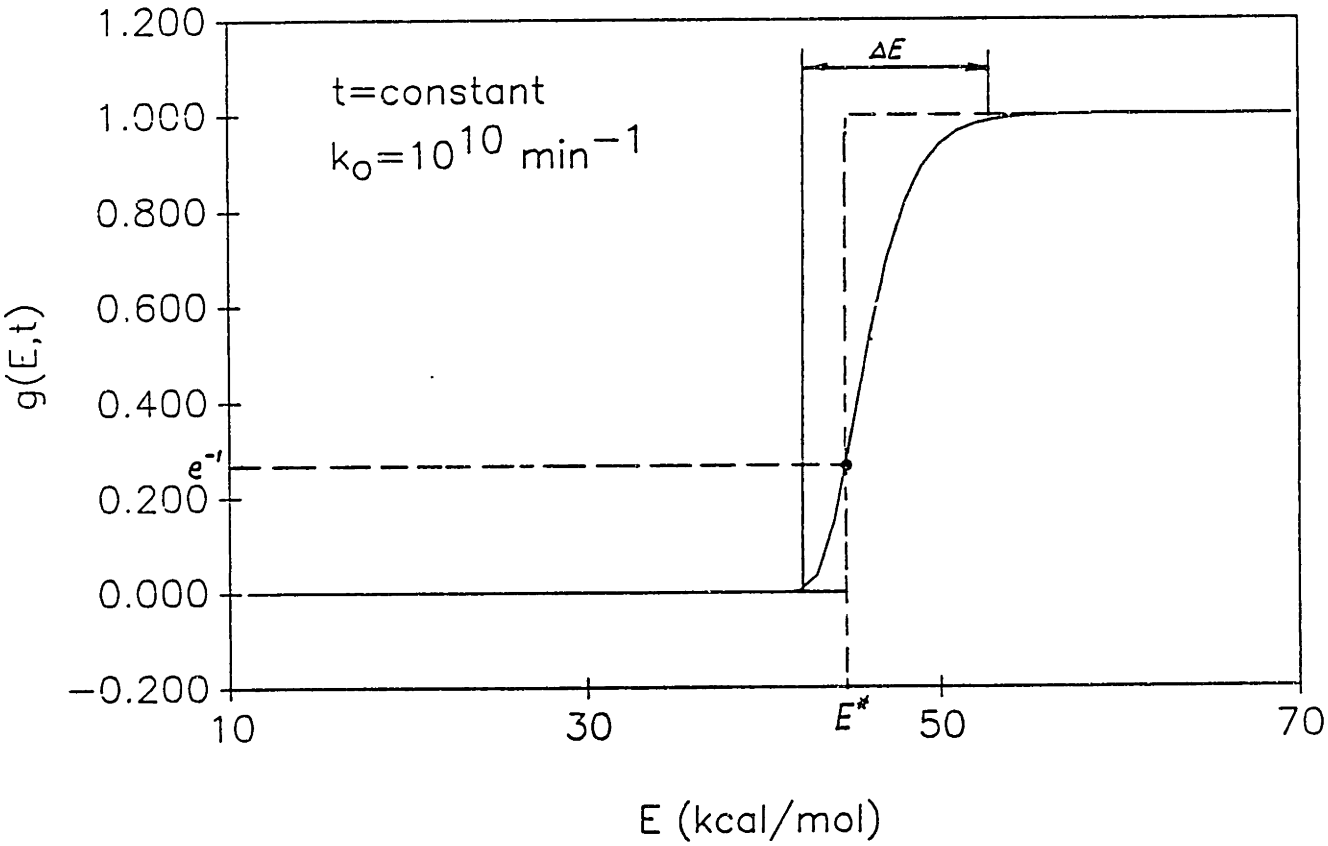

Fig. 4.2 Plot of g(E,t) versus E for constant t.

The quantities of $\frac{d[CO]}{dt}$ and $[C\text{-}O]_{tot}$ are measurable during the TPD experiment. The distribution function is hence determinable from Eq.(4.7), when E^* and $\frac{dE^*}{dt}$ can be calculated from the experimental data, as described below.

4.23. Calculation of Critical Activation Energy E*

The temperature evolution in the TPD must be known for the calculation of E^*. An imposed profile is considered. This profile ramps the temperature from an initial value T_i to a final value T_f, which is then maintain for a certain period of time, i.e.

$$T = \begin{cases} T(t) & 0 \le t \le t_f \\ T_f = \text{Const.} & t > t_f \end{cases}$$

$$\frac{dT}{dt} = \begin{cases} T'(t) > 0 & 0 \le t \le t_f \\ 0 & t > t_f \end{cases}$$

Other more complicated heating programs can be treated in a similar manner.

We recall that E^* is defined such that

$$g(E^*,t) = \exp\left[-\int_0^t k_o \exp\left(-\frac{E^*}{RT(\xi)}\right)d\xi\right] = e^{-1}$$

or

$$\int_0^t k_o \exp\left(-\frac{E^*}{RT_i}\frac{T_i}{T(\xi)}\right)d\xi = \frac{1}{k_o} \ll 1 \qquad (4.10)$$

In order for the integral in Eq. (4.10) to be small, we must have $\frac{E^*}{RT_i} \gg 1$ since $\frac{T_i}{T(\xi)} \sim O(1)$. Using Laplace's method [78], the limiting behavior of the integral for large $\frac{E^*}{RT_i}$ is (see Appendix C):

$$\int_0^t \exp\left(-\frac{E^*}{RT_i}\frac{T_i}{T(\xi)}\right)d\xi \approx \begin{cases} \dfrac{T(t)}{yT'(t)}\,e^{-y} & 0 \le t \le t_f \\ \left[\dfrac{T_f}{T'_f y_f} + (t - t_f)\right]e^{-y} & t > t_f \end{cases} \qquad (4.11)$$

where notations $T'_f \equiv T'(t_f)$, $y \equiv \frac{E^*}{RT(t)}$ and $y_f \equiv \frac{E^*}{RT_f}$ are used. Equating Eq's (4.10) & (4.11) will give the governing equations for y or E^*:

$$k_o \frac{T(t)}{T'(t)} = y\, e^y \qquad \text{for } 0 \le t \le t_f \qquad (4.12a)$$

$$k_o\left[\frac{T_f}{T'_f} + (t - t_f)y_f\right] = y_f\, e^{y_f} \qquad \text{for } t > t_f \qquad (4.12b)$$

Theoretically, Eq. (4.12a,b) does not have a closed form solution for y. Either numerical or graphical (see Fig. 4.3) methods should therefore be adopted to solve for y, and then E^*. Nevertheless, an asymptotic solution to Eq. (4.12a) could be found, if $a \equiv \ln\left(k_o \frac{T(t)}{T'(t)}\right)$ is sufficiently large (see Appendix D):

$$\frac{E^*}{RT(t)} = a - \ln(a) + \frac{\ln(a)}{a} + \frac{\ln(a)}{2a^2}\left[\ln(a) - 2\right] \qquad \text{for } 0 \le t \le t_f \quad (4.13)$$

The error committed from Eq. (4.13) is in the order of $\left(\frac{\ln(a)}{a}\right)^3$. Table 4.3 gives the comparison between the exact y, which is solved from Eq. (4.12a) by a numerical method, and the approximated y from Eq. (4.13). It is quite clear that Eq. (4.13) is an excellent approximation to Eq. (4.12a).

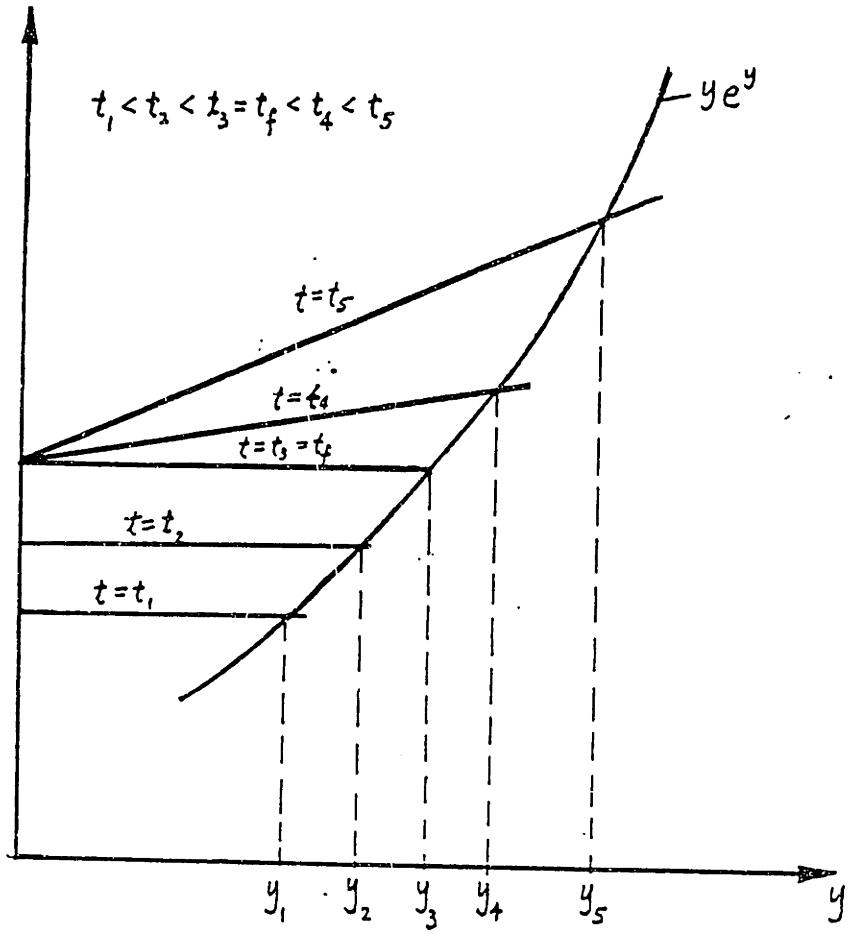

Fig. 4.3 Schema of the graphic method for solving Eq. (4.12).

Table 4.3

A Comparison of the Exact and Approximate Solutions to Eq. (4.12a)

$k_o\frac{T}{T'}$	$a \equiv \ln(k_o\frac{T}{T'})$	y Value		Rel. Error
		Approx.	Exact	
10^{10}	23.03	20.02882	20.02868	-6.57×10^{-6}
10^{11}	25.33	22.22721	22.22712	-4.03×10^{-6}
10^{12}	27.63	24.43507	24.43501	-2.50×10^{-6}
10^{13}	29.93	26.65083	26.65079	-1.50×10^{-6}
10^{14}	32.24	28.87330	28.87327	-0.99×10^{-6}
10^{15}	34.54	31.10154	31.10152	-0.61×10^{-6}

4.24 Calculation of $\frac{dE^*}{dt}$

We rewrite Eq. (4.10) as

$$G(E^*,t) \equiv \int_0^t k_o \exp\left(-\frac{E^*}{RT_i}\frac{T_i}{T(\xi)}\right)d\xi = \frac{1}{k_o} \qquad (4.10)$$

We also know that

$$\frac{\partial G}{\partial E^*} \approx -\frac{1}{RT(t)}G(E^*,t) = -\frac{1}{RT(t)k_o}$$

from the limiting case of $\frac{E^*}{RT_i} \gg 1$ (see Eq.(C2) in Appendix C), and

$$\frac{\partial G}{\partial t} = \exp\left(-\frac{E^*}{RT(t)}\right)$$

Thus,

$$\frac{dE^*}{dt} = -\frac{\frac{\partial G}{\partial t}}{\frac{\partial G}{\partial E^*}} \approx k_o RT(t)\exp\left(-\frac{E^*}{RT(t)}\right)$$

$$\approx \begin{cases} E^* \dfrac{T'(t)}{T(t)} & 0 \le t \le t_f \\ \dfrac{E^*}{\dfrac{T_f}{T_f'} + (t-t_f)\dfrac{E^*}{RT_f}} & t > t_f \end{cases} \tag{4.14}$$

Substituting the values of E^* and $\frac{dE^*}{dt}$ into Eq.(4.9), we are now able to calculate the energy distribution function, according to

$$f(E^*) = \frac{1}{[C\text{-}O]_{tot}} \frac{\frac{dE^*}{dt}}{\frac{d[CO]}{dt}} \tag{4.15}$$

4.25 Criterion for the Step Function Approximation

Recalling that the simplification of g(E,t) as a step function will introduce an error in the integration of Eq. (4.8), we are going to develop a criterion in this section to restrict such an error to a tolerable level. We rewrite the integration part of Eq. (4.8) as

$$\int_{-\infty}^{\infty} f(E)g(E,t)dE \approx \int_{E^*}^{\infty} f(E)dE \tag{4.16}$$

and plot f(E) and g(E,t) in Fig. 4.4.

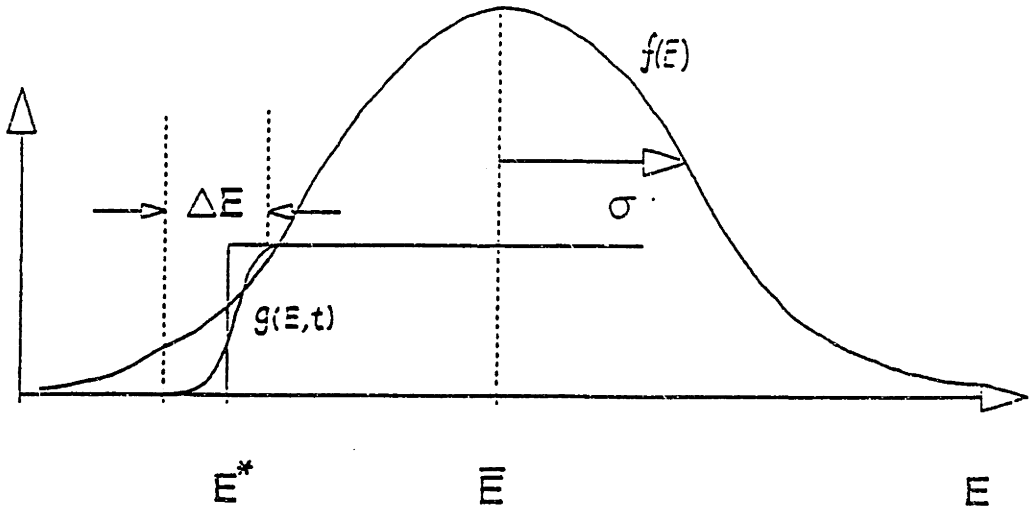

Fig. 4.4 Plot of g(E,t) and f(E) for versus E.

It can be seen from Fig. 4.4 that the error committed by the step function approximation will be small, if the width of distribution function f(E) is larger than the ΔE within which g(E,t) varies from 0 to 1. The width of f(E) is characterized by its standard deviation σ defined by

$$\sigma^2 \equiv \int_{-\infty}^{\infty} (E - \bar{E})^2 f(E) dE \tag{4.17}$$

where $\bar{E}$ is the mean of f(E). ΔE, on the other hand, could be estimated by the interval over which the tangential line of $g(E^*,t)$ increase from 0 to 1, i.e. ,

$$(1 - 0) \approx \frac{\partial g}{\partial E}\Big|_{E=E^*} \Delta E \tag{4.18}$$

For the limiting case of $\frac{E^*}{RT_i} \gg 1$ (see Eq. (C3) in Appendix C),

$$\frac{\partial g}{\partial E}\Big|_{E=E^*} \approx - \frac{1}{RTk_o} (-k_o e^{-1}) = \frac{1}{2.72RT}$$

Thus the criterion for the step function approximation will be

$$2\sigma > \Delta E$$

or

$$\frac{\sigma}{1.36RT} > 1 \tag{4.19}$$

Suuberg [74] reached the similar criterion, after he employed the step function approximation to a Gaussian distributed energy model for pyrolysis. He concluded in his paper [74] that the maximum error would be about 5% when $\frac{\sigma}{\sqrt{2}RT} = 1$, and about 15% when $\frac{\sigma}{\sqrt{2}RT} = 0.5$. His result implies that the step function approximation used in our desorption model will result in only a small error if the criterion of $\frac{\sigma}{1.36RT} > 1$ is satisfied.

4.3 Model Test

The testing procedure consists of three stages:

1) conducting TPD experiment and measuring T(t), $\frac{d[CO]}{dt}$ and the total amount of CO generated in TPD; then calculating E^*, $\frac{dE^*}{dt}$ and $f(E^*)$ according to Eq.'s (4.12a,b), (4.14) and (4.15).

2) calculating the standard deviation of f(E), and checking if the criterion, or Eq. (4.19), is satisfied.

3) testing the sensitivity of f(E) to the temperature history in TPD. If the computed f(E) from Eq. (4.15) is the 'true' energy distribution function, it should be an intrinsic property of the carbon material and insensitive to the temperature history used in TPD.

4.31 Experiment

The tube-furnace-MS arrangement described in Chapter 2 was employed for all TPD experiments, and ST1 material was used for the purpose of model test. The TPD runs started with approximately the same initial surface condition on ST1 sample, which was achieved by chemisorbing oxygen at 818K in 21% O_2 & 79% Ar gas mixture for 3 minutes and cooling to 598K in the same environment prior to the TPD run. The temperature in the TPD runs started at T_i = 598K and ended up at T_f = 1173K. In order to test the sensitivity of f(E) to temperature history, three temperature programs, shown in Fig. 4.5a & 4.5b, were performed in the TPD experiments: (1) slow heating, which takes about 35 minuted to ramp temperature from 598K to 1173K; (2) fast heating, which is about two times faster than the slow heating to reach 1173K; (3) two-step heating,

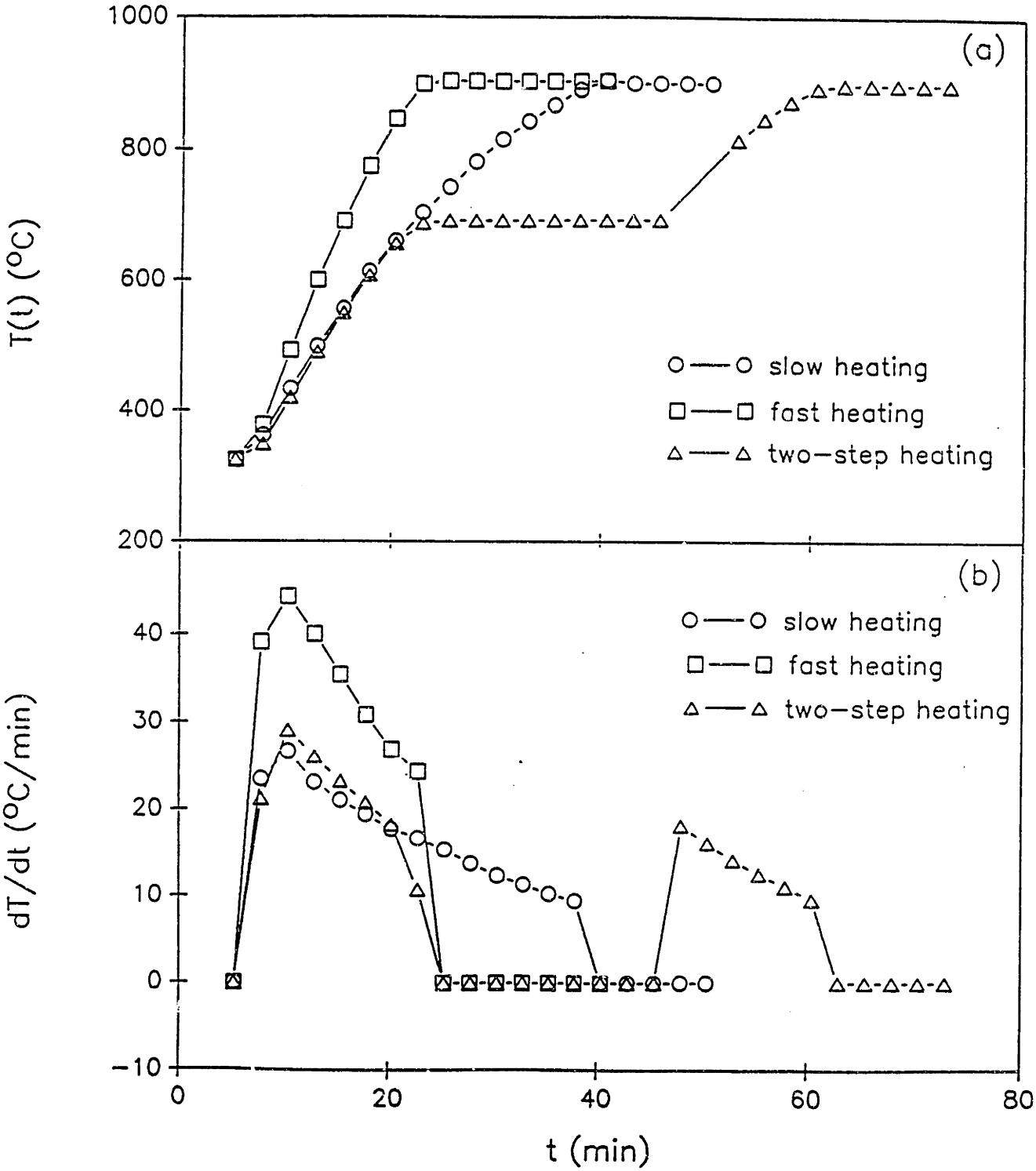

Fig. 4.5 Three temperature programs used in TPD experiment (a) T vs t (b) dT/dt vs t

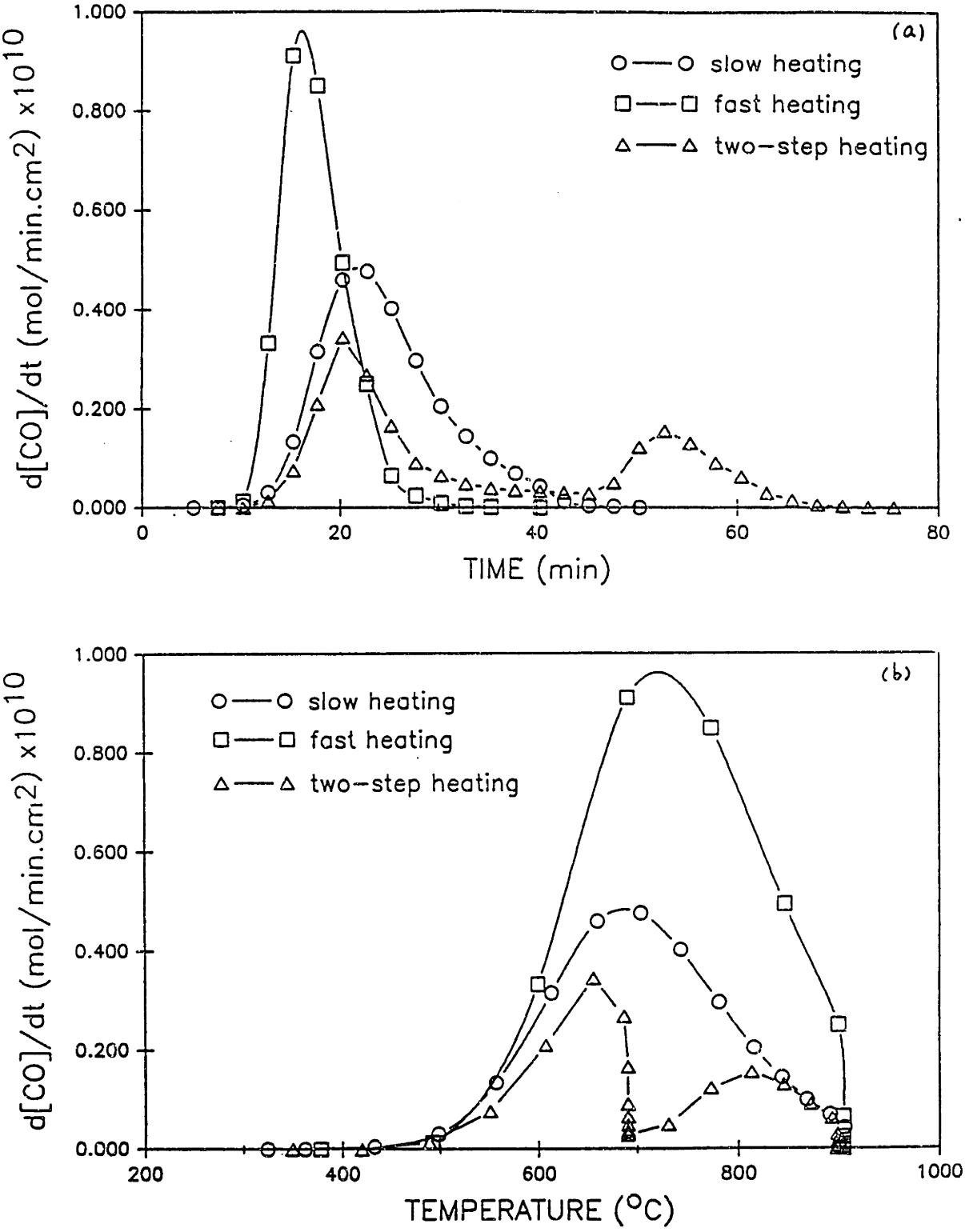

Fig. 4.6 CO generation in TPD: (a) d[CO]/dt vs t (b) d[CO]/dt vs T

which first ramps the temperature to 964K, maintains at this value for about 23 minutes, then increases the temperature again to 1173K. The final holding time in all three programs stopped when the CO signal decreased to the detection limit.

The results from the TPD experiments are tabulated and plotted in Table 4.1, and Fig. 4.6a & 4.6b. Fig. 4.6a gives the time dependence on the CO generation rate in the TPD processes. The area under each curve in Fig.4.6a corresponds to the CO generation , or $[C\text{-}O]_{tot}$, during the TPD run, and its value is tabulated in the second column of Table 4.1. The $[C\text{-}O]_{tot}$ in the slow and fast heating runs are approximately the same within the experiment error, and the lower value of $[C\text{-}O]_{tot}$ in the two-step heating case may be attributed to the relatively large error introduced in measuring the weak CO signal during the first holding period. Fig. 4.6b gives the TPD spectra corresponding to those three temperature programs used in our TPD experiments. The effect of heating history on the TPD spectrum is clear. As the heating rate increases, the intensity of the spectrum goes up, and the peak of the spectrum moves towards the higher temperature. Moreover, a two-peak spectrum will appear when a two-step heating is applied.

4.32 Mono-energy Distribution

The simplest case for the thermal decomposition of (C-O) complex is that all (C-O) complexes are desorbed with almost the same activation energy, E_m. In terms of energy distribution function,

$$f(E) \approx \delta(E - E_m) \tag{4.20}$$

Hence, the rate equation can be written as

$$\frac{d[CO]}{dt} = k_o \exp(-\frac{E_m}{RT})[C\text{-}O]_t \qquad (4.21)$$

where $[C\text{-}O]_t=[C\text{-}O]_{tot}-[CO]$ is the total (C-O) complexes remaining on the carbon surface at time t. Eq. (4.21) can be also derived by combining Eq's (4.3), (4.4), (4.7) and (4.20).

According to Eq. (4.21), the rate of CO generation in TPD should be proportional to $[C\text{-}O]_t$, if temperature was kept constant. This was obviously not the case in the two-step heating TPD experiment, where $\frac{d[CO]}{dt}$ signal were dropped to nearly zero while $[C\text{-}O]_t$ was still about one third of $[C\text{-}O]_{tot}$ during the holding period at 964K (see Fig. 4.6a,b).

Furthermore, Eq. (4.21) can be rearranged as

$$\log(\frac{\frac{d[CO]}{dt}}{[C\text{-}O]_t}) = \log(k_o) - \log(e)\frac{E_m}{R}\frac{1}{T} \qquad (4.22)$$

The plot of the left hand side of Eq. (4.22) against 1/T would form a straight line, if Eq. (4.21) correctly described the rate of CO generation in TPD. However, no straight line was found when the TPD data were plotted in this manner (see Fig. 4.7).

The aforementioned discussions disprove the validity of Eq. (4.21), indicating that the thermal desorption of (C-O) complex on carbon surface possesses widely different activation activation energies.

4.33 Construction of f(E) by the Step Function Approximation

In light of the preceding discussion in Section 4.32, an activation energy distribution, f(E), should be considered in order to properly describe the CO generation in TPD process. Based on the information from the TPD experiments, the f(E) corresponding to each TPD run can be constructed point by point according to Eq.'s (4.12a,b), (4.14) and (4.15).

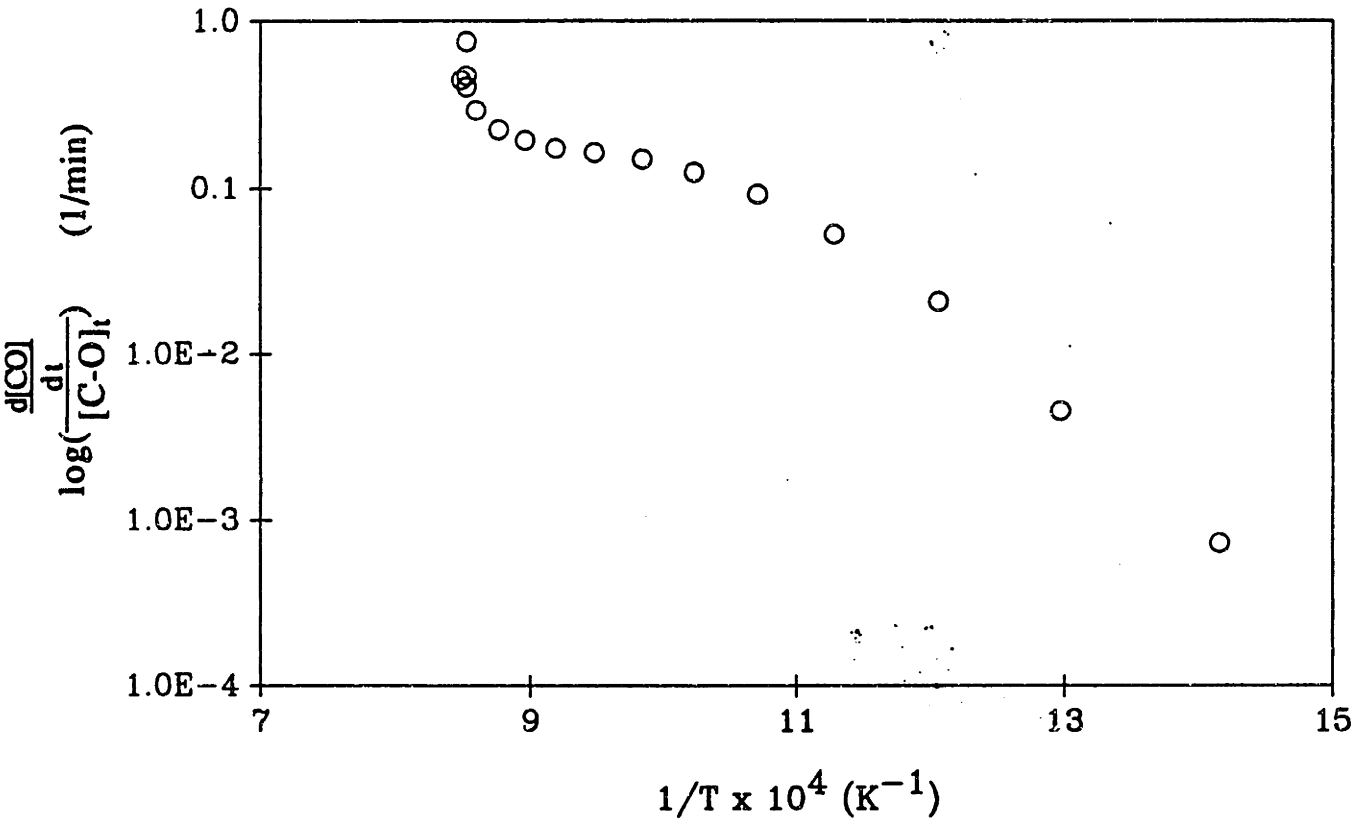

Fig. 4.7 Arrhenius plot for the CO generation in TPD.
(Slow heating program.)

The preexponential k_o is treated as a parameter during the calculation, and three values of 10^{10}, 10^{12} and $6x10^{14}$ (1/min) were considered. The energy distribu ons for different temperature programs and different k_o values are presented in Fig. 4.8a, 4.8b and 4.8c.

4.34 Verification of f(E)

First of all, the validity of the criterion for the step function approximation was examined. For a more severe test, the case of $k_o=10^{10}$ (1/min), which leads to the narrowest distribution for all k_o values investigated (see Fig. 4.8a,b,c), was considered. In this case, the mean and standard deviation of f(E) were found to be 47.5 kcal/mol and 4.5 kcal/mol, respectively. Taking $T = T_f = 1173K$, we have

$$\frac{\sigma}{1.36RT} = 1.41 > 1$$

Little error would therefore be introduced in the calculation of f(E) by the step function approximation.

Secondly, the sensitivity of computed f(E) to the temperature history in TPD was checked. Fig. 4.8a,b,c show that virtually identical f(E) was obtained for all three temperature programs investigated, regardless of the k_o values. The independence of f(E) to the heating history in TPD provides a crucial test of the present approach.

Finally, by utilizing the computed f(E), the rate of CO generation during a TPD process was calculated according to

$$\frac{d[CO]}{dt} = \int_{-\infty}^{\infty} k_E[C\text{-}O]_{E,t}dE$$

$$= \int_{-\infty}^{\infty}\{k_o[C\text{-}O]_{tot}f(E)\exp(-\frac{E}{RT(t)})\exp[-\int_0^t k_o\exp(-\frac{E}{RT(\xi)})d\xi]\}dE \qquad (4.24)$$

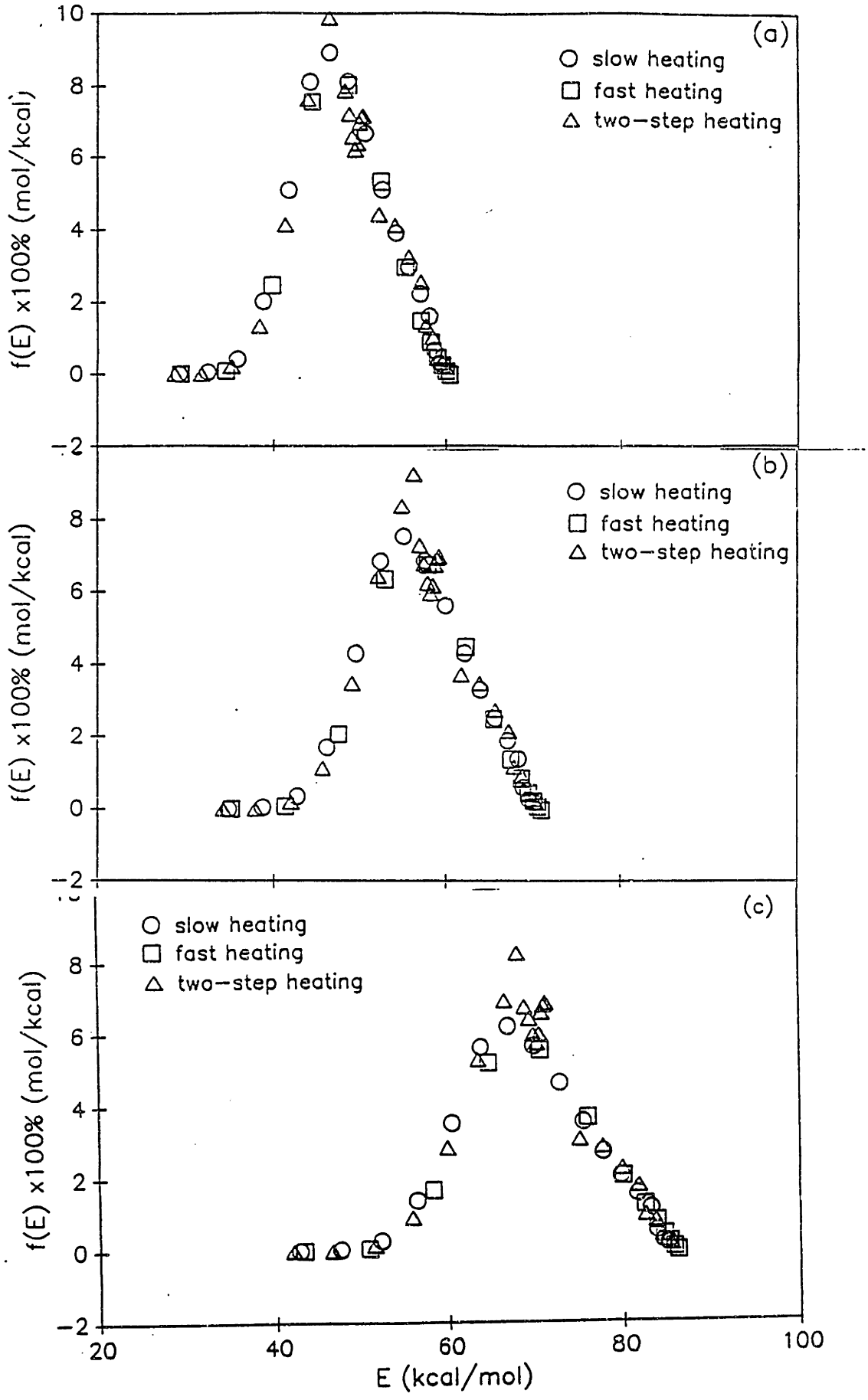

Fig. 4.8 Energy distribution of ST1 determined from TPD data.

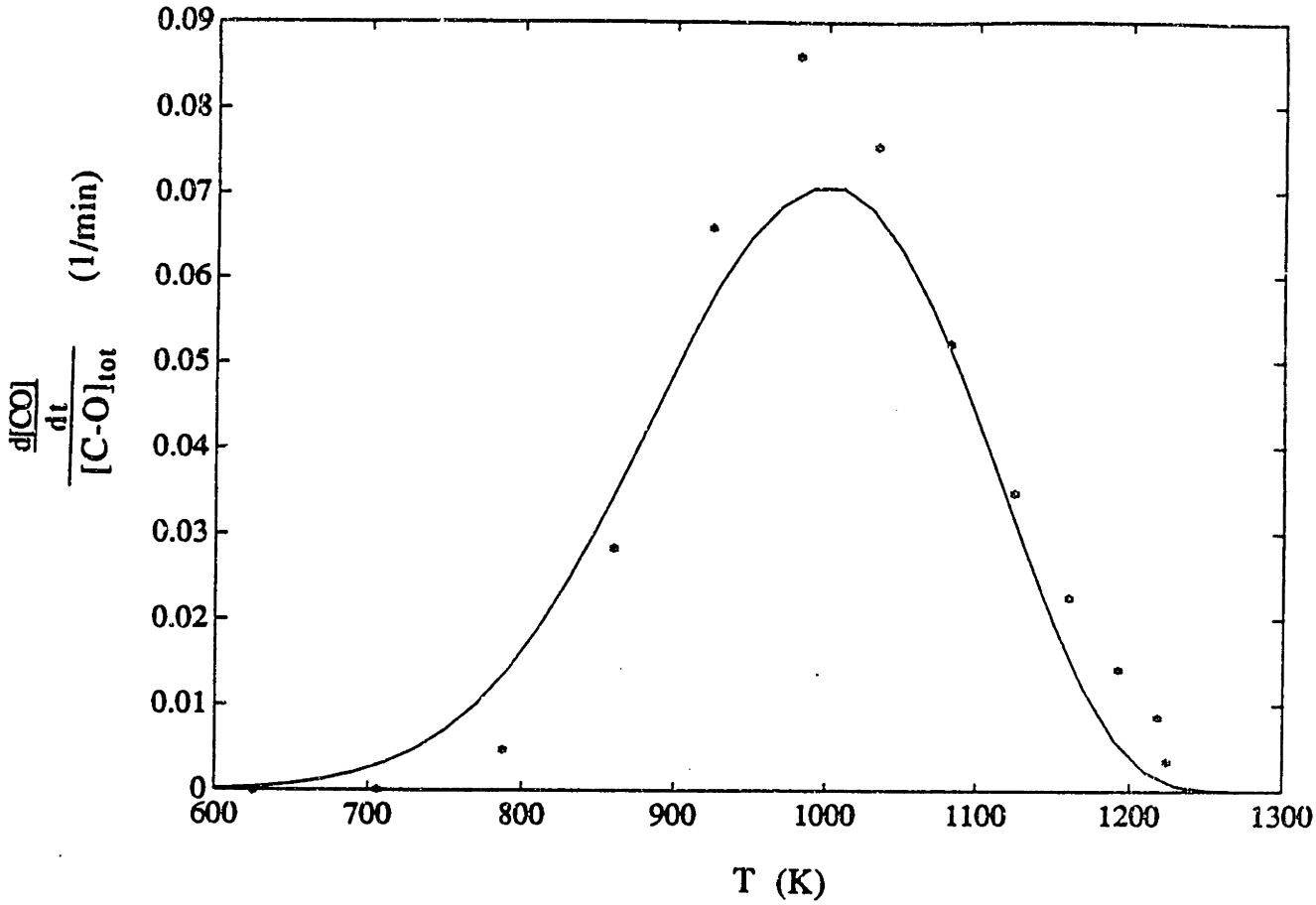

Fig. 4.9 Rate of CO generation in TPD.

Note: Symbol represents experimental data and solid line represents the model prediction for $k_o=6x10^{14}/min$.

and then compared with the experimental measurement. To simplify the calculation, f(E) was approximated to a Gaussian distribution, and the mean and standard deviation of the distribution were found to be 69.7 kcal/mol and 7.81 kcal/mol, respectively, for $k_0=6x10^{14}$/min (see Section 4.46 & Fig.4.10). A constant heating rate of 20 K/min was used in the calculation. Fig. 4.9 shows the comparison between the calculated CO spectrum during a TPD run (solid line) and corresponding experimental data (symbols). The agreement is reasonably good.

4.4 Discussion (Desorption Model)

4.41 Critical Activation Energy E^*

The thermal decomposition of (C-O) surface complex is an activated process. An corresponding intrinsic energy barrier must be overcome for a given (C-O) complex to be desorbed to CO gas. Due to the complicated surface structure of carbon, a variety of (C-O) complexes exists on the carbon surface. These (C-O) complexes can be divided into two categories according to the critical activation energy E^*. The (C-O) complexes with their energy barrier lower than E^* will be quickly desorbed; and those (C-O) complexes with an energy barrier higher than E^* do not have sufficient energy to be decomposed and will remain inactive on the carbon surface.

The value of critical activation energy clearly depends on the desorption conditions, especially the desorption temperature. A rough estimate of E^* from Eq's (4.13) & (4.12b) generates,

$$E^* \sim \begin{cases} RT\ln(k_o\frac{T}{T'}) & 0 \le t \le t_f \\ RT_f\ln(k_o(t-t_f)) & t > t_f \end{cases} \qquad (4.25)$$

Eq. (4.25) does show the strong dependence of E^* on temperature. In addition, it shows the weak dependence of E^* on time in a logarithmic manner, when temperature is kept constant. This can be explained in the sense of statistical mechanics as follows: The change in temperature alters the mean thermal energy of each (C-O) complex, and so affects the capability of the (C-O) complex to overcome the desorption energy barrier. The increase in desorption time, on the other hand, gives each (C-O) complex more attempts at overcoming the desorption barrier, so that the probability of desorption over a higher energy barrier will increase. As a result of above discussion, it is expected that all (C-O) complexes can be desorbed isothermally if the desorption time is long enough.

4.42 Rate of CO Generation in TPD

An approximate relation between the rate of CO generation and the temperature history in TPD can be found by combining Eq's (4.9), (4.14) & (4.25),

$$\frac{d[CO]}{dt} \sim \begin{cases} [C\text{-}O]_{tot}f(E^*)RT'(t)\ln(k_o\frac{T(t)}{T'(t)}) & 0 \le t \le t_f \\ [C\text{-}O]_{tot}f(E^*)\frac{RT_f}{t-t_f} & t > t_f \end{cases} \qquad (4.26)$$

Since the value of $\ln[k_o \frac{T(t)}{T'(t)}]$ does not vary too much during TPD, the rate of CO generation is primarily proportional to the heating rate, T'(t), in the

heating period ($0 \le t \le t_f$), and inversely proportional to the desorption time t in the holding period ($t > t_f$).

4.43 Preexponential k_o

The preexponential k_o is treated as a parameter in the calculation of f(E). It can be seen from Fig. 4.8a,b,c that the increase in k_o will only shift the whole f(E) curve towards the higher energy value, and slightly broaden the distribution of f(E), but preserve the shape of f(E). $k_o = 6 \times 10^{14}$ 1/min will be used from now on for the purpose of computing the energy distribution f(E).

4.44 Shape of f(E)

For the ST1 material, the shape of f(E) was found to be very close to a Gaussian distribution (see Fig. 4.8a,b,c). Therefore, the Gaussian distribution may be utilized to properly approximate the real site energy distribution of the carbon and to simplify the computation.

4.45 Effect of The TPD Final Temperature T_f on f(E)

To examine the effect of the TPD final temperature on f(E), two more TPD runs with T_f = 1223K were conducted using the ST1 sample. A comparison of the energy distributions obtained from the TPD runs with different T_f's are shown in Fig. 4.10. It can be seen from Fig. 4.10 that increasing the final temperature T_f of the TPD heating program from 1173K to 1223K will not significantly affect the f(E) for the ST1 sample.

4.46 f(E) at Different Conversions

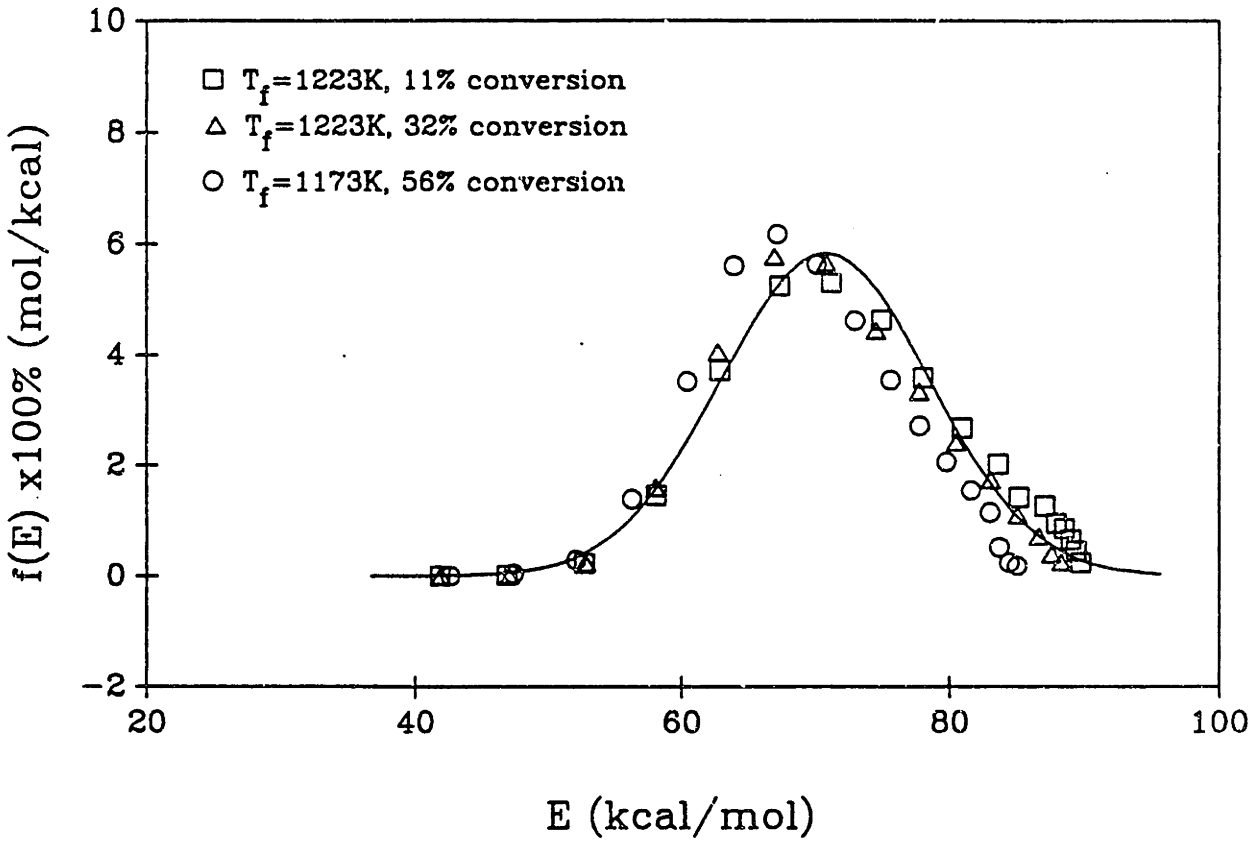

Fig. 4.10 Energy distribution of ST1 obtained from TPD runs with different final temperatures and at different carbon conversions (k_o = $6x10^{14}$/min).

Note: solid line is the best fit of the data points.

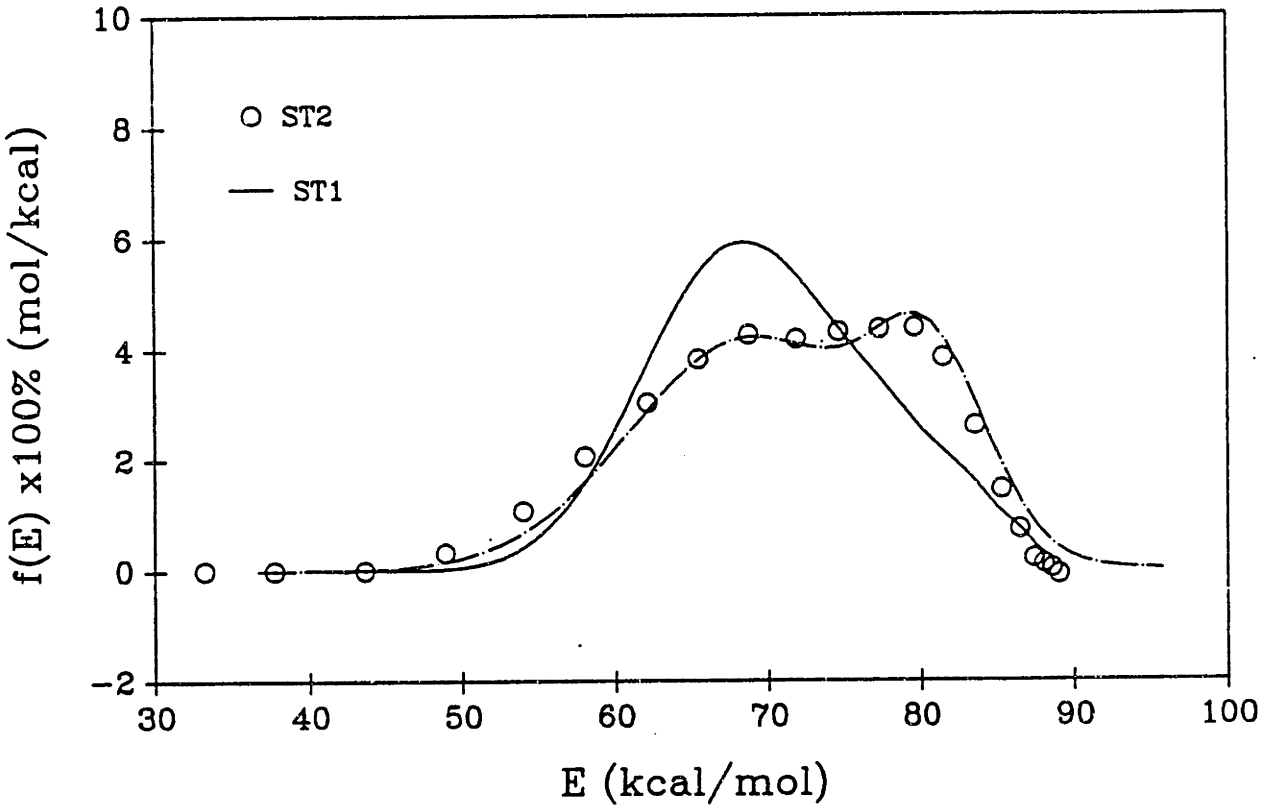

Fig. 4.11 Comparison between the energy distributions of ST1 and ST2 (k_o = 6x10^{14}/min).

Note: dash-dot line is the best fit of ST2 data with a bimodal Gaussian (see Eq. (4.27)).

Fig. 4.10 also shows the energy distributions corresponding to the partially converted ST1. The energy distribution of ST1 was found insensitive to the carbon conversion, suggesting that the active carbon sites can be regenerated during the oxidation.

A Gaussian distribution with $\bar{E}$ = 69.7 kcal/mol and σ = 7.81 kcal/mol may roughly represent those f(E) curves in Fig. 4.10.

4.47 f(E) for The Catalyzed Soot

The similar TPD experiments were carried out using the Ca catalyzed soot, ST2. The energy distribution for ST2 was obtained in the same way as that for ST1, and is presented in Fig. 4.11. (The f(E) of ST1 is also plotted in the same figure for comparison). Two peaks were found in the f(E) of ST2 (see Fig. 4.11). The best fit of the ST2 f(E) with a bimodal Gaussian distribution results in:

$$f(E) \equiv \frac{1}{\sqrt{2\pi}}\{\frac{A}{\sigma_1}\exp[-\frac{(E - \bar{E}_1)^2}{2\sigma_1^2}] + \frac{B}{\sigma_2}\exp[-\frac{(E - \bar{E}_2)^2}{2\sigma_2^2}]\} \qquad (4.27)$$

where A=0.74, B=0.26, $\bar{E}_1$=67.9 kcal/mol, $\bar{E}_2$=79.7 kcal/mol,

σ_1=7.82kcal/mol, σ_2=3.70 kcal/mol.

The first peak in the ST2 f(E) corresponds to the energy distribution of ST1, while the second one is a new feature generated due to the addition of calcium.

4.5 Summary

4.51 Desorption of the (C-O) complexes on the carbon surface can not be explained by a single activation energy process. An site energy

distribution function, f(E), which characterizes the surface structure of the carbon, must be considered in the desorption process.

4.52 The site energy distribution of a carbon material is determinable by incorporating the present desorption model in this Chapter with the TPD experiment.

4.53 The ST1 sample at different conversion levels has approximately the same energy distribution, suggesting that the active carbon sites can be regenerated during the oxidation.

4.54 The energy distribution of the ST2 sample exhibits a second peak, which is created by the Ca addition, compared with the ST1 sample.

4.55 Normal and bimodal Gaussian distributions provide good approximations to the real energy distributions for ST1 and ST2, respectively.

Chapter 5. Oxidation Data and Modeling

In this chapter, data on carbon oxidation rate are presented and a kinetic model for the carbon oxidation is developed and applied to the soot-oxygen system.

5.1 Experimental Results

All experiments were conducted at 1 atm total pressure, and followed the procedures described in Chapter 2. Most experiments were performed in 0.21 O_2 partial pressure; additional runs were made with O_2 partial pressure between 0.1 atm and 1.0 atm. All samples were heated in situ at 1173K for about 15 minutes prior to a run. The reactivity determined from the TGA system was actually a combination of the true reaction rate and the chemisorption rate of oxygen. The latter, nevertheless, was found to be negligible after a short induction period (see the discussion in section 5.51). So the rate measured by the TGA system will be equivalent to the rate of carbon oxidation.

5.11 Reactivities of ST1 at Different Temperatures

The weight change of ST1 sample during an isothermal oxidation in air was measured in the TGA system. Reaction rate was obtained by taking the derivative of the weight loss curve with respect to time. The weight loss curves at different reaction temperatures are presented in Fig. 5.1, and corresponding reactivities as a function of carbon conversion* in

---

* In this chapter, the carbon conversion is defined as the percentage of carbon consumption due to oxidation. It is different from the definition used in the preceding chapters.

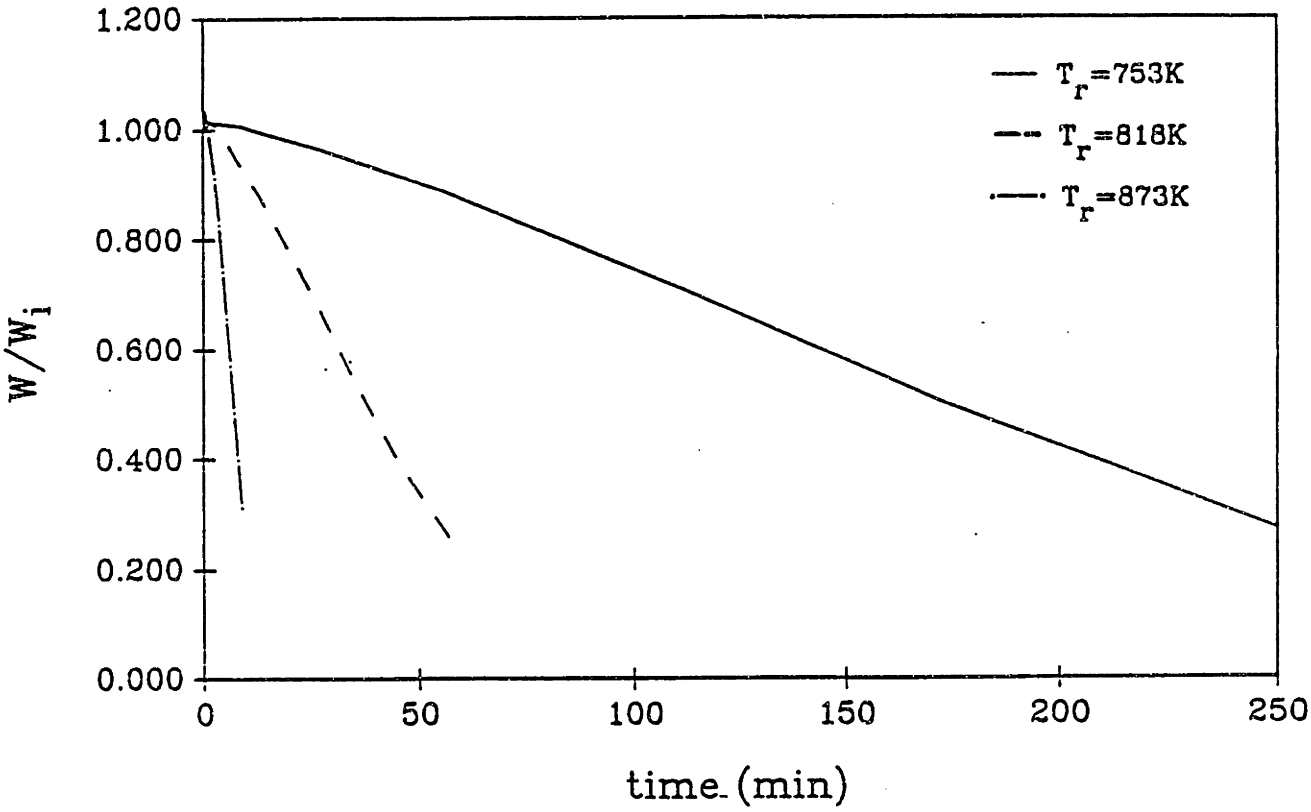

Fig. 5.1 Weight change of ST1 during oxidation at different temperature.

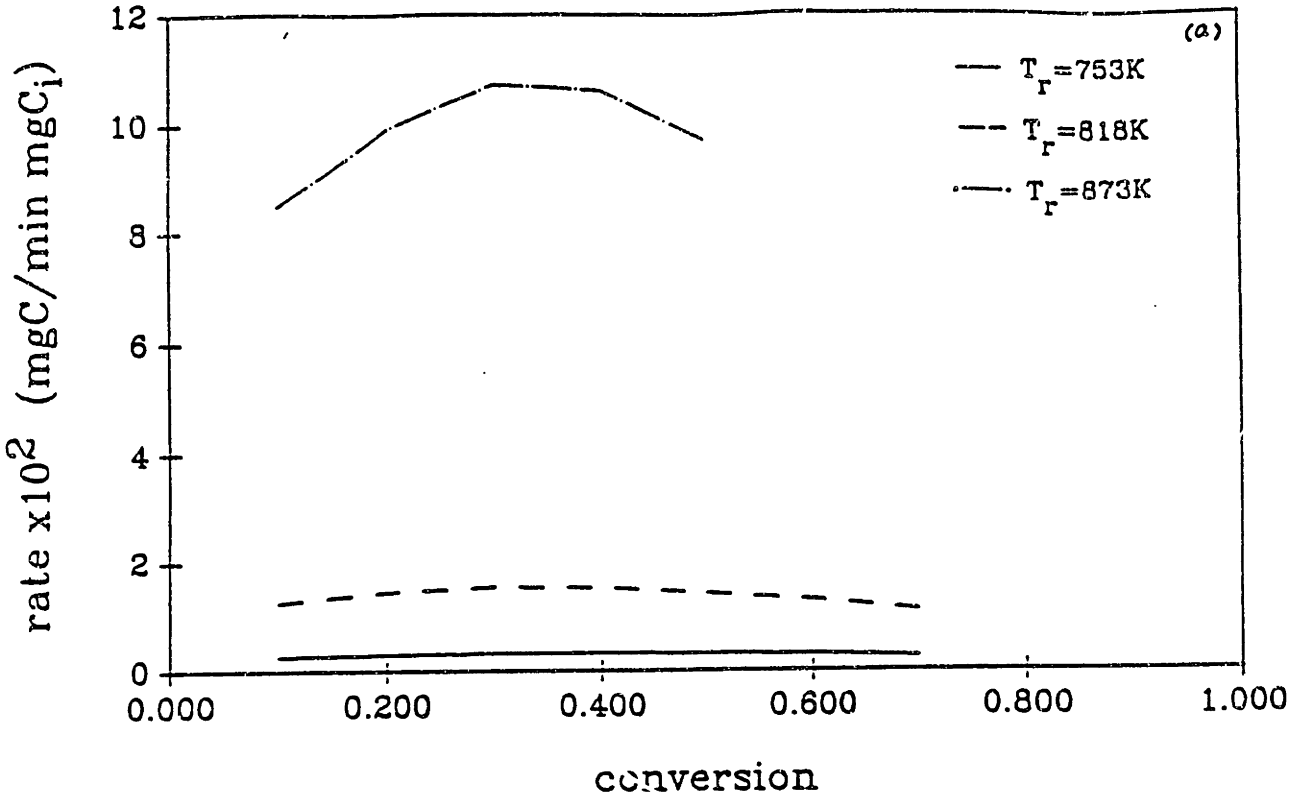

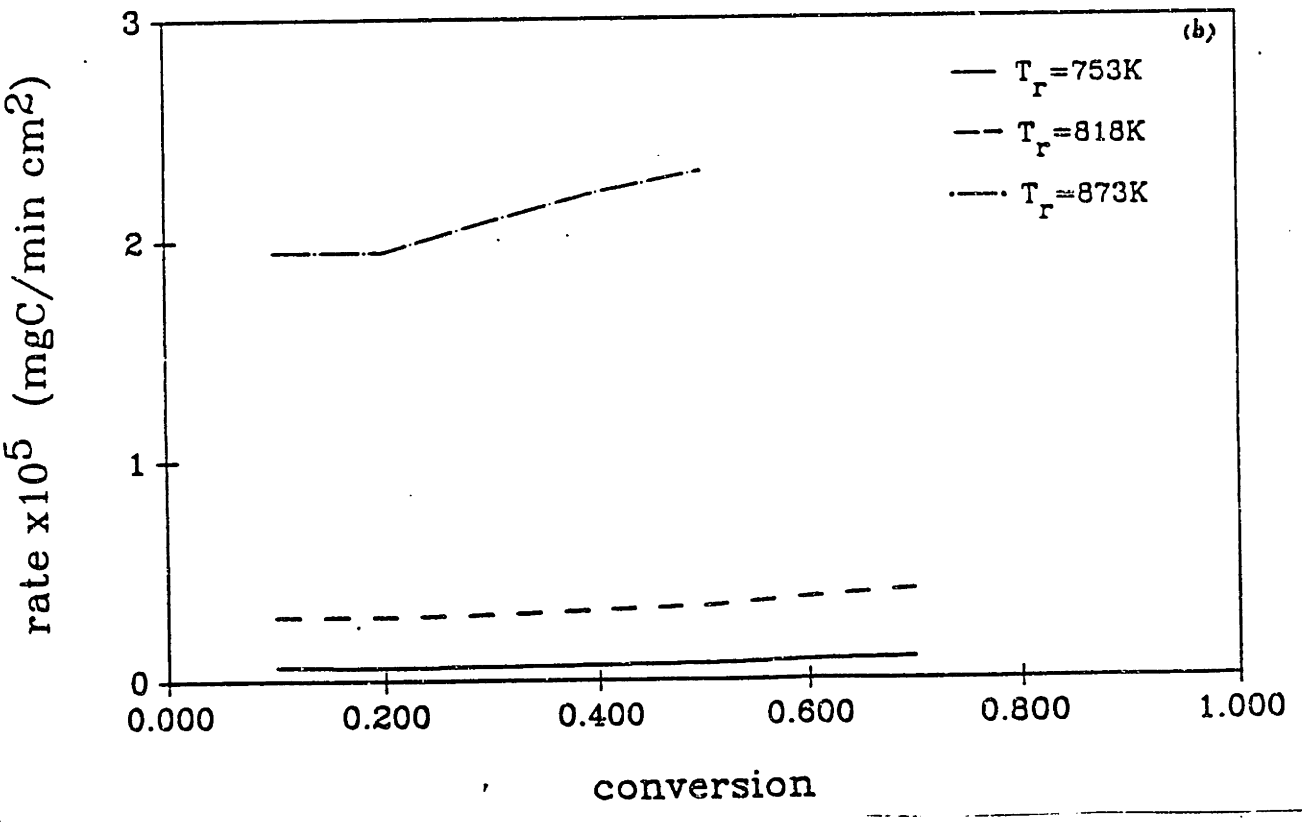

Fig. 5.2 Reactivities of ST1 at different temperature.
(a) Reactivity per unit initial weight vs conversion
(b) Reactivity per unit surface area vs conversion

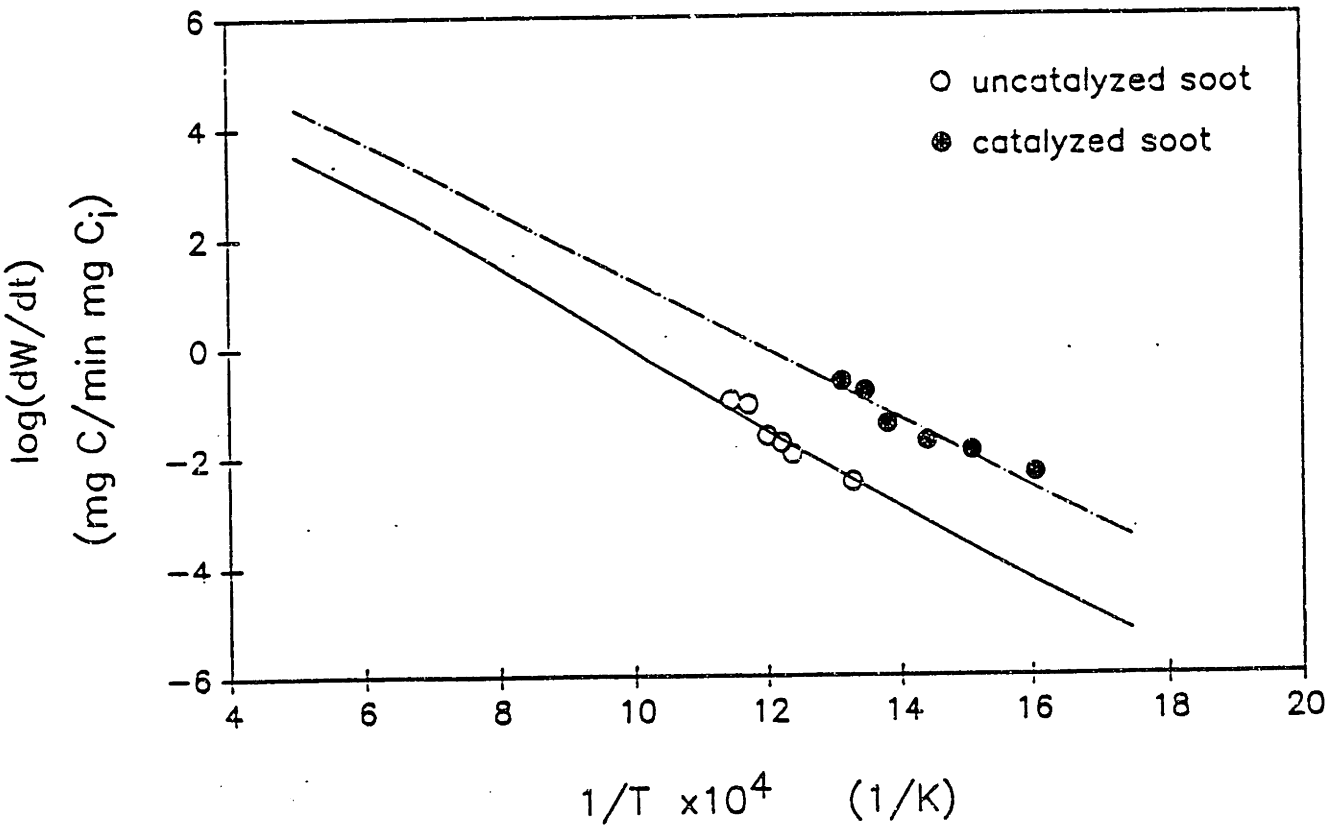

Fig. 5.3 Arrhenius rate plot for ST1 and ST2 oxidation at 30% conversion.

Note: Symbols represent experimental data and line represents simulation results from the model.

Fig.5.2a,b. The reactivity per unit surface area of carbon was found to be approximately constant in the reaction (see Fig. 5.2b), indicating the proportionality between the surface area and the reactivity of carbon. Those reactivities at 30% conversion and different reaction temperatures are also given in the Arrhenius plot of Fig. 5.3, which shows an apparent activation energy of ~34 kcal/mol around 818K.

5.12 CO/CO_2 in ST1 Oxidation.

The tube-furnace-MS arrangement was used to measure the rates of CO and CO_2 formation during carbon oxidation. Both CO and CO_2 were found to be primary products in the ST1 oxidation, and the product ratio, CO/CO_2, is virtually a constant after a short induction period (see Fig.5.4). CO/CO_2 increases with increased reaction temperature (see Fig. 5.5a) and with decreased partial pressure of O_2 in the reactant (see Fig. 5.5b). (Possibility of secondary gas phase reaction was eliminated because of the low reaction temperature.) Similar trends about CO/CO_2 were also reported by Tognotti et al [28] for spherocarb, Phillips et al [27] for Graphon, Bonnetain et al [25] for graphite, and Otterbein et al [26] for vitreous carbon.

5.13 Reaction Order with Respect to Partial Pressure of O_2

Increase in reactivity with O_2 concentration was observed in the ST1 oxidation, and reactivity could be correlated with a fractional order of 0.83 with respect to the oxygen partial pressure at 818K (see Fig. 5.6 and Table 5.1). Since the overall reaction rate is the summation of the CO and CO_2 formation rates, the order for CO_2 rate and CO rate could be separately

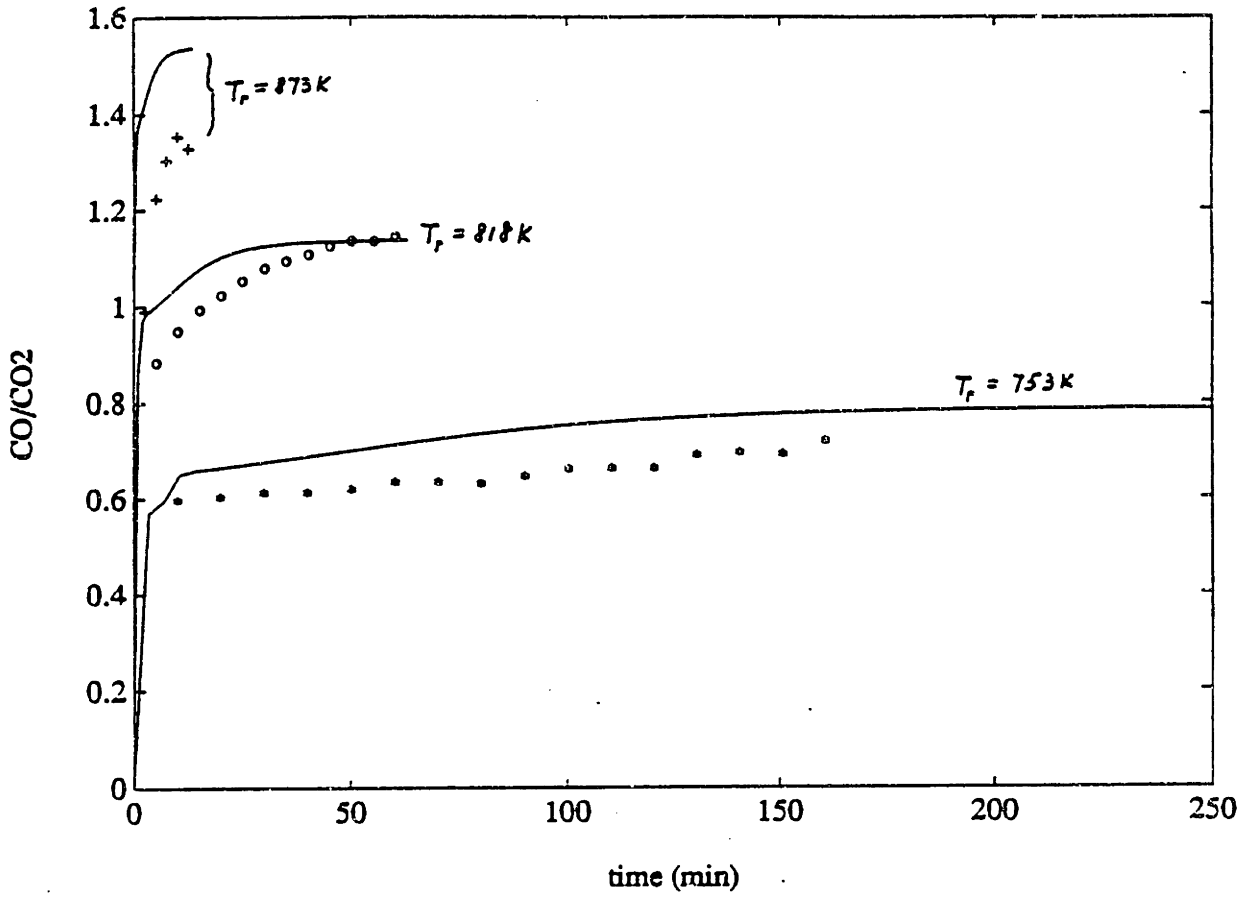

Fig. 5.4 CO/CO_2 ratio in ST1 oxidation.

Note: Symbols represent experimental data and line represents simulation results from the model.

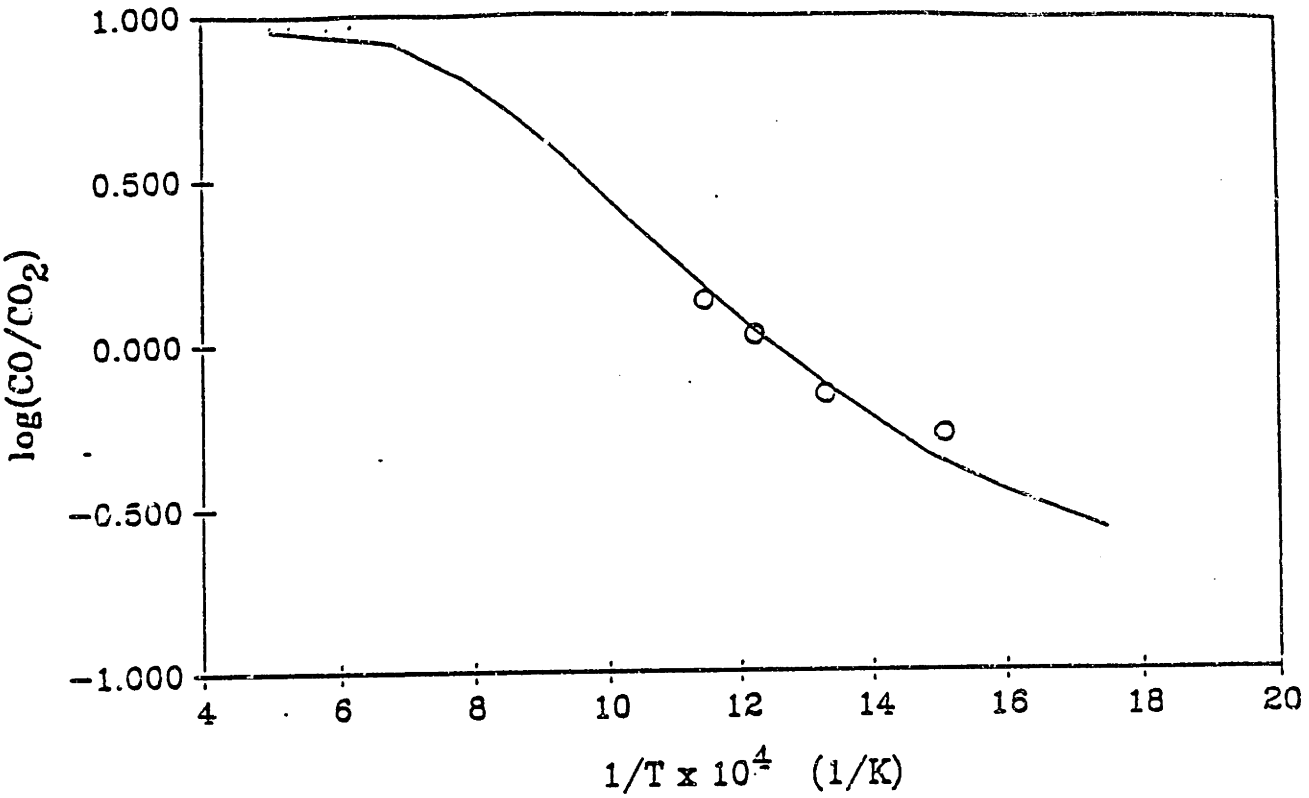

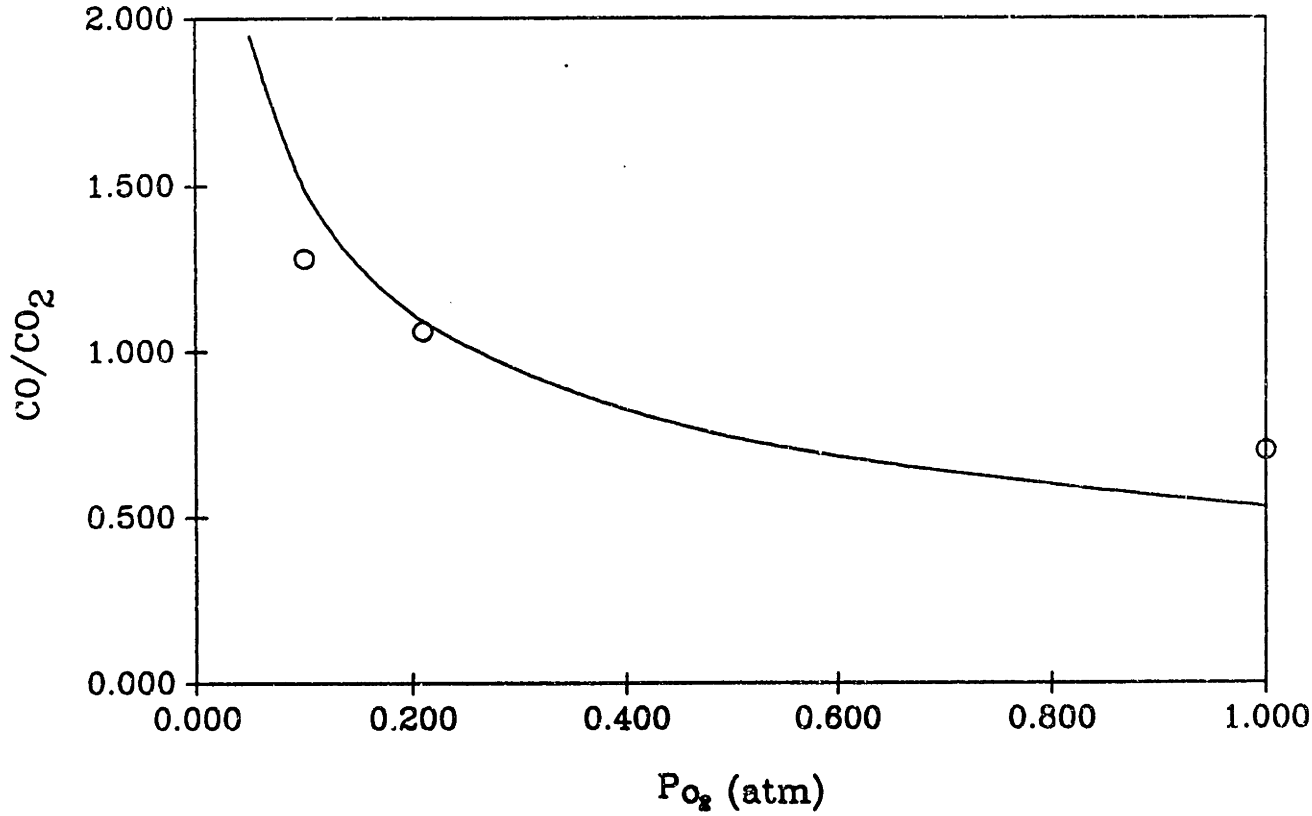

Fig. 5.5 CO/CO_2 ratio in ST1 oxidation at 30% conversion for different T and Po_2.

(a) $\log(CO/CO_2)$ vs 1/T (b) CO/CO_2 vs Po_2

Note: Symbols represent experimental data and line represents simulation results from the model.

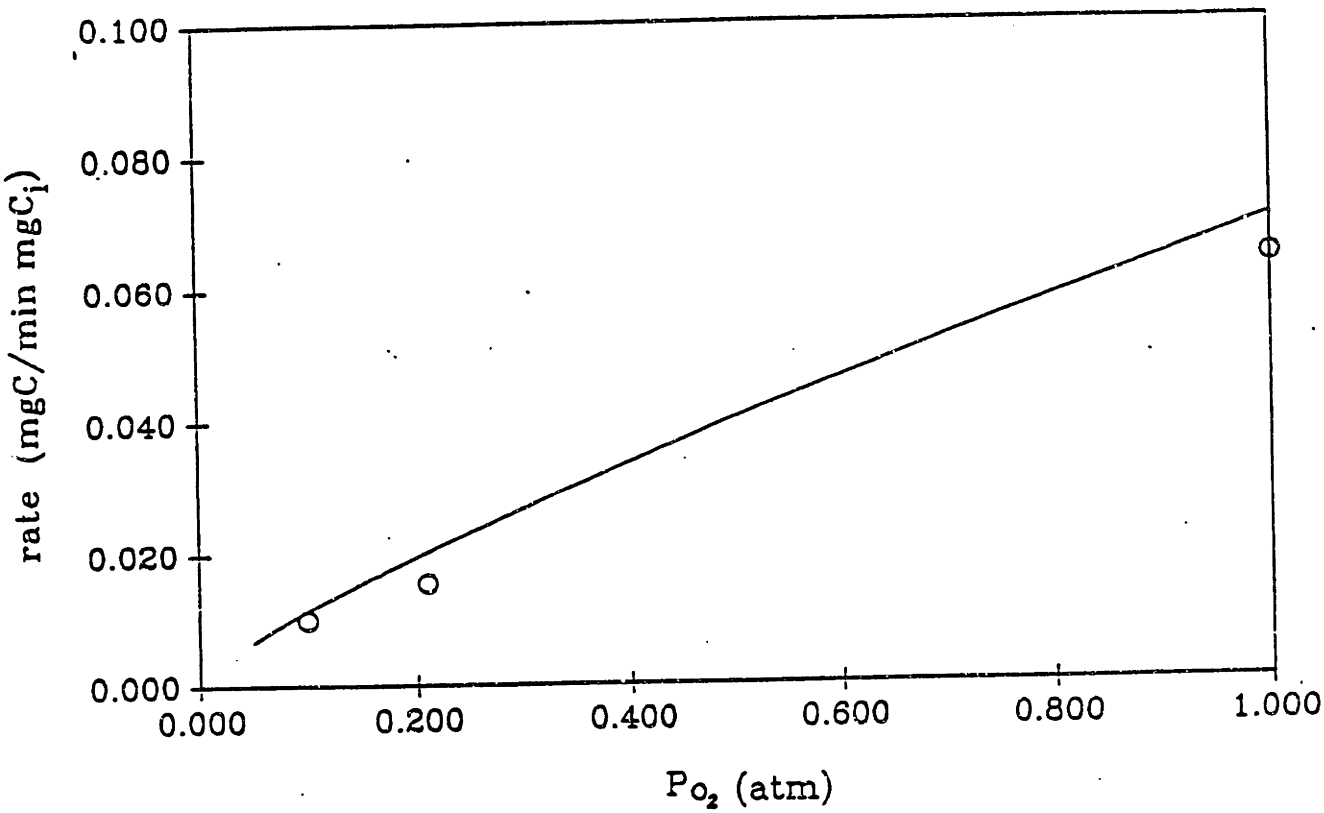

Fig. 5.6 Overall reaction rate at 30% conversion for different P_{O_2}.

Note: Symbols represent experimental data and line represents simulation results from the model.

found to be near 1.0 and 0.77, respectively, using the information of CO/CO_2 (see also Table 5.1).

Table 5.1 Reaction Order for ST1 Oxidation at 818 K

P_{O_2} (atm)	r^a (mg/min.mgC$_i$)	$\frac{CO}{CO_2}$	$r^b_{CO_2}$ (mg/min.mgC$_i$)	r^c_{CO} (mg/min.mgC$_i$)
0.1	0.010	1.28	4.39×10^{-3}	5.61×10^{-3}
0.21	0.0155	1.06	7.52×10^{-3}	7.98×10^{-3}
1.0	0.064	0.70	0.0376	0.0264
order	0.826		0.948	0.688

a: $r = r_{CO} + r_{CO_2}$ overall reaction rate in the ST1 oxidation at 30% conversion.
b: r_{CO_2} is CO_2 rate in the ST1 oxidation at 30% conversion.
c: r_{CO} is CO rate in the ST1 oxidation at 30% conversion.

5.14 Desorption

As discussed in the previous chapter, CO was observed as the major product in desorption process, while CO_2 was only barely observed (see Table 4.1). The TPD data presented in chapter 4 strongly showed that a variety of activation energies was involved in the desorption process. This multi-activation-energy behavior may be either due to the different local carbon surface structures, or due to the variation of long-range-electron interactions at different adsorbed oxygen coverages [79]. A proper oxygen isotope experiment could in principle identify which one will be responsible for the multi-activation-energy behavior. Scrambling between

O^{16} and O^{18}, however, made it difficult to draw any meaningful conclusion about (C-O) complex desorption from the isotope experiment (see the next section and Appendix? for detail). In this Thesis, we assume that the complexity of the carbon surface structure leads to the multi-activation-energy behavior in desorption.

5.15 Oxygen Isotope Experiments

A set of oxygen experiments was designed and conducted at Exxon to study some possible mechanisms and examine the role of (C-O) complex in the carbon oxidation by means of the transient technique (see Appendix E). In the isotope experiments, the ST1 sample was first reacted with O_2^{16-16} to about 20% conversion; and then transient process was started by switching the reactant from a $Ar+O_2^{16-16}$ mixture to a $Ar+O_2^{18-18}$ mixture. The gaseous products in the transient period were continuously sampled and analyzed by MS to obtain CO and CO_2 concentrations as functions of time.

The only meaningful observation in this isotope experiment was that change in CO_2 concentration closely followed change of O_2 concentration during the transient process, which indicates that the CO_2 formation in carbon oxidation is due to direct reaction of carbon with O_2, not due to the desorption of (C-O) complex on the carbon surface.

Other information obtained from the oxygen isotope experiment was not conclusive for the following reasons:

1) O_2 in the gas sample oxidizes the MS filament to form extra CO and CO_2 which contaminate the MS signals. The extra CO_2 generated from the filament oxidation can be separated from the 'true' CO_2 signal by passing the gaseous sample through a GC column before the MS measurement.

However, the CO signal can not be effectively separated in this way because O_2 peak and CO peak from the GC column are too close to be distinguished. That was why no conclusion about CO formation could be drawn from the isotope experiment.

2) Oxygen isotopes of O^{16} and O^{18} in O_2, CO and CO_2 gas species scramble (for detail see Appendix E), which totally invalidates the oxygen isotope distribution between the CO and CO_2 gas species.

Therefore, the oxygen isotope technique can not be employed unless the scrambling problem could be avoided.

5.16 Effect of Calcium Catalyst on Carbon Oxidation

The Ca catalyzed oxidation was investigated using the 2 wt% Ca soot, ST2. The measured reactivity of ST2 was about 50 times larger than that of ST1 around 763 K (see Fig. 5.3). A further study of the individual CO and CO_2 rates in the ST2 oxidation revealed that the CO rate was almost not affected by the addition of Ca, but that the CO_2 rate was drastically catalyzed (see Fig. 5.7a,b). The CO/CO_2 ratio, as a result, decreased from 0.53 in the ST1 oxidation to a very small value, $\sim 7 \times 10^{-3}$, in ST2 oxidation. The similar result was also found by Harker et al [51] for irradiated nuclear graphite catalyzed by potassium.

The possibility of secondary gas phase reaction under the Ca catalyzed carbon oxidation condition was examined by feeding about 2800 ppm CO in the reactant and monitoring CO_2 concentration change before and after the CO feed. Fig. 5.8 shows that the CO_2 signal was not affected by the extra CO feed to the Ca catalyzed oxidation system up to 698K, indicating the secondary gas phase reaction was not significant under the experimental conditions for the Ca catalyzed soot.

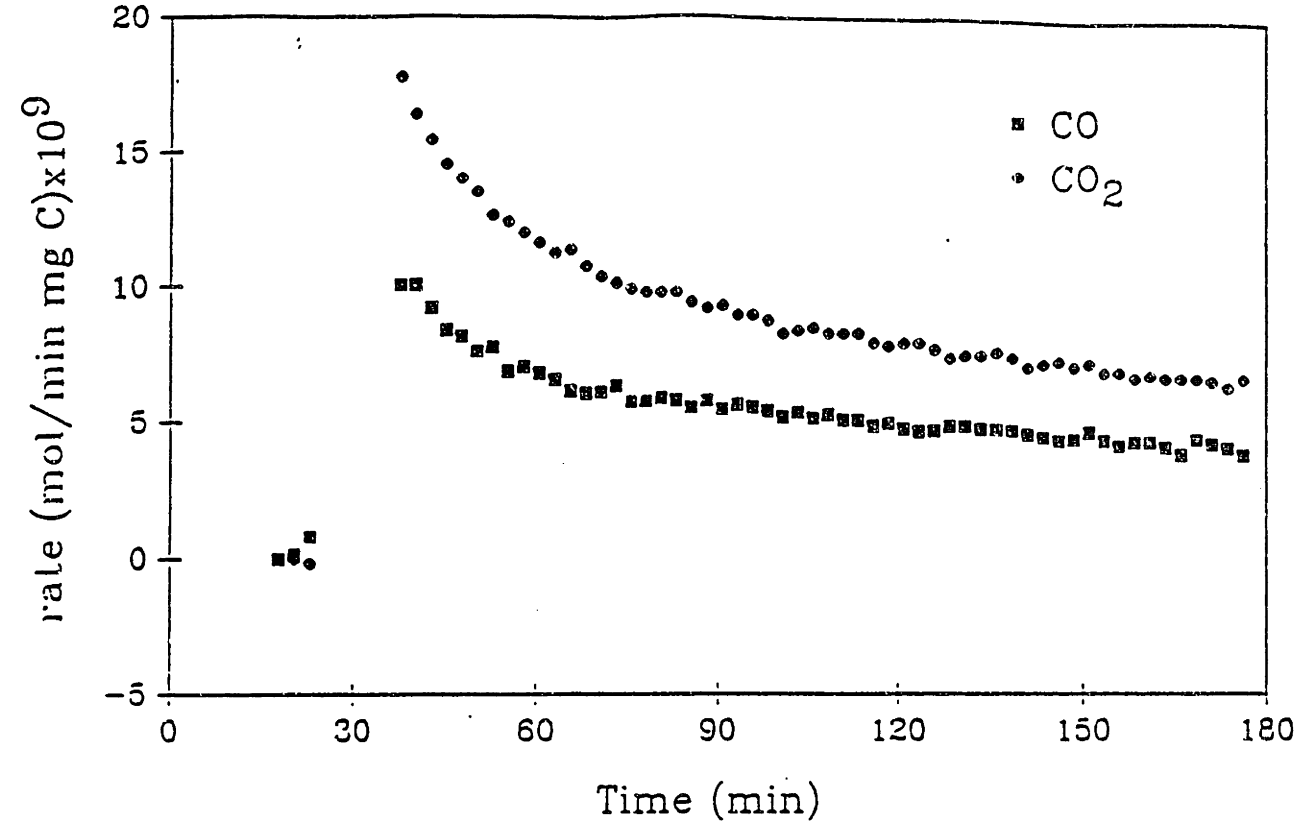

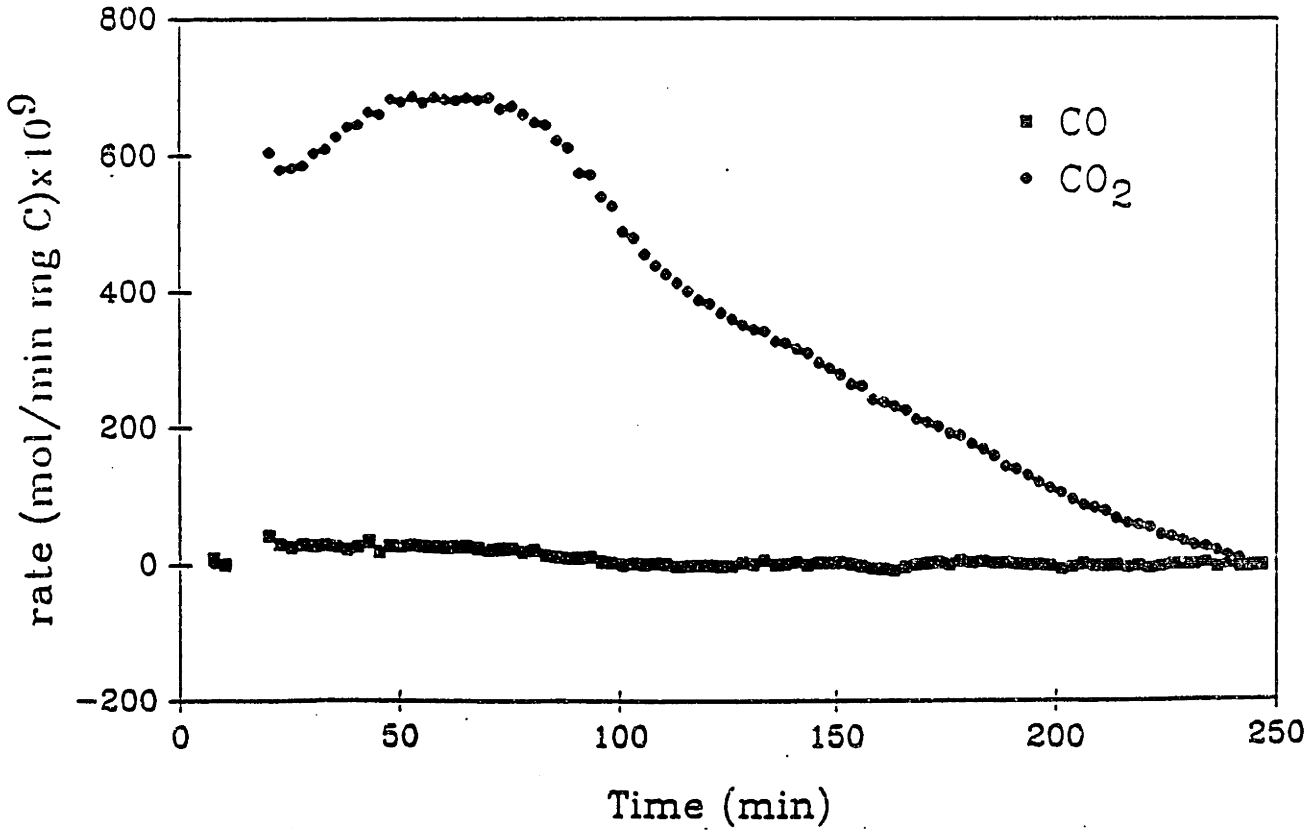

Fig. 5.7 CO and CO_2 generations in carbon oxidation at 663 K.
(a) ST1 oxidation (b) ST2 oxidation

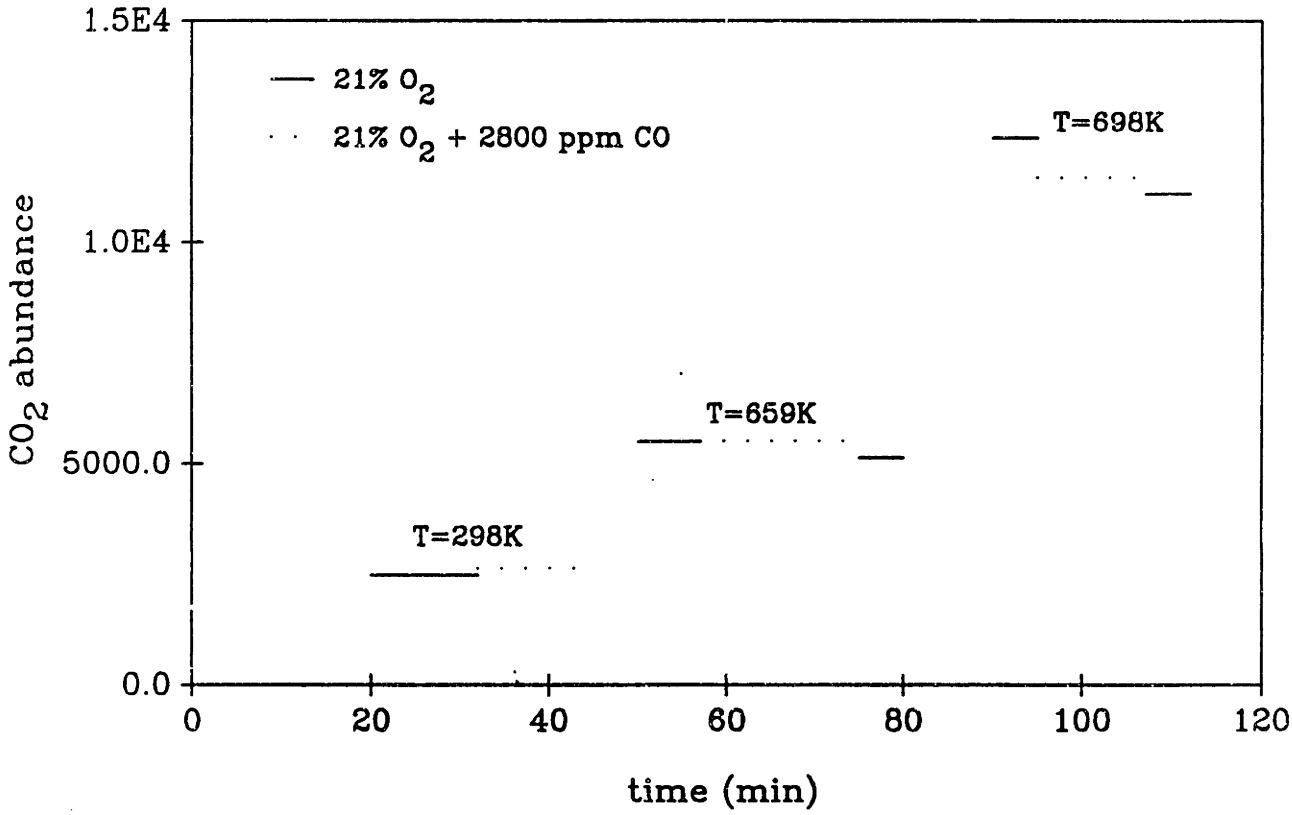

Fig. 5.8 A test of secondary gas phase reaction in Ca catalyzed carbon oxidation.

The desorption study depicted in the previous chapter showed that the activation energy distribution of ST2 exhibits double peaks and that one of them corresponds to the addition of Calcium (see Fig. 4.8).

5.2 Model Formulation (Oxidation)

5.21 Basic Features of the Reaction Model

The following aspects should be considered in order to explain the experimental results described above:

1) Although small amount of CO_2 may be obtained from a desorption process, the CO_2 generation in the carbon oxidation is not primarily from the desorption step. That is because (a) CO/CO_2 is about 16 to 1 in the desorption, but around 1 to 1 in the oxidation (see Table 4.1 & Table 5.1); (b) The rate of CO_2 generation is near first order with respect to the partial pressure of oxygen (see also Table 5.1); (c) Change in CO_2 concentration closely follows the change of O_2 concentration during transient process (see Appendix E).

2) The CO product in the oxidation may be generated from the desorption of (C-O) complex. As discussed in Chapter 4, this desorption process involves multi-activation-energies.

3) Since the desorption of (C-O) complexes involves a distribution of activation energies, the formation of these (C-O) complexes, i.e. adsorption, may involve a similar energy distribution.

4) The addition of Ca catalyst effectively increases the rate of CO_2 formation during carbon oxidation, but does not affect the rate of CO formation (see Fig. 5.7a,b).

5.22 Oxidation Model

Based on the proceeding discussion, the following mechanisms were proposed for the carbon oxidation:

$$C_{f,E} + O_2 \xrightarrow{k1} (C\text{-}O_2)^*_E \qquad \text{(R5.1)}$$

$$(C\text{-}O_2)^*_E + C_{f,E'} \xrightarrow{k2} (C\text{-}O)_E + (C\text{-}O)_{E'} \qquad \text{(R5.2)}$$

$$(C\text{-}O)_E \xrightarrow{k3} CO \qquad \text{(R5.3)}$$

$$C + O_2 \xrightarrow{k4} CO_2 \qquad \text{(R5.4)}$$

where subscript f denotes the free carbon sites available for adsorption and subscript E denotes those carbon sites with the site energy between E and E+ΔE. Reactions (R5.1) to (R5.3) are similar to (R1.6) to (R1.9) in Chapter 1, accounting for the CO generation in carbon oxidation. Instead of the two-site assumption used in (R1.6) to (R1.9), a continuous site energy distribution is employed in reactions (R5.1) and (R5.3) for the reasons discussed in Section 5.21. Since little experimental evidence for the CO_2 generation has been observed except for the first order dependence on O_2 partial pressure, a simple reaction mechanism (R5.4) is assumed in the present model to account for the CO_2 generation during carbon oxidation.

The following assumptions were made in order to simplify the model calculation:

1) The adsorption and desorption steps, i.e., (R5.1) and (R5.3), depend on the energy distribution of the carbon for the reasons given above. Both distributions for the adsorption and desorption were assumed to be Gaussian.

For uncatalyzed carbon (ST1):

$$f_a(E_a) \equiv \frac{1}{\sqrt{2\pi}\,\sigma_a} \exp[-\frac{(E_a - \bar{E}_a)^2}{2\sigma_a^2}] \tag{5.1}$$

$$f_d(E_d) \equiv \frac{1}{\sqrt{2\pi}\,\sigma_d} \exp[-\frac{(E_d - \bar{E}_d)^2}{2\sigma_d^2}] \tag{5.2}$$

and for catalyzed carbon (ST2):

$$f_a(E_a) \equiv \frac{1}{\sqrt{2\pi}}\{\frac{A}{\sigma_{a1}}\exp[-\frac{(E_a - \bar{E}_{a1})^2}{2\sigma_{a1}^2}] + \frac{B}{\sigma_{a2}} \exp[-\frac{(E_a - \bar{E}_{a2})^2}{2\sigma_{a2}^2}]\} \tag{5.3}$$

$$f_d(E_d) \equiv \frac{1}{\sqrt{2\pi}}\{\frac{A}{\sigma_{d1}}\exp[-\frac{(E_d - \bar{E}_{d1})^2}{2\sigma_{d1}^2}] + \frac{B}{\sigma_{d2}} \exp[-\frac{(E_d - \bar{E}_{d2})^2}{2\sigma_{d2}^2}]\} \tag{5.4}$$

where subscripts a and d denote adsorption and desorption respectively. According to the desorption study, these distributions, $f_a(E_a)$ and $f_d(E_d)$, were assumed not to change with carbon conversion (see Fig. 4.10).

It was further assumed that the carbon sites corresponding to the same adsorption activation energy E_a will have the same desorption activation energy E_d. In other words, if E_a corresponds to a position, say, one standard deviation away from the mean, in the $f_a(E_a)$, E_d will correspond to a similar position, i.e., one standard deviation away from the mean, in the $f_d(E_d)$. This assumption led to the following relations between E_a and E_d:

for ST1,

$$\frac{E_a - \bar{E}_a}{\sigma_a} = \frac{E_d - \bar{E}_d}{\sigma_d} \tag{5.5}$$

for ST2,

$$\frac{E_a - \bar{E}_{a1}}{\sigma_{a1}} = \frac{E_d - \bar{E}_{d1}}{\sigma_{d1}} \tag{5.6}$$

and $$\frac{E_a - \bar{E}_{a2}}{\sigma_{a2}} = \frac{E_d - \bar{E}_{d2}}{\sigma_{d2}} \tag{5.7}$$

Eliminating E_d from Eq's (5.6) and (5,7) generates:

$$\bar{E}_{d1} - \bar{E}_{d2} = \left(\frac{\sigma_{d1}}{\sigma_{a1}} \bar{E}_{a1} - \frac{\sigma_{d2}}{\sigma_{a2}} \bar{E}_{a2} \right) - \left(\frac{\sigma_{d1}}{\sigma_{a1}} - \frac{\sigma_{d2}}{\sigma_{a2}} \right) E_a \tag{5.8}$$

Since $\bar{E}_{a1}$, σ_{a1}, $\bar{E}_{a2}$, σ_{a2}, $\bar{E}_{d1}$, σ_{d1}, $\bar{E}_{d2}$, and σ_{d2} are constant, we must set

$$\frac{\sigma_{d1}}{\sigma_{a1}} = \frac{\sigma_{d2}}{\sigma_{a2}} \tag{5.9}$$

in order to validate Eq.(5.8) for all values of E_a.

2) Rate constants k_1 and k_3 in (R5.1) and (R5.3) are of the Arrhenius form, i.e.,

$$k_1 = k_{1,o} \exp\left(-\frac{E_a}{RT}\right) \tag{5.10}$$

and $$k_3 = k_{3,o} \exp\left(-\frac{E_d}{RT}\right) \tag{5.11}$$

3) $(C\text{-}O_2)^*$ is an unstable complex, which will be easily converted to a stable complex (C-O) whenever its adjacent site is available. Therefore, the reaction (R5.2) is extremely fast, and does not depend on the site energy distribution of the carbon.

4) The mechanism (R5.4) with a single activation energy is designated for the CO_2 generation during the carbon oxidation. CO_2 can be only produced on the special carbon sites, called CO_2-site. The population of the CO_2-site

is expected to be very small, because the rate of CO_2 formation was found to be dropped to zero with almost no transient period after oxygen supply was switched off (see Appendix E).

5) The addition of catalyst increases the CO_2-sites on the carbon surface, and thus catalyzes the rate of CO_2 formation. The increase in the CO_2-sites is proportional to the amount of catalyst added to the carbon sample if the catalyst loading is small (< 3 wt%).

6) The total number of carbon sites available for the reaction, $[C]_{tot}$, is assumed to be proportional to the surface area obtained by the CO_2 isotherms in TGA (see Chapter 3).

5.3 Model Development (Oxidation)

5.31 Non-catalytic Carbon Oxidation

5.311 Dimensionless Variables

For a non-catalytic carbon oxidation, adsorption and desorption energy distributions, or Eq.(5.1) & Eq.(5.2), are normalized by introducing a non-dimensional parameter $y_s \equiv \frac{E_a - \bar{E}_{a1}}{\sigma_{a1}} = \frac{E_d - \bar{E}_{d1}}{\sigma_{d1}}$. Therefore,

$$f_a(E_a)dE_a = f_d(E_d)dE_d \equiv f(y_s)dy_s = \frac{1}{\sqrt{2\,\pi}} \exp(-\frac{y_s^2}{2})dy_s$$

The site coverages on the surface were defined as:

$$\theta_{o,y_s} \equiv \frac{[C_f]_{y_s}}{[C]_{tot} f(y_s)dy_s}; \qquad \theta_o \equiv \frac{[C_f]}{[C]_{tot}} = \int_{-\infty}^{\infty} \theta_{o,y_s} f(y_s)dy_s$$

$$\theta_{1,y_s} \equiv \frac{[C\text{-}O]_{y_s}}{[C]_{tot} f(y_s) dy_s}; \qquad \theta_1 \equiv \frac{[C\text{-}O]}{[C]_{tot}} = \int_{-\infty}^{\infty} \theta_{1,y_s} f(y_s) dy_s$$

$$\theta_{2,y_s} \equiv \frac{[C\text{-}O_2]^*_{y_s}}{[C]_{tot} f(y_s) dy_s}; \qquad \theta_2 \equiv \frac{[C\text{-}O_2]^*}{[C]_{tot} f(y_s) dy_s} = \int_{-\infty}^{\infty} \theta_{2,y_s} f(y_s) dy_s$$

with $\theta_{o,y_s} + \theta_{1,y_s} + \theta_{2,y_s} = 1$, and $\theta_o + \theta_1 + \theta_2 = 1$.

The reaction time and all rate constants in the model were non-dimensionalized using a desorption time scale, which was defined as the reciprocal of the overall desorption rate, $\bar{k}_3$, under desorption control ($\theta_{1,y_s}=1$) condition, i.e.,

$$\bar{k}_3 \equiv \int_{-\infty}^{\infty} k_{3,o} \exp(-\frac{E_d}{RT}) f_d(E_d) dE_d$$

$$= k_{3,o} \exp[-\frac{\bar{E}_d}{RT} + \frac{1}{2}(\frac{\sigma_d}{RT})^2] \quad (1/min.)$$

Thus, $\tau \equiv \bar{k}_3 t$,

and $b_1 \equiv \dfrac{k_{1,o} \exp(-\frac{\bar{E}_a}{RT})\ P_{O_2}}{\bar{k}_3}$, $\quad b_2 \equiv \dfrac{\bar{k}_3}{k_2}$, $\quad b_4 \equiv \dfrac{k_4\ P_{O_2}}{\bar{k}_3}$

where P_{O_2} is the partial pressure of O_2 in reactant.

5.312 Governing Equations

According to the mechanisms proposed in the model, the rate equations for each site energy interval (y_s to y_s+dy_s) can be written as:

$$\frac{\partial \theta_{o,y_s}}{\partial \tau} = -\frac{\theta_{o,y_s}}{[C]_{tot}} \frac{d[C]_{tot}}{d\tau} + \frac{1}{b_2}(\theta_o \theta_{2,y_s} + \theta_{o,y_s} \theta_2) - \theta_{1,y_s} \exp[-(y_s + \frac{\sigma_d}{2RT})\frac{\sigma_d}{RT}] \quad (5.12)$$

$$\frac{\partial \theta_{2,y_s}}{\partial \tau} = -\frac{\theta_{2,y_s}}{[C]_{tot}} \frac{d[C]_{tot}}{d\tau} + b_1 \theta_{o,y_s} \exp(-y_s \frac{\sigma_d}{RT}) - \frac{\theta_o}{b_2} \theta_{2,y_s} \quad (5.13)$$

the overall rate equations are:

$$\frac{d[CO_2]}{d\tau} = [C]_{tot}\, b_4 \tag{5.14}$$

$$\frac{d[CO]}{d\tau} = [C]_{tot} \int_{-\infty}^{\infty} \exp[-(y_s + \frac{\sigma_d}{2RT})\frac{\sigma_d}{RT}] f(y_s)\theta_{1,y_s} dy_s \tag{5.15}$$

$$\frac{dx}{d\tau} = \frac{1}{[m]_i}(\frac{d[CO]}{d\tau} + \frac{d[CO_2]}{d\tau}) \tag{5.16}$$

where x is the percentage of carbon conversion defined as:

$$x \equiv (1 - \frac{[m]}{[m]_i}) \tag{5.17}$$

[m] is the amount of carbon remaining in the oxidation (mmol), and the subscript i denotes the initial condition of that quantity.

The initial conditions for these rate equations are:

$$\text{at } \tau = 0,\ \theta_{o,y_s} = 1,\ \theta_{1,y_s} = \theta_{2,y_s} = 0, \text{ for all } y_s$$

$$[CO] = [CO_2] = 0, \text{ and } x = 0$$

Evolution of $[C]_{tot}$ during the oxidation can be related to the evolution of surface area, according to the assumption 6 in section 5.22,

$$\frac{[C]_{tot}}{[C]_{tot,i}} = \frac{S_A}{S_{A,i}} \tag{5.18}$$

The site density of 7.137×10^{-7} mmol site/cm^2 on the carbon surface was calculated as from the average $[C\text{-}O]_{tot}$ in Table 4.1.

Once all the rate constants, energy distributions and surface area evolution are known, the whole oxidation process can be simulated by

solving the rate equations from Eq. (5.12) to Eq. (5.16) with their initial conditions. Furthermore, the sample weight during the oxidation can be also calculated according to

$$W = 12\ [m]_i \{\frac{16}{12}\ [C]_{tot}\ (2\theta_2 + \theta_1) + (1 - x)\} \qquad (5.19)$$

5.32 Catalytic Carbon Oxidation

All governing equations for a catalytic carbon oxidation are similar to those for the non-catalytic oxidation discussed above, except several points mentioned below:

1) The activation energy distributions for adsorption and desorption are bimodal Gaussian, which are different from those in the non-catalytic reaction. Nevertheless, these two energy distributions can be still normalized by letting $y_s \equiv \frac{E_a - \bar{E}_{a1}}{\sigma_{a1}} = \frac{E_d - \bar{E}_{d1}}{\sigma_{d1}}$, i.e.,

$$f_a(E_a)dE_a = f_d(E_d)dE_d \equiv f(y_s)dy_s$$

$$= \frac{1}{\sqrt{2\pi}} \{A\exp(-\frac{y_s^2}{2}) + B\frac{\sigma_1}{\sigma_2} \exp[-\frac{\sigma_1^2}{2\sigma_2^2} (y_s - \frac{\bar{E}_2 - \bar{E}_1}{\sigma_1})^2]\}dy_s$$

2) The time scale used in a catalytic oxidation is an average desorption time with respect to the first peak of $f_d(E_d)$,

$$\text{i.e.} \qquad (\bar{k}_3)^{-1} \equiv \{k_{3,o}\exp[-\frac{\bar{E}_{d1}}{RT} + \frac{1}{2}(\frac{\sigma_{d1}}{RT})^2]\}^{-1} \text{ (min.)}$$

3) The rate constant k_4 in the mechanism (R5.4) is significantly increased due to the catalytic effect.

4) The number of CO_2-sites on the ST2 surface should depend on the amount of catalyst in the ST2 sample and on the dispersiveness of the catalyst. For the fresh ST2, the Ca loading is low (~2 wt%) so that the calcium can be atomically dispersed on the external ST2 surface (see also Sections 2.12 & 3.4), and CO_2-sites, or reactivity, should not vary with carbon conversion at the beginning of oxidation. However, as more carbon is reacted away during oxidation, the Ca loading will be saturated and the calciums will stick together to form agglomerates. The number of CO_2-sites, or reactivity, is hence expected to decrease and vary with surface area at high carbon conversion. The evolution of the catalytic reactivity as a function of carbon conversion is not investigated in detail in this thesis. Future work in this regard is needed. In the model calculation, the evolution of the CO_2-sites during the ST2 oxidation was assumed to follow the evolution of the ST2 surface area discussed in Chapter 3.

5.4 Application to the Soot-Oxygen Reaction

5.41 Determination of Carbon Surface Area, Rate Constants and Energy Distributions

Assumed to be extremely fast, the mechanism (R5.2) would not significantly affect the overall behavior of the oxidation. Therefore, a big number ($>10^{13}$/min) was assigned to k_2 such that the whole oxidation process would be independent of the k_2 value chosen.

5.411 ST1 Material

A scheme described in Fig. 5.9 was used to determine the rate constants, surface area evolution and energy distributions for the ST1 sample.

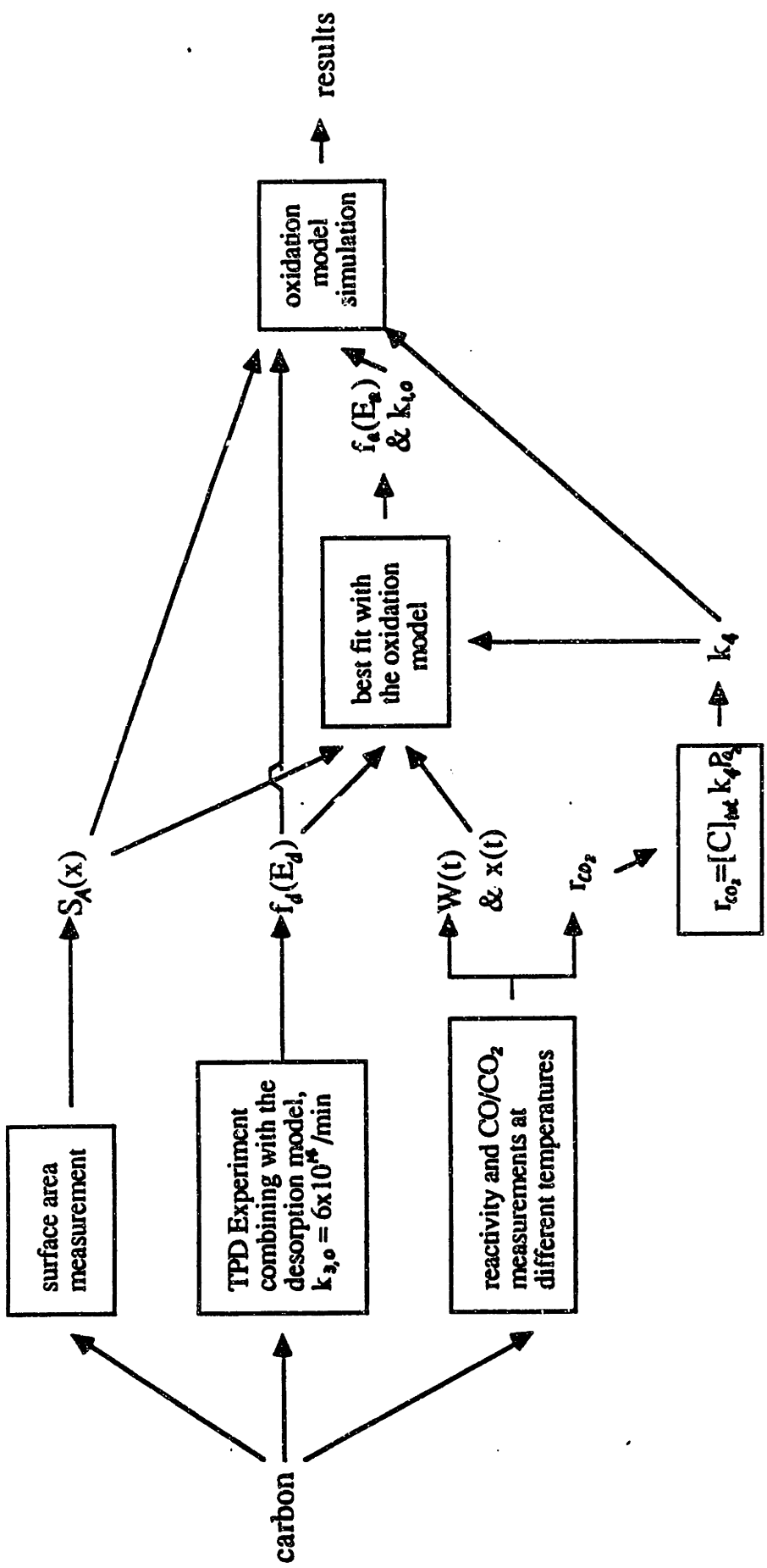

Fig. 5.9 Methodology to determine kinetic data for a specific carbon.

The surface area evolution was obtained from the CO_2 adsorption isotherms as aforementioned in Chapter 3. Since the definition of conversion in this chapter is different from that in Chapter 3, the surface area expression in Chapter 3 should corrected accordingly to account for the initial ~3.5% weight loss during the preheat-treatment prior to oxidation,

$$\frac{S_A}{S_{A,i}} = [1 + 2.638(1 - e^{-4.253x})](1 - x), \quad \text{and } S_{A,i} \approx 252.2 \ m^2/g$$

where the factor (1-x) converts area per unit remaining carbon to area per unit initial carbon.

The energy distribution for desorption is found from TPD data using the desorption model aforementioned in chapter 4. If $k_{3,o}$ was taken as 6×10^{14}/min, then

$$f_d(E_d) \equiv \frac{1}{\sqrt{2\pi}\,\sigma_d} \exp[-\frac{(E_d - \bar{E}_d)^2}{2\sigma_d^2}]$$

with $\bar{E}_d = 69.7$ kcal/mol, $\sigma_d = 7.8$ kcal/mol.

k_4 is calculated from the measured reaction rate and CO/CO_2 using Eq.(5.14). k_4 values at three temperatures of 753K, 818K and 873K were calculated and correlated by an Arrhenius expression as

$$k_4 = 4.76 \times 10^7 \exp(-\frac{28.61}{RT}) \ (1/\text{min atm } O_2)$$

with R in kcal/mol K.

b_1 and σ_a, which are the parameters related to the energy distribution for adsorption, were chosen such that the weight loss curve could be best fitted by the model calculation. Table 5.2 lists the best fitted b_1 and σ_a values for temperature 735K, 818K and 873K.

Table 5.2

T (K)	b_1	$k_{1,o}\exp(-\frac{\bar{E}_a}{RT})P_{O_2}=b_1k_3$ (1/min)	σ_a (kcal/mol)
753	0.0892	0.250	1.517
818	0.0572	0.818	1.305
873	0.0672	3.520	1.875

From the third column of Table 5.2, $k_{1,o}$ and $\bar{E}_a$ were found to be 1.918×10^8 (1/min atm O_2) and 28.41 kcal/mol respectively, via an Arrhenius plot (see Fig. 5.10), and from the fourth column of Table 5.2 the average σ_a value was found to be 1.57 kcal/mol.

In summary,

$$\frac{S_A}{S_{A,i}} = [1 + 2.638(1 - e^{-4.253x})](1 - x), \quad \text{and } S_{A,i}\approx 252.2 \text{ m}^2/\text{g}$$

$$k_{1,o} = 1.918\times10^8 \text{ (1/min atm } O_2)$$

$$f_a(E_a) \equiv \frac{1}{\sqrt{2\pi}\,\sigma_a} \exp[-\frac{(E_a - \bar{E}_a)^2}{2\sigma_a^2}]$$

$$\bar{E}_a = 28.41 \text{ kcal/mol}, \quad \sigma_a = 1.57 \text{ kcal/mol}$$

$$k_2 > 10^{13} \text{ (1/min.)}$$

$$k_{3,o} = 6\times10^{14} \text{ (1/min.)}$$

$$f_d(E_d) \equiv \frac{1}{\sqrt{2\pi}\,\sigma_d} \exp[-\frac{(E_d - \bar{E}_d)^2}{2\sigma_d^2}]$$

$$\bar{E}_d = 69.7 \text{ kcal/mol}, \quad \sigma_d = 7.8 \text{ kcal/mol}$$

$$k_4 = 4.76\times10^7\exp(-\frac{28.61}{RT}) \text{ (1/min atm } O_2)$$

with R in kcal/mol K.

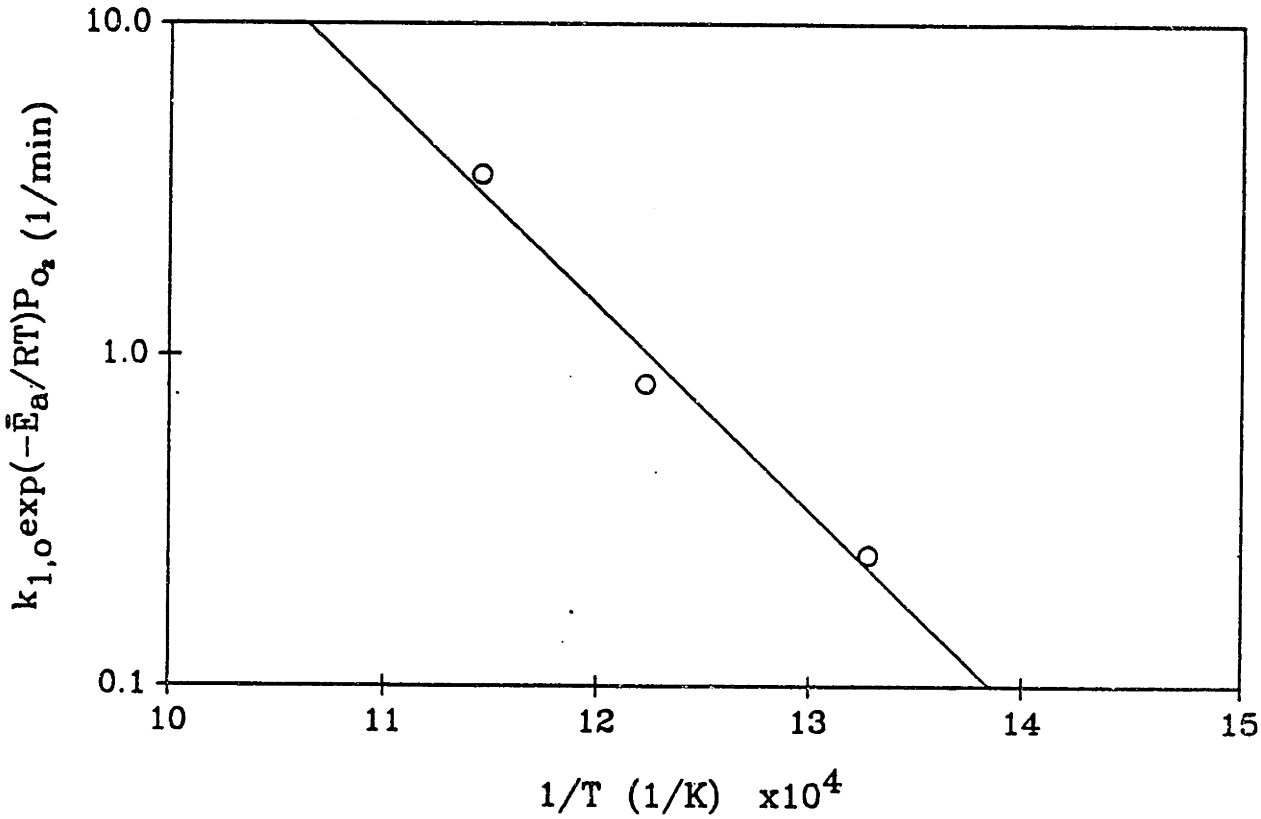

Fig. 5.10 Arrhenius plot of $k_{1,o}\exp(-\frac{\bar{E}_a}{RT})\,P_{O_2}$.

5.412 ST2 Material

For the ST2 sample, surface area evolution and $f_d(E_d)$ were similarly obtained from direct surface area measurement and TPD experiment, respectively, i.e.,

$$\frac{S_A}{S_{A,i}} = [1 + 0.338(1 - e^{-3.380x})](1 - x), \quad \text{and } S_{A,i} \approx 532.5 \ m^2/g$$

$$f_d(E_d) \equiv \frac{1}{\sqrt{2\pi}} \left\{ \frac{0.74}{\sigma_{d1}} \exp\left[-\frac{(E_d - \bar{E}_{d1})^2}{2\sigma_{d1}^2} \right] + \frac{0.26}{\sigma_{d2}} \exp\left[-\frac{(E_d - \bar{E}_{d2})^2}{2\sigma_{d2}^2} \right] \right\}$$

with $\bar{E}_{d1} = 67.9$ kcal/mol , $\sigma_{d1} = 7.82$ kcal/mol

and $\bar{E}_{d2} = 79.7$ kcal/mol , $\sigma_{d2} = 3.70$ kcal/mol

where the similar correction was made in the S_A expression in order to account for ~25% weight loss due to the pretreatment before the oxidation.

Since the mechanism (R5.4) was assumed to be catalyzed by the CO_2-sites increase upon the Ca addition, the activation energy of k_4 should be the same as that for ST1, or 28.61 kcal/mol. The pre-exponential of k_4 was calculated from the measured ST2 oxidation rate and CO/CO_2 at 663K,

$$k_{4,o} = 3.52 \times 10^9 \ (1/\text{min atm } O_2).$$

Regarding the energy distribution for adsorption, $k_{1,0}$ and the first peak of $f_a(E_a)$ were assumed to be the same as those for the ST1 sample, i.e.,

$$k_{1,0} = 1.918 \times 10^8 \ (1/\text{min atm } O_2)$$

$\sigma_{a1} = 1.57$ (kcal/mol.), $\bar{E}_{a1} = 28.41$ (kcal/mol.)

and the parameters for the second peak of $f_a(E_a)$ were calculated according to Eq.'s (5.8) and (5.9), or

$$\sigma_{a2} = \sigma_{a1} \frac{\sigma_{d2}}{\sigma_{d1}} \ , \text{ and } \ \bar{E}_{a2} = \bar{E}_{a1} + (\bar{E}_{d2} - \bar{E}_{d1}) \frac{\sigma_{a1}}{\sigma_{d1}}.$$

Above discussions lead to the following results for the ST2 sample:

$$\frac{S_A}{S_{A,i}} = [1 + 0.338(1 - e^{-3.380x})](1 - x), \quad \text{and } S_{A,i} \approx 532.5 \ m^2/g$$

$$k_{1,o} = 1.918 \times 10^8 \ (1/\text{min atm } O_2)$$

$$f_a(E_a) \equiv \frac{1}{\sqrt{2\pi}} \{ \frac{0.74}{\sigma_{a1}} \exp[-\frac{(E_a - \bar{E}_{a1})^2}{2\sigma_{a1}^2}] + \frac{0.26}{\sigma_{a2}} \exp[-\frac{(E_a - \bar{E}_{a2})^2}{2\sigma_{a2}^2}] \}$$

with $\bar{E}_{a1} = 28.41$ kcal/mol, $\sigma_{a1} = 1.57$ kcal/mol

and $\bar{E}_{a2} = 30.77$ kcal/mol, $\sigma_{a2} = 0.74$ kcal/mol

$k_2 > 10^{13}$ (1/min.)

$k_{3,o} = 6 \times 10^{14}$ (1/min.)

$$f_d(E_d) \equiv \frac{1}{\sqrt{2\pi}} \{ \frac{0.74}{\sigma_{d1}} \exp[-\frac{(E_d - \bar{E}_{d1})^2}{2\sigma_{d1}^2}] + \frac{0.26}{\sigma_{d2}} \exp[-\frac{(E_d - \bar{E}_{d2})^2}{2\sigma_{d2}^2}] \}$$

with $\bar{E}_{d1} = 67.9$ kcal/mol, $\sigma_{d1} = 7.82$ kcal/mol

and $\bar{E}_{d2} = 79.7$ kcal/mol, $\sigma_{d2} = 3.70$ kcal/mol

$$k_4 = 3.52 \times 10^9 \exp(-\frac{28.61}{RT}) \ (1/\text{min atm } O_2)$$

with R in kcal/mol K.

5.42 Results from the Model Simulation

The proposed model was applied to simulate both ST1 and ST2 oxidation under different oxidation conditions, using the rate constants, energy distributions and surface area evolutions obtained in the last section. A variable-order, variable-step Gear method was employed to perform the simulations on a VAX Station (detailed Fortran code can be found in Appendix F).

All results from the simulations are presented in Fig. 5.11 to Fig. 5.17 as well as in Fig. 5.3 to Fig. 5.6. In these figures, the results from the

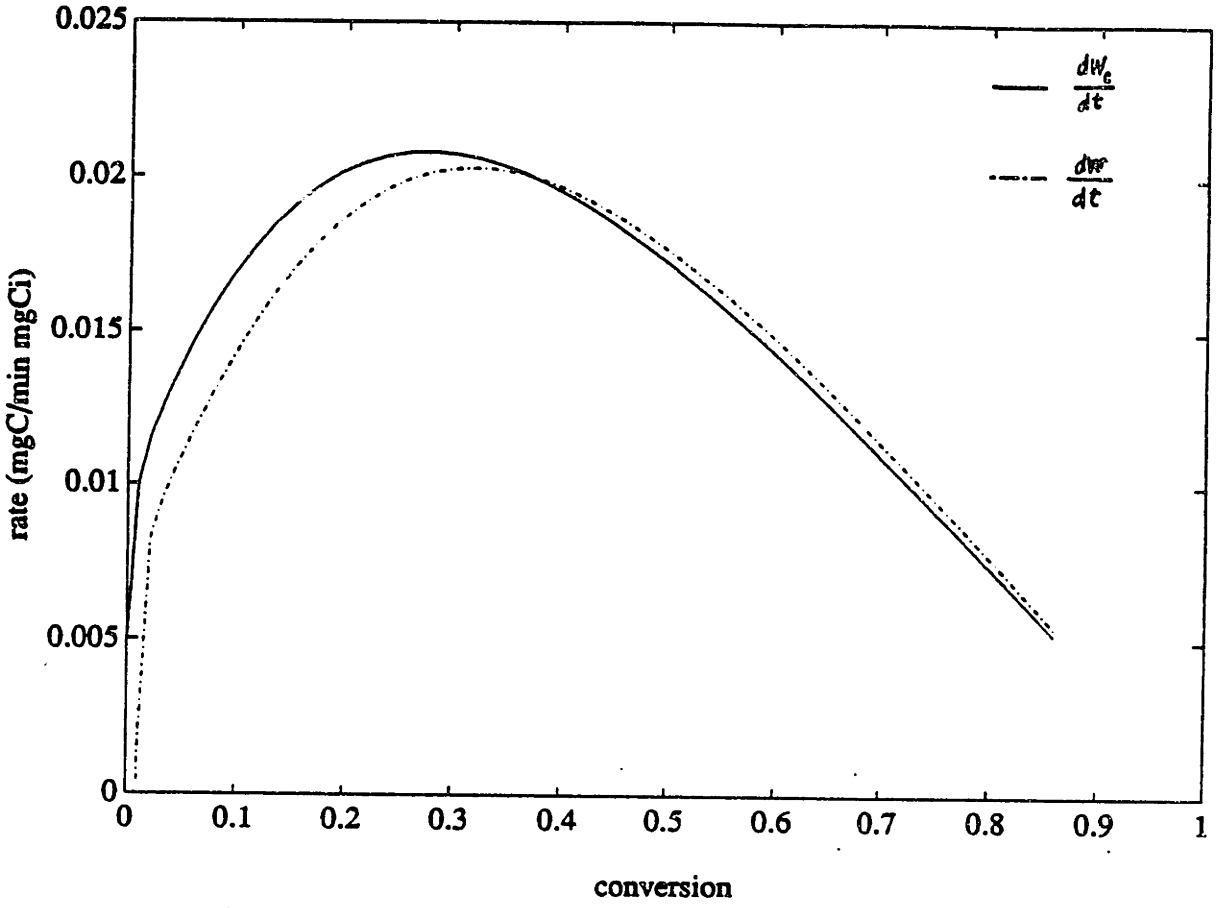

Fig. 5.11 A comparison between $\frac{dW}{dt}$ and $\frac{dW_c}{dt}$ at 818K for ST1.

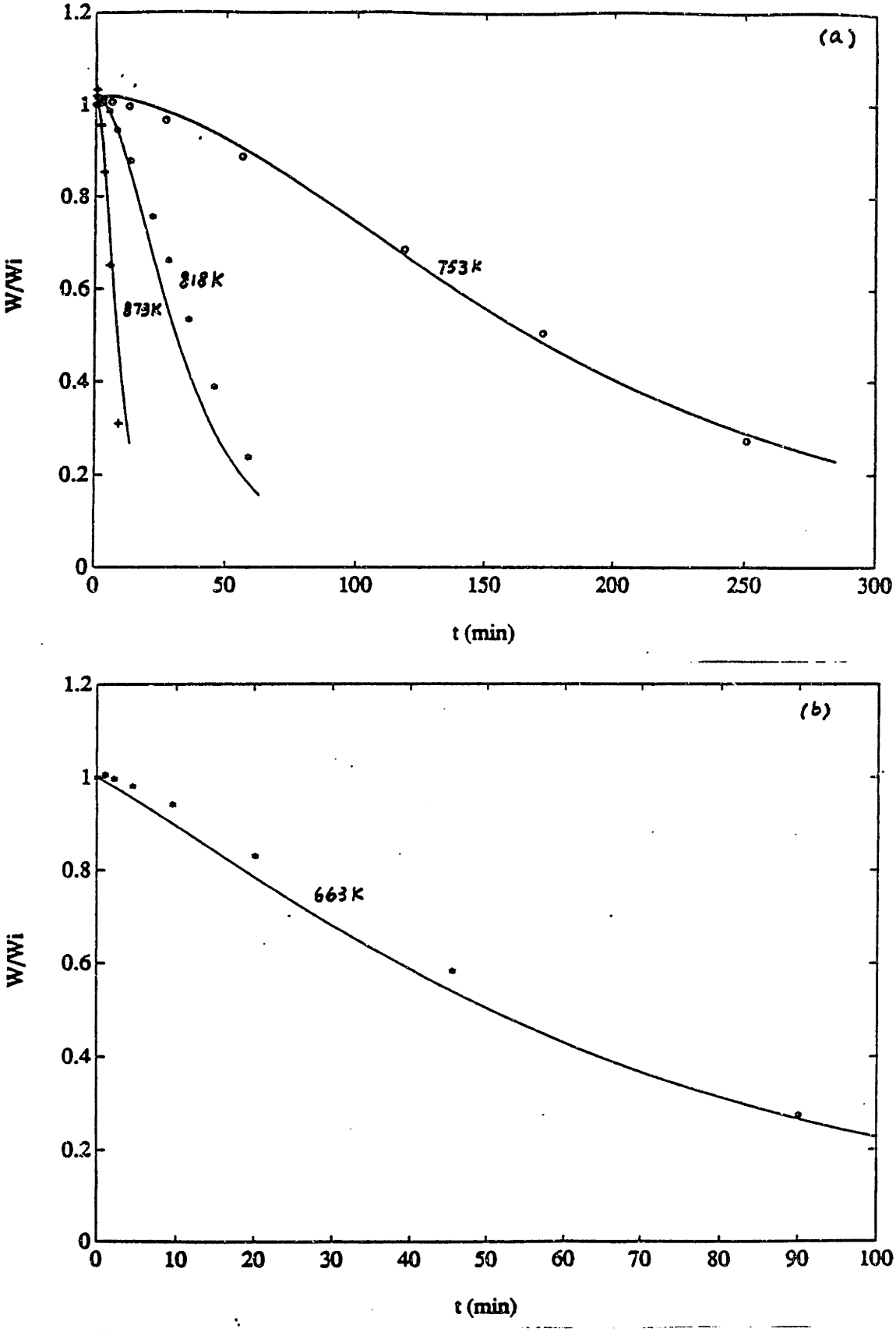

Fig. 5.12 Carbon weight change during oxidation.
(a) ST1 (b) ST2

Note: Symbols represent experimental data and line represents simulation results from the model.

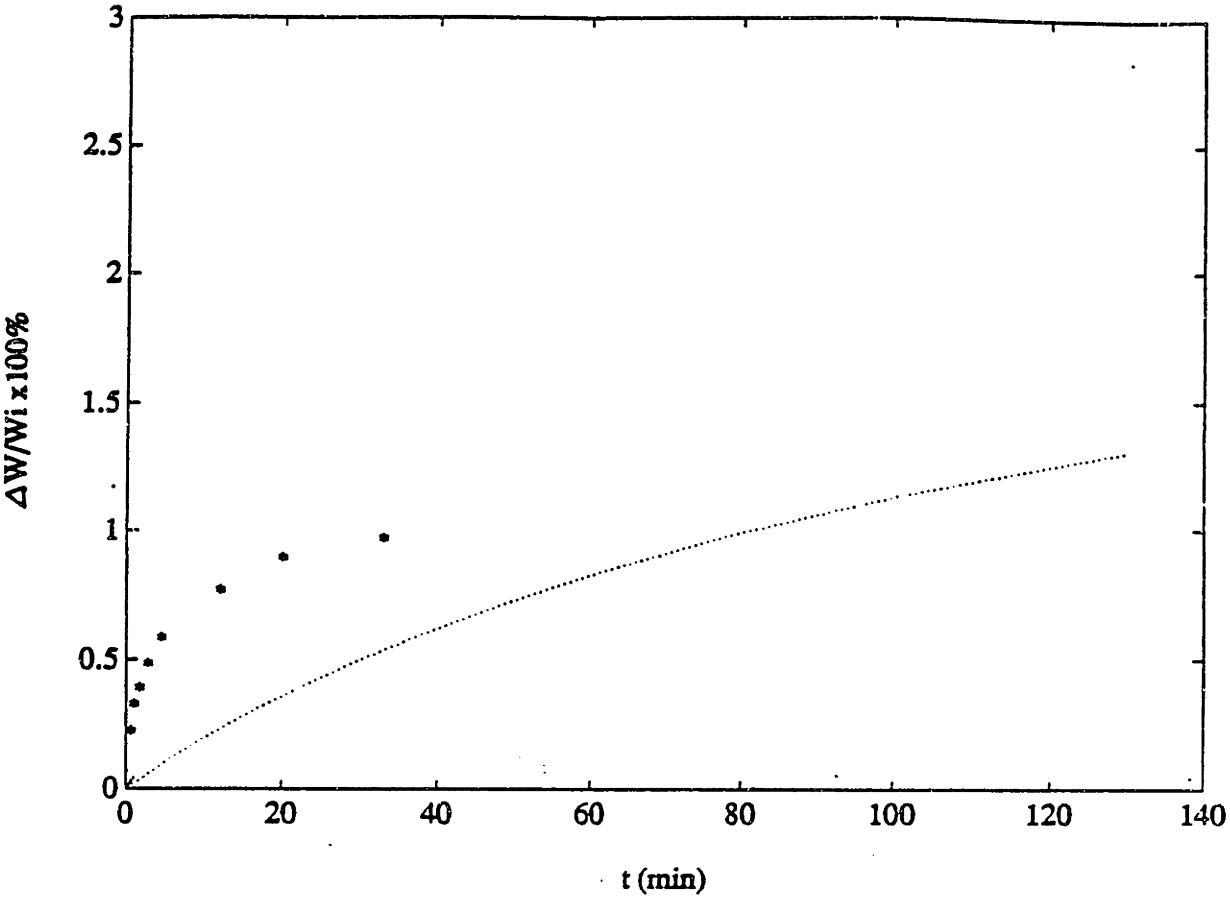

Fig. 5.13 Weight uptaking curve at 598K for 0% conversion ST1.

Note: Symbols represent experimental data and line represents simulation results from the model.

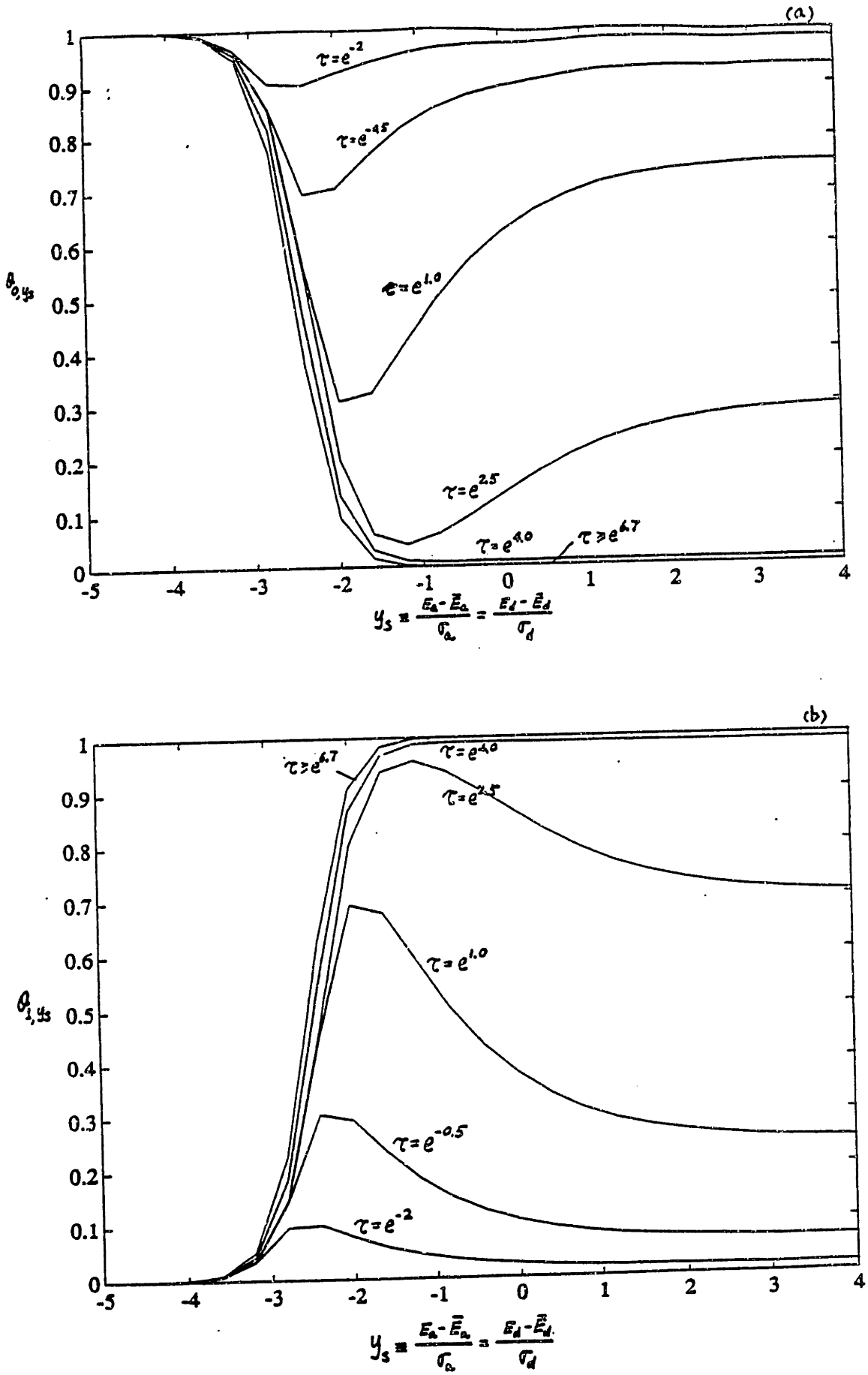

Fig. 5.14 Evolusion of site coverage during the ST1 oxidation at 818K.
(a) θ_{0,y_s} vs y_s (b) θ_{1,y_s} vs y_s

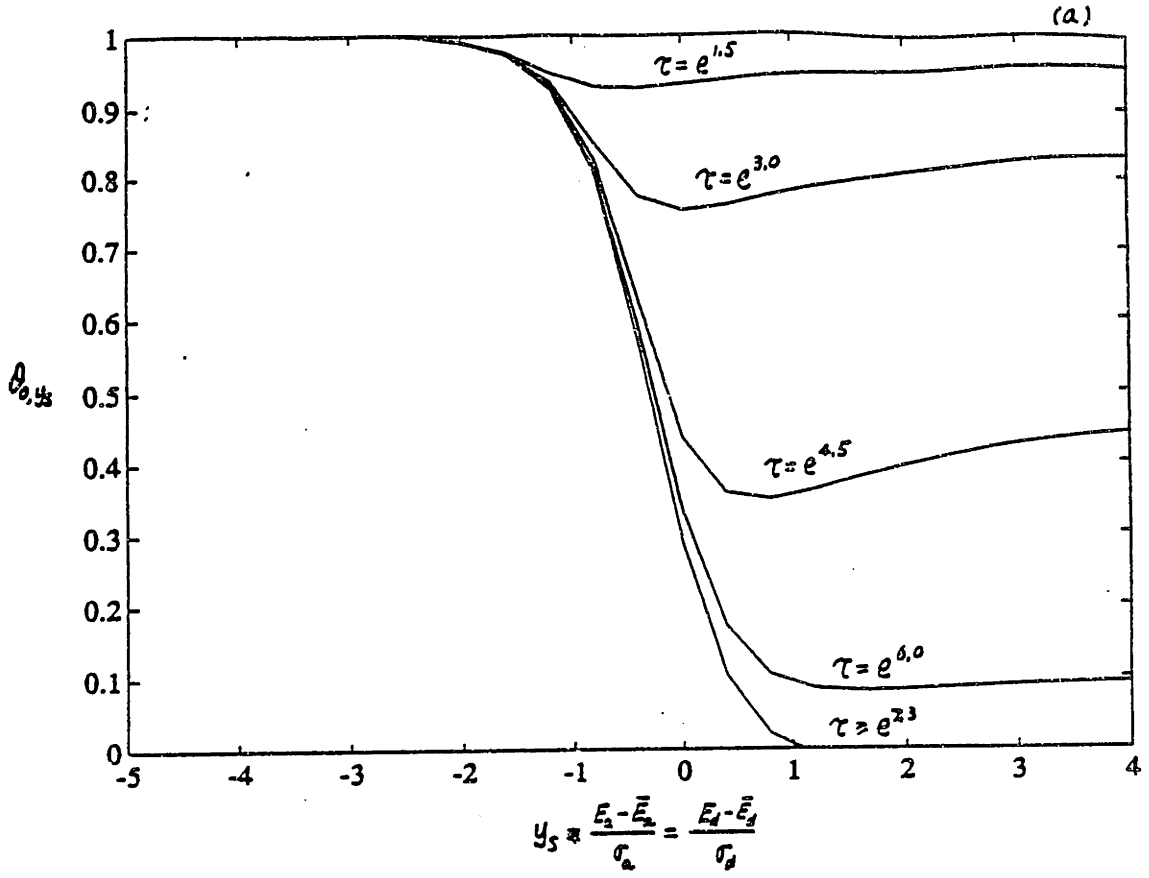

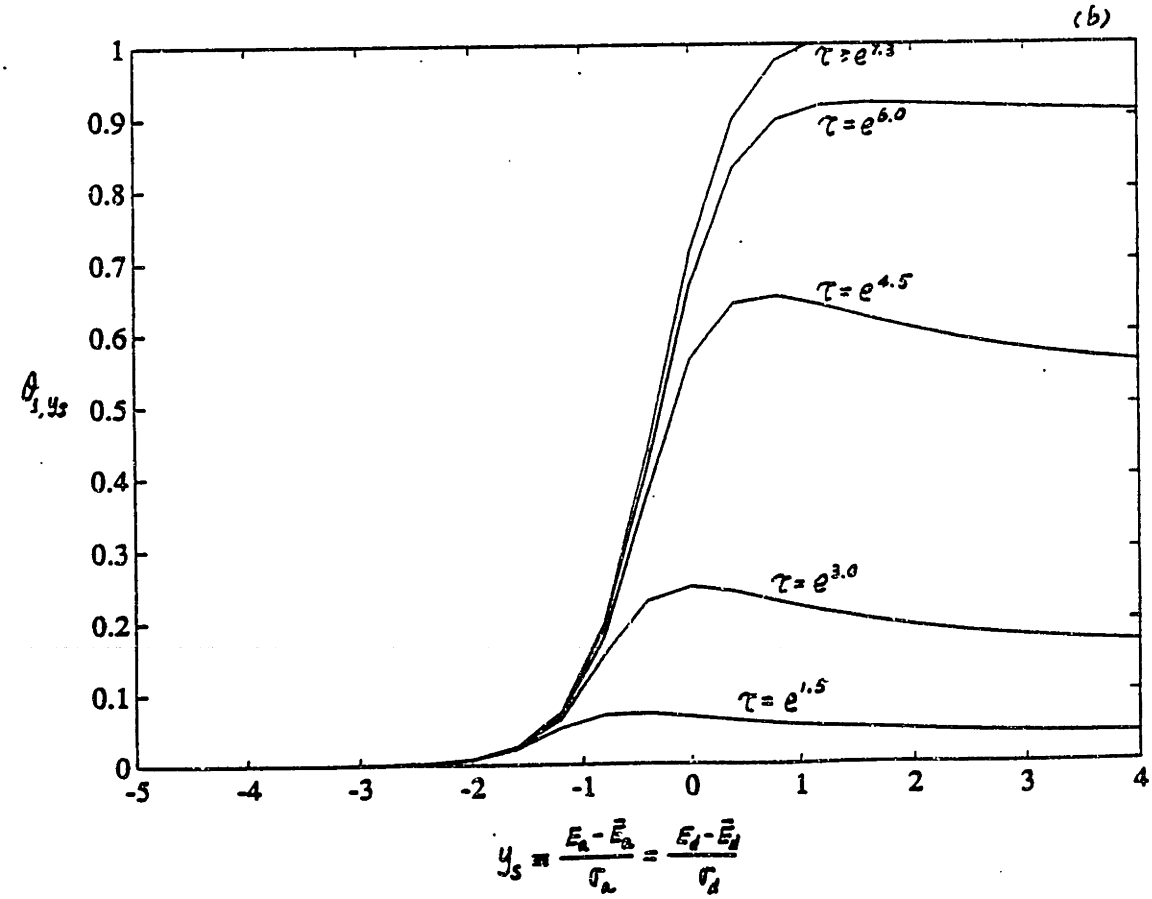

Fig. 5.15 Evolusion of site coverage during the ST1 oxidation at 1273K.
(a) θ_{0,y_s} vs y_s (b) θ_{1,y_s} vs y_s

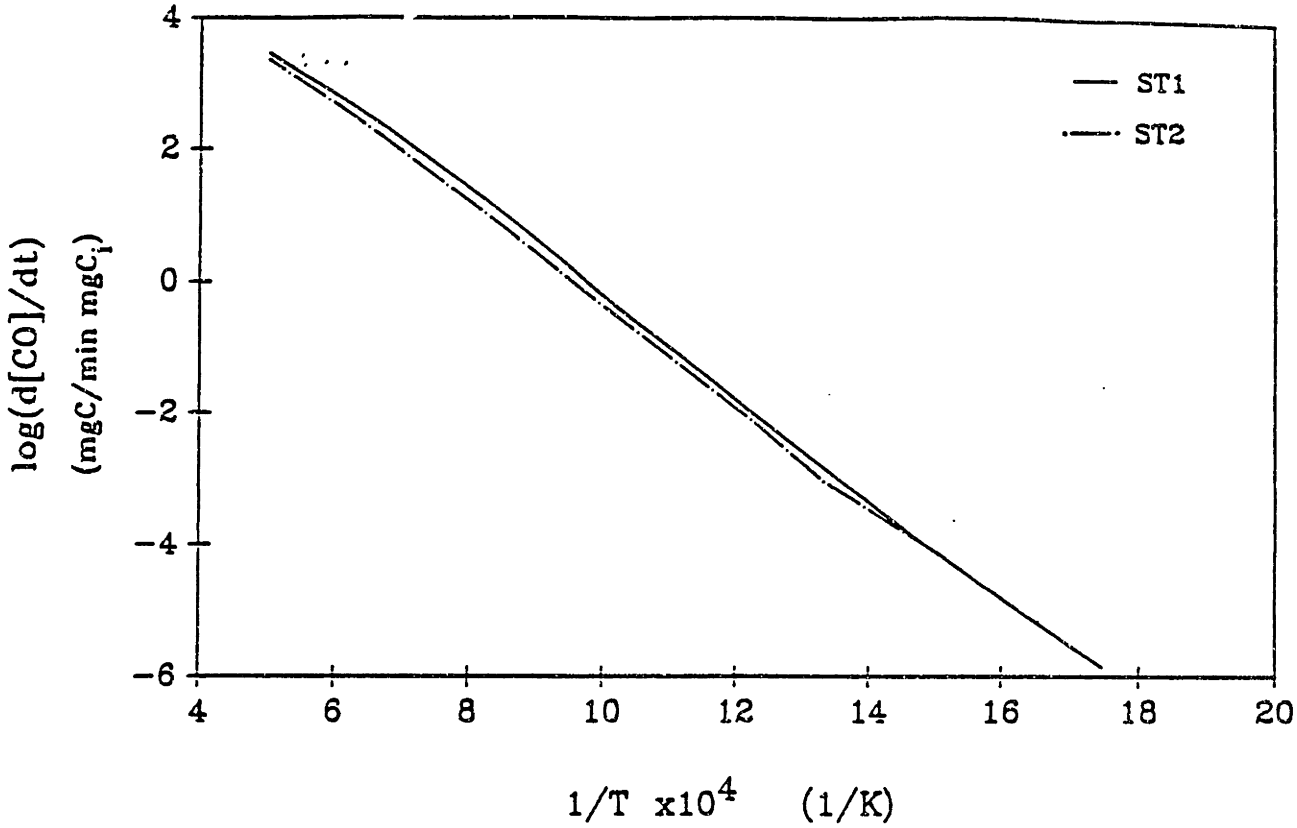

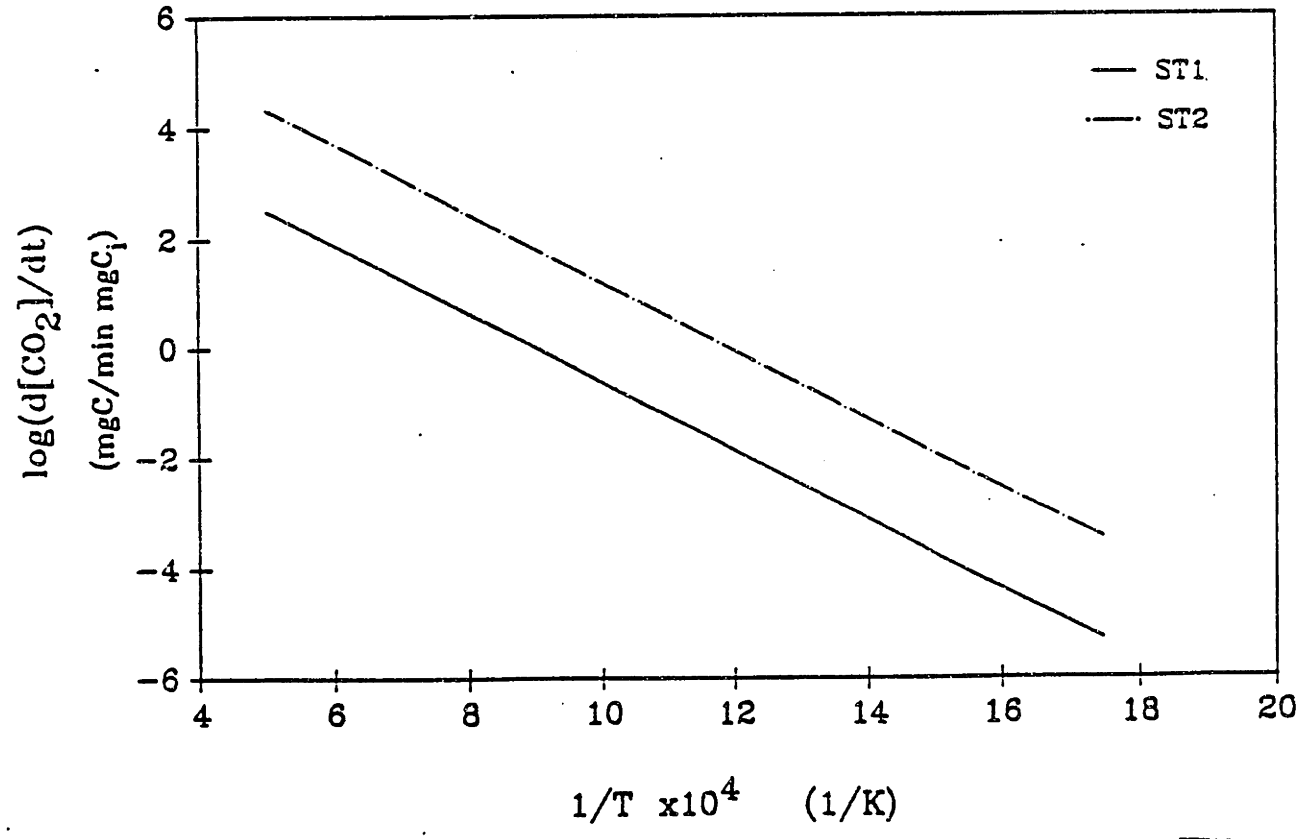

Fig. 5.16 CO and CO_2 rates at 30% conversion as functions of T .
(a) log(d[CO]/dt) vs 1/T (b) log(d[CO_2]/dt) vs 1/T

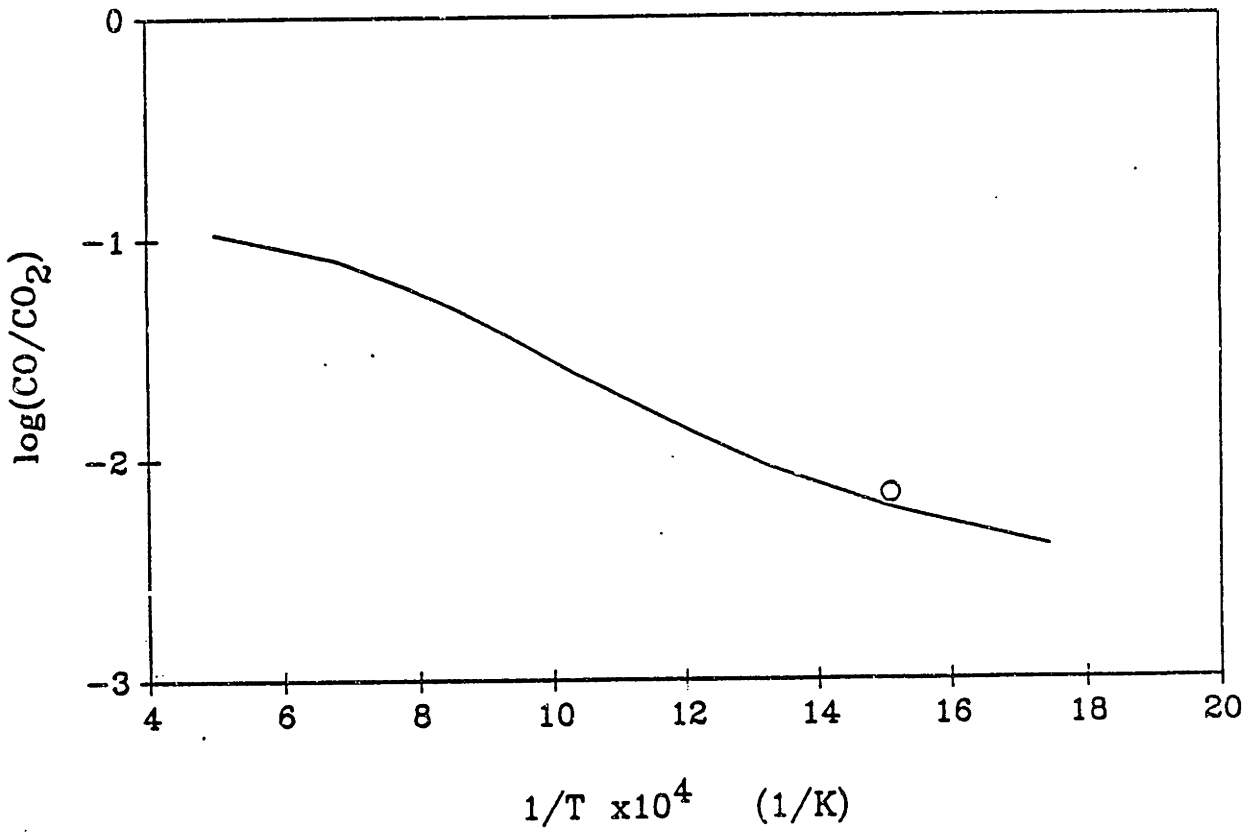

Fig. 5.17 CO/CO_2 ratio at 30% conversion in ST2 oxidation.

Note: Symbol represents experimental data and line represents simulation results from the model.

model simulations are represented by lines and the experiment data are represented by symbols. It can be seen that the present model is able to explain the experimental data for both ST1 and ST2 oxidations, except for the adsorption run at low temperature (see Fig. 5.13), which will be discussed in Section 5.54.

5.5 Discussion (Oxidation Model)

5.51 $\frac{dW_c}{dt}$ vs $\frac{dW}{dt}$

Two types of reaction rate were measured experimentally. The measured rate in TGA system was based on the total weight of the sample (W), which is the summation of the remaining carbon weight (W_c) and the adsorbed oxygen weight (W_o). Therefore,

$$\frac{dW}{dt} = \frac{dW_c}{dt} + \frac{dW_o}{dt}$$

The measured rate from gas analysis in MS was the true carbon reaction rate, based on the conversion of carbon to gaseous products CO and CO_2. These two rates, $\frac{dW}{dt}$ and $\frac{dW_c}{dt}$, were calculated from the present model and compared in Fig.5.11. In addition, the direct measurements of $\frac{dW}{dt}$ and $\frac{dW_c}{dt}$ are given in Fig. 2.3. The difference between them was found very small after a short induction period. So the reaction rate or the reactivity of carbon oxidation will be hereinafter referred to either $\frac{dW}{dt}$ or $\frac{dW_c}{dt}$ without further specification.

5.52 Reaction Order

A fractional reaction order of 0.83 was observed in the ST1 oxidation at 818K (see Fig. 5.6 & Table 5.1). The similar fractional order behavior has been reported by Suuberg et al [30] and Smith [80] for various carbon materials. This fractional order behavior may be explained as the combination of the fractional order of CO rate and the first order of CO_2 rate.

As aforementioned in Section 5.2, the CO formation involves a set of parallel adsorption-desorption processes with different activation energies. The processes with relatively low activation energies are under adsorption control (first order), those with relatively high activation energies are under desorption control (zero order), and the others are of fractional orders (see Fig. 5.14a,b). Therefore, the integration of these parallel processes results in the fractional order behavior for the CO generation. Moreover, as the reaction temperature increases, more processes are shifted to the adsorption control (compare Fig. 5.14 & Fig. 5.15), so the apparent behavior of the CO generation is expected to gradually approach first order.

5.53 Product Ratio CO/CO_2

The observed CO/CO_2 increase with reaction temperature (see Fig.5.5) can be explained by the activation energy difference of CO and CO_2 rates. In general, the apparent activation energy for CO rate is about 35 kcal/mol or higher within 773K — 873K, but the activation energy for CO_2 rate was found to be 28.6 kcal/mol. Since the CO rate has a stronger dependence on temperature than the CO_2 rate, the CO rate will be accelerated faster, and thus CO/CO_2 will increase, as the reaction temperature goes up.

The effect of oxygen partial pressure on CO/CO_2 can be explained by the different reaction orders for CO and CO_2 rates. As discussed in the last section, the CO rate is of the fractional order of 0.77, while the CO_2 rate is of the first order (see also Table 5.1). Consequently, the stronger dependence of the CO_2 rate on oxygen partial pressure leads to the faster acceleration of the CO_2 rate, and thus decreases CO/CO_2, as P_{O_2} increases.

It is interesting to notice that at high oxidation temperature the CO rate approaches to the adsorption control, which is first order and incidentally possesses an apparent activation energy of about 28.4 kcal/mol for the ST1 sample. As a result, no significant difference in reaction order as well as activation energy can be found between the CO and CO_2 rates, so CO/CO_2 will approach a constant during high temperature carbon oxidation. Unfortunately, this phenomenon can not be observed experimentally, because the secondary gas phase reaction at high temperature makes measurement of the heterogeneous product ratio, CO/CO_2, very difficult.

5.54 Adsorption

As pointed out at the end of Section 5.42 the model simulation at low temperature (598K) did not agree with the adsorption experimental data (see Fig. 5.13). First of all, the total amount of oxygen adsorbed on carbon surface at the oxidation temperature (818K) was about 3 times as much as that at the adsorption temperature (598K). Secondly, the initial adsorption rate calculated from the model seemed to be slower than that measured from the adsorption experiment (see also Fig. 5.13). Similar behavior was also found by Lussow et al [81] for oxygen adsorption on Graphon. They reported that the total amount of adsorbed oxygen increased sharply when

the adsorption temperature exceeded 673K, and the ratio of the total amount of oxygen between 773K and 573K was 2.6 to 3.0. They also pointed out that the carbon sites (type I), which could adsorb oxygen at 573K, tends to have a faster adsorption rate comparing with those type II sites which are unable to adsorb oxygen at 573K. And the adsorption rate of the type II sites will become significant after most type I sites are covered.

In light of above discussion, we may reach the following conclusions: (1) Total carbon sites available for oxygen adsorption are higher than those measured at 598K. (2) The adsorption kinetics obtained from the best fit of the experimental data during oxidation may only correspond to the type II sites defined in Lussow's paper [81]. The detailed adsorption kinetics can not be found from the present oxidation model, and future work is needed.

5.55 Effect of Carbon Structure on Oxidation

The present model was employed to examine the effect of carbon structure on the non-catalytic oxidation by comparing the reactivities obtained from different energy distributions.

In light of the discussion in Chapter 4, the energy distribution of a non-catalytic carbon is close to a Gaussian distribution which can be characterized by two parameters, the mean and the standard deviation. It is quite clear that change in the mean of the distribution will significantly alter the reaction rate. It is, however, less obvious that how the standard deviation, or the width of the distribution, affects the reaction rate as well as the apparent activation energy. In this respect, the following model calculation was performed. Suppose that the standard deviation of $f_d(E_d)$,

σ_d, was changed from 7.8 kcal/mol to 3.9 kcal/mol (σ_a in $f_a(E_a)$ would be changed from 1.57 kcal/mol to 0.79 kcal/mol accordingly), and other parameters were kept the same as those for ST1. The reactivities calculated from this narrower distribution were plotted in Fig. 5.18, and compared with the reactivities resulting from the ST1 sample. It was found from Fig. 5.18 that the reactivity dropped about 40 times and the apparent activation energy increased from about 34 kcal/mol to about 53 kcal/mol around 873 K, if the energy distribution for ST1 were narrowed by half. In summary, the apparent activation energy and the reactivity of a non-catalytic carbon oxidation depend on not only the mean but also the standard deviation of the energy distribution of the carbon used. The higher mean and narrower distribution will result in the higher apparent activation energy and lower reactivity. The carbon structure, or the carbon site energy distribution, therefore is a key parameter which controls the reactivity of the non-catalytic carbon oxidation.

Actually, it is the low energy portion of the site energy distribution that sufficiently influences the overall rate in the model calculation, since the other sites with relatively high activation energies correspond to much slower reaction rates comparing with the low activation energy sites, and are considered inactive during the reaction.

The carbon structure is not expected to significantly affect a Ca catalyzed carbon oxidation since the predominant product in this catalytic reaction is CO_2, the rate of which strongly depends on the Ca loading in the carbon. The catalytic effect will overshadow those effects caused by the carbon structure.

5.56 Effect of Ca on the Carbon Oxidation

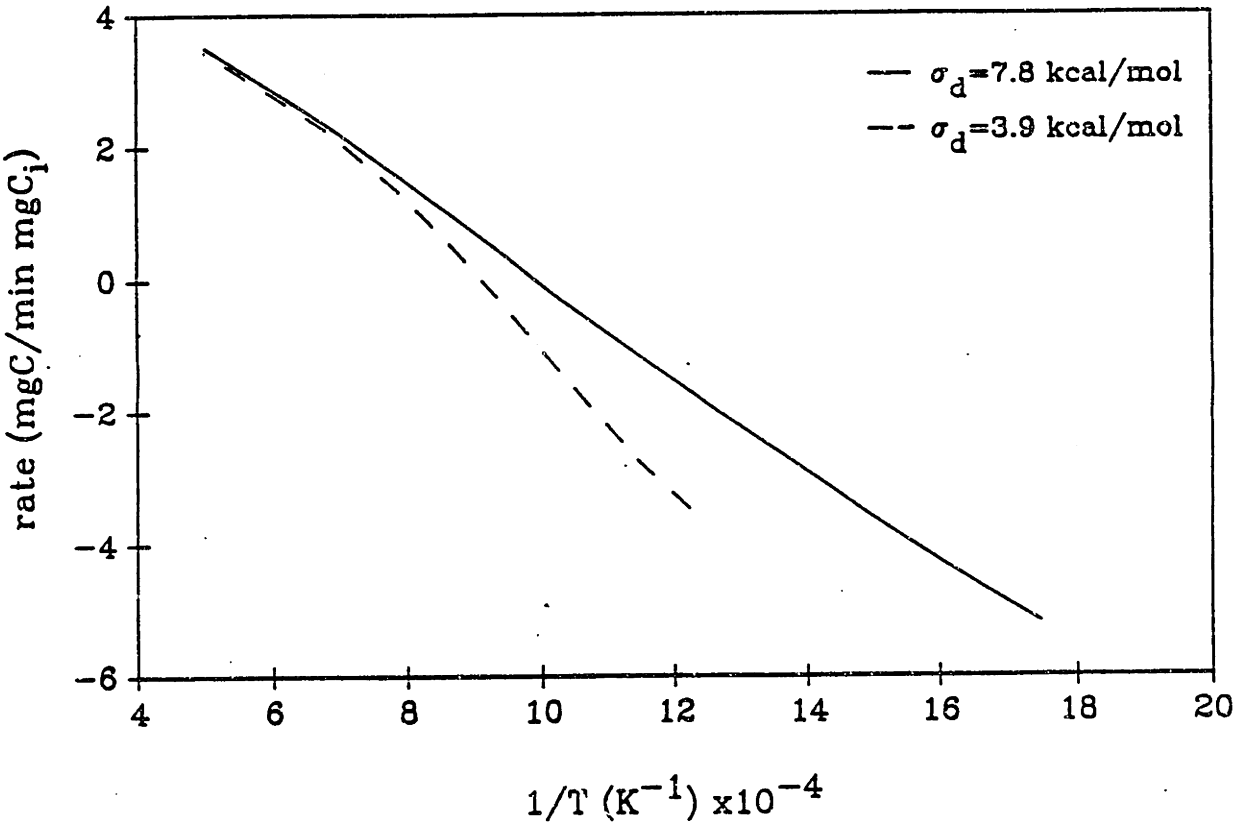

Fig. 5.18 A comparison of reactivities at 30% conversion for the carbon with different energy distributions.

The effect of Ca on the carbon oxidation was studied by comparing the results obtained from the non-catalyzed (ST1) and catalyzed (ST2) carbon samples. It was found from Fig. 5.3 that the overall oxidation rate is significantly catalyzed by Ca. A further study of the individual CO and CO_2 rates in ST2 oxidation indicated that the addition of Ca only catalyzed the CO_2 rate, but has little effect on the CO rate (see Fig. 5.7 & Fig. 5.16). As a result, CO_2 will be generated at a much fast rate than CO, and CO/CO_2 will decrease to a small number (see Fig. 5.17) in the Ca catalyzed carbon oxidation.

The catalytic effect of Ca on the oxidation may be explained as follows: The addition of Ca, on the one hand, generated a second peak on the high energy side of the ST2 energy distribution, and left the original peak virtually unchanged (see Fig. 4.11). According to the preceding discussion in Section 5.55, this change in the energy distribution on the high energy side would not alter the rate of CO formation. The atomic dispersed Ca on the carbon surface, on the other hand, might serve as an active site which is able to effectively oxidize carbon into CO_2. Hence, the increase in the CO_2 rate primarily depends on the amount of Ca added in the carbon sample. In other words, the Ca loading on carbon surface is a key parameter which controls the CO_2 rate, or the overall reaction rate, in the Ca catalyzed carbon oxidation.

Since the addition of Ca only affects the CO_2 rate in the carbon oxidation, CO/CO_2 is a good measure to indicate in what degree the oxidation is catalyzed by Ca. If the ratio is less than 0.1, the carbon oxidation is considered to be significantly catalyzed.

5.6 Summary

The proposed carbon oxidation model is able to explain the experimental results for both ST1 and ST2 oxidations. The model analyses lead to the following conclusions:

1) The controlling factor for a non-catalytic carbon oxidation is the carbon structure which may be appropriately presented by the site energy distribution of that carbon

2) The controlling factor for a Ca catalyzed carbon oxidation is the Ca loading on the carbon surface. The CO/CO_2 ratio provides a measure of the importance of the catalytic effect is in the oxidation.

The proposed oxidation model can be generally applied to other carbon materials. The kinetic parameters required for model simulation can be found using the methodology described in Fig. 5.9.

Both CO and CO_2 are primary products during the carbon oxidation, but they are generated via different mechanisms. The separate examination of the CO and CO_2 formation reveals some new insights about the carbon oxidation.

CO formation was found to follow the conventional adsorption-desorption path which usually has a feature of fractional order with respect to the partial pressure of O_2; while the CO_2 formation was found to be a first order reaction with respect to the partial pressure of O_2. The fractional order for CO formation and the first order for CO_2 formation, therefore, resulted in the observed fractional order of ~ 0.83 for the overall oxidation.

The product ratio, CO/CO_2, was found to increase with increased reaction temperature and with decreased partial pressure of O_2. This behavior is attributed to the stronger temperature dependence (~35 kcal/mol) and weaker O_2 partial pressure dependence (fractional order of

~0.69) for the rate of CO formation, compared with those (~29 kcal/mol and first order, respectively) for the rate of CO_2 formation.

As oxidation temperature increases, the rate of CO formation is expected to approach to adsorption control, which is first order and incidentally possesses an apparent activation energy close to 29 kcal/mol for the ST1 sample. As a result, the CO/CO_2 ratio is expected to gradually approach a constant during high temperature carbon oxidation.

Carbon oxidation can be effectively catalyzed by calcium. An increase of about 50 fold in reactivity around 763K was experimentally observed on a 2 wt% Ca added soot sample, ST2. A further study of the individual CO and CO_2 rates in the ST2 oxidation revealed that the addition of Ca had little effect on the rate of CO formation, and the increase in the overall reactivity was primarily attributed to the increase in the rate of CO_2 formation.

Chapter 6 Conclusions and Recommendations

6.1 Conclusions

6.11 Surface Areas of The ST1 and ST2 Materials

The surface area evolution of ST1 and ST2 during oxidation exhibits the following two features:

1) The specific surface areas of both ST1 and ST2 increase rapidly during the first 20% conversion, due to opening the inaccessible surface area inside the soot particle.

2) The specific surface area will continue to growth or approach an asymptote beyond 20% conversion, depending on the oxidation occurs whether on the entire carbon surface for the ST1 sample, or on those 'catalyzed active sites', which reside on the external surface of the carbon, for the ST2 sample.

6.12 Desorption Model

The desorption model depicted in Chapter 4 can be employed to determine the site energy distribution of a carbon material from measurable TPD experimental data. This energy distribution appropriately characterizes the carbon structure which is found to be an important factor in the non-catalytic carbon oxidation.

Normal and bimodal Gaussian distributions provide good approximations to the real energy distributions of ST1 and ST2, respectively, i.e.,

for ST1 $$f(E) = \frac{1}{\sqrt{2\pi}\,\sigma} \exp\left[-\frac{(E - \bar{E})^2}{2\sigma^2}\right]$$

with $\bar{E} = 69.7$ kcal/mol, $\sigma = 7.81$ kcal/mol;

for ST2 $$f(E) = \frac{1}{\sqrt{2\pi}}\{\frac{0.74}{\sigma_1}\exp[-\frac{(E - \bar{E}_1)^2}{2\sigma_1^2}] + \frac{0.26}{\sigma_2}\exp[-\frac{(E - \bar{E}_2)^2}{2\sigma_2^2}]\}$$

with $\bar{E}_1$ = 67.9 kcal/mol , σ_1 = 7.82 kcal/mol

and $\bar{E}_2$ =79.7 kcal/mol , σ_2 = 3.70 kcal/mol.

6.13 Oxidation Model

The proposed carbon oxidation model is to able explain the experiment results for both ST1 and ST2 samples. The model analyses lead to the following conclusions:

1) The controlling factor for a non-catalytic carbon oxidation is the carbon structure which may be appropriately presented by the site energy distribution of that carbon.

2) The controlling factor for a Ca catalyzed carbon oxidation is the Ca loading on the carbon surface. The CO/CO_2 ratio provides a measure of the importance of the catalytic effect is in the oxidation.

Both CO and CO_2 are primary products during the carbon oxidation, but they are generated via different mechanisms. The separate examination of the CO and CO_2 formation reveals some new insights about the carbon oxidation.

CO formation was found to follow the conventional adsorption-desorption path which usually has a feature of fractional order with respect to the partial pressure of O_2; while the CO_2 formation was found to be a first order reaction with respect to the partial pressure of O_2. The fractional order for CO formation and the first order for CO_2 formation, therefore, resulted in the observed fractional order of ~ 0.83 for the overall oxidation.

The product ratio, CO/CO_2, was found to increase with increased reaction temperature and with decreased partial pressure of O_2. This behavior is attributed to the stronger temperature dependence (~35 kcal/mol) and weaker O_2 partial pressure dependence (fractional order of ~0.69) for the rate of CO formation, compared with those (~29 kcal/mol and first order, respectively) for the rate of CO_2 formation.

Carbon oxidation can be effectively catalyzed by calcium. An increase of about 50 fold in reactivity around 763K was experimentally observed on a 2 wt% Ca added soot sample, ST2. A further study of the individual CO and CO_2 rates in the ST2 oxidation revealed that the addition of Ca had little effect on the rate of CO formation, and the increase in the overall reactivity was primarily attributed to the increase in the rate of CO_2 formation.

6.2 Recommendation for Future Research

The results obtained in this thesis suggest continuing investigations in the following areas:

6.21 Preexponental Factor for the Desorption

The desorption preexponential, $k_{3,0}$, was considered as a parameter in the desorption model (See Chapter 4), and was assumed to be $6x10^{14}$/min in the oxidation model (see Chapter 5). Additional work is needed to determine the exact value of this preexponential. One possible method to obtain $k_{3,0}$ is the heating rate variation technique.

6.22 Site Energy Distribution for Other Carbons

Although the present oxidation model can explain the large differences in reactivity and apparent activation energy for different carbons using the energy distribution, a quantitative understanding of the effect of carbon structure on carbon oxidation requires a systematic study of the relation between different carbons and their site energy distributions. In particular, the site energy distribution for a graphitic material, though it is expected to have a narrower distribution than a disordered amorphous carbon, is needed in order to address the different oxidation behaviors between graphite and amorphous carbons, as a aforementioned in Chapter 1 and Fig. 1.3a,b.

The present oxidation model can be generally applied to simulated the oxidation behaviors for different carbons. The kinetic parameters required for the model simulation can be obtained using the methodology described in Fig. 5.9.

6.23 Detailed Mechanism for CO_2 Formation

In the present oxidation model, a lumped mechanism (R5.4) with a single activation energy is designated for the CO_2 formation during carbon oxidation. This mechanism is justified by the facts that the rate of CO_2 formation was measured to be first order with respect to O_2 partial pressure (see also Table 5.1) and the change in CO_2 rate was found to follow the change of O_2 concentration during transient experiment (see also Section 5.15). However, it is believed that (R5.4) is not an elementary mechanism. A future investigation to pin down detailed mechanism for the CO_2 formation in carbon oxidation will not only be beneficial to the understanding of the entire non-catalytic carbon oxidation, but also reveal some insights about Ca catalyzed carbon

oxidation, for only CO_2 formation during the carbon oxidation can be effectively catalyzed by Ca (see Section 5.16).

6.24 Oxygen Chemisorption on Carbon Surface at Low Temperature

As aforementioned in Section 5.54, the adsorption kinetics obtained from the oxidation temperatures (753K-873K) failed to explain the oxygen chemisorption experiments at low temperature (573K), (see also Fig. 5.13), suggesting that some new features emerge during the low temperature chemisorption of oxygen on carbon. Therefore, future work on the adsorption kinetics is needed in order to better understand the oxygen chemisorption process.

Appendix A. Calculation of Ca Ion Exchange from Solution pH

It is possible to approximately monitor the calcium uptake on the carbon by following the pH of the solution during ion exchange. Calculation of calcium uptake from the pH assumes that no acetate ion is removed from the solution through association with the solid, and that the solid does not contribute to the overall charge balance of the solution. For the acetate ion, the equilibria are:

$$Ca(Ac)_2 \rightleftharpoons Ca^{++} + 2\,Ac^- \qquad (A1)$$

$$H^+ + Ac^- \rightleftharpoons HAc \qquad (A2)$$

From an overall mass balance,

$$[Ac^-] + [HAc] = 2M \qquad (A3)$$

where the brackets denote concentration and M is the molarity of the calcium acetate solution. Utilizing the equilibrium constant for Eq. (A2), we can obtain an expression for the concentration of the acetate ion:

$$[Ac^-] = \frac{2M}{\frac{[H^+]}{K} + 1} \qquad (A4)$$

where K is the equilibrium constant.

The calcium ion concentration can then be determined from a charge balance:

$$[Ca^{++}] = \frac{1}{2}\left([Ac^-] - [H^+]\right)$$

$$= \frac{M}{\frac{[H^+]}{K} + 1} - \frac{1}{2}[H^+] \qquad (A5)$$

Appendix B. Calculation of Intra-particle Diffusion

Effects of intra-particle diffusion in the soot sample, ST1, were determined by so-called Weisz-Prater criterion described in [82], using a first order reaction-diffusion model. By definition [82],

$$\Phi \equiv \eta\phi = \frac{r_{obs}L^2}{D_{eff}C_s} \tag{B1}$$

where η — effectiveness factor.

ϕ — Thiele modulus.

r_{obs} — observed reaction rate (mol/cm^3 s).

L — characteristic length of the particle.

C — gas phase concentration at solid surface.

According to Froment and Bischoff [82], there are no diffusion limitations, if

$$\Phi \ll 1 \tag{B2}$$

Two types of intra-particle diffusion were considered in the calculation: (1) the pore diffusion in the agglomerant particle; and (2) the micropore diffusion in the individual primary particle.

B1. Pore Diffusion in the Agglomerant Particle

It can be seen from the TEM picture (Fig. 2.1) that the ST1 sample is aggregated by up to several hundreds of pseudo spherical primary particles, the diameter of which is around 43 nm. The particle size of such an agglomerate is on the order of 1 μm (see Fig. 2.1); and pore size in the agglomerate was estimated according to the diameter of the primary particle; i.e.,

$$L_{agg} \sim 1\ \mu m = 10^{-4}\ cm$$

$$r_{agg} \sim d_p/2 \approx 21.5\ nm = 2.15 \times 10^{-6}\ cm$$

This pore size falls into Kundsen diffusion regime [82]. So, for T=873K,

$$D_{K,O_2} = 9700\, r_{agg} \sqrt{\frac{T}{M}} \approx 0.11\ cm^2/s$$

$$D_{eff} \approx \frac{\varepsilon}{\tau_s} D_{K,O_2} \approx 0.012\ cm^2/s$$

where ε and τ_s are the porosity and tortuosity of the solid, and assumed to be 0.34 and 3, respectively.

For a conservative estimate, the reaction rate at T=873K and P_{O_2}=0.10 atm were used to calculate Φ. From Fig. 5.3,

$$r_{obs} \approx 0.1\ (mgC/min\ mgC_i) \approx 2.8 \times 10^{-4}\ (mol/cm^3\ s)$$

where $\rho_s = 2.0\ g/cm^3$ was used.

$$C_s = 0.1\ atm \approx 1.4 \times 10\ (mol/cm^3), \quad \text{at T=873K.}$$

Thus,

$$\Phi_{agg} \equiv \frac{r_{obs} L_{agg}^2}{D_{eff} C_s} \approx \frac{2.8 \times 10^{-4} \times (10^{-4})^2}{0.012 \times 1.4 \times 10^{-6}} \approx 1.7 \times 10^{-4} \ll 1$$

No pore diffusion limitations exist in the agglomerant particle.

B2. Micropore Diffusion in the Primary Particle

For a single primary particle [82],

$$L_p \sim d_p/6 \approx 7.2\ nm = 7.2 \times 10^{-7}\ cm$$

$$r = \frac{2\varepsilon}{\rho_s S_A} \approx \frac{2 \times 0.34}{2.0 \times 710.6 \times 10^4} \approx 4.8 \times 10^{-8}\ cm$$

$$D_{K,O_2} = 9700\, r_p \sqrt{\frac{T}{M}} \approx 2.4 \times 10^{-3}\ cm^2/s$$

$$D_{eff} \approx \frac{\varepsilon}{\tau_s} D_{K,O_2} \approx 2.8 \times 10^{-4}\ cm^2/s$$

Again, take $r_{obs} \approx 2.8 \times 10^{-4}$ $(mol/cm^3\ s)$ and $C_s \approx 1.4 \times 10^{-6}$ (mol/cm^3),

$$\Phi_p \equiv \frac{r_{obs} L_p^2}{D_{eff} C_s} \approx \frac{2.8 \times 10^{-4} \times (7.2 \times 10^{-7})^2}{2.8 \times 10^{-4} \times 1.4 \times 10^{-6}} \approx 3.7 \times 10^{-7} \ll 1$$

Therefore, effect of the micropore diffusion in the primary ST1 particle is negligible.

Appendix C. Leading Behavior of the Function G(E,t)

As defined in Eq.(4.10),

$$G(E,t) \equiv \int_0^t exp(-\frac{E}{RT_i}\frac{T_i}{T(\xi)})d\xi \qquad (4.10)$$

Noting that for the E range of interest the quantity E/RT_i is very large, we can obtain an asymptotic expression for G(E,t) using Laplace's method [78].

Since $T'(t) > 0$, for $0 \le t \le t_f$

So,
$$G(E,t) \equiv \int_0^t exp(-\frac{E}{RT_i}\frac{T_i}{T(\xi)})d\xi$$

$$\sim \int_{t-\varepsilon}^t exp(-\frac{E}{RT_i}\frac{T_i}{T(\xi)})d\xi$$

$$\sim \int_{t-\varepsilon}^t exp[-\frac{E}{RT_i}(\frac{T_i}{T(t)} - \frac{T_i}{T^2(t)}T'(t)(\xi-t) + \dots)]d\xi$$

$$\sim \int_{-\infty}^t exp(-\frac{E}{RT(t)})exp[-\frac{ET'(t)}{RT^2(t)}(t-\xi)]d\xi$$

$$= \frac{RT^2(t)}{ET'(t)} exp(-\frac{E}{RT(t)})$$

By the same token, if $T > T_f$

$$G(E,t) \equiv \int_0^{t_f} exp(-\frac{E}{RT_i}\frac{T_i}{T(\xi)})d\xi + \int_{t_f}^t exp(-\frac{E}{RT_i}\frac{T_i}{T(\xi)})d\xi$$

$$\sim \frac{RT^2(t_f)}{ET'(t_f)} exp(-\frac{E}{RT_f}) + (t - t_f)\, exp(-\frac{E}{RT_f})$$

Therefore,

$$G(E,t) \approx \begin{cases} \dfrac{RT^2(t)}{ET'(t)} \exp(-\dfrac{E}{RT(t)}) & 0 \le t \le t_f \\ [\dfrac{RT_f^2}{ET_f'} + (t - t_f)] \exp(-\dfrac{E}{RT_f}) & t > t_f \end{cases} \qquad \text{(C1)}$$

Moreover, the partial derivative of G(E,t) with respect to E can be calculated in the same way:

$$\frac{\partial G}{\partial E} = \int_0^t -\frac{1}{RT(\xi)} \exp(-\frac{E}{RT_i}\frac{T_i}{T(\xi)}) d\xi$$

$$\sim \begin{cases} -\dfrac{1}{RT(t)}\dfrac{RT^2(t)}{ET'(t)} \exp(-\dfrac{E}{RT(t)}) & 0 \le t \le t_f \\ -\dfrac{1}{RT_f}[\dfrac{RT_f^2}{ET_f'} + (t - t_f)] \exp(-\dfrac{E}{RT_f}) & t > t_f \end{cases}$$

$$\sim -\frac{1}{RT(t)} G(E,t) \qquad \forall\, t \qquad \text{(C2)}$$

From the definition of g(E,t) and G(E,t),

$$g(E,t) \equiv \exp(-k_o G(E,t))$$

So,

$$\frac{\partial g}{\partial E} = -k_o g(E,t) \frac{\partial G}{\partial E}$$

$$\sim \frac{k_o}{RT(t)} g(E,t)\, G(E,t) \qquad \text{(C3)}$$

Appendix D. Asymptotic Solution to Equation (4.12a)

We rewrite here Eq.(4.12a) as

$$\ln(y) + y = \ln(k_o \frac{T(t)}{T'(t)}) \equiv a \tag{D1}$$

Since a is usually a large number, the dominant balance in Eq.(D1) is y~a. So, we introduce a parameter 'ε' in Eq.(D1), such that

$$\varepsilon \ln(y) + y = a \tag{D2}$$

and let the solution of Eq.(D2) have an asymptotic form:

$$y = y_o + \varepsilon y_1 + \varepsilon^2 y_2 + \ldots \tag{D3}$$

Thus,

$$\begin{aligned} \ln(y) &= \ln\{ y_o(1 + \varepsilon\frac{y_1}{y_o} + \varepsilon^2\frac{y_2}{y_o} + \ldots)\} \\ &= \ln(y_o) + \ln\{ 1 + (\varepsilon\frac{y_1}{y_o} + \varepsilon^2\frac{y_2}{y_o} + \ldots)\} \\ &\approx \ln(y_o) + (\varepsilon\frac{y_1}{y_o} + \varepsilon^2\frac{y_2}{y_o} + \ldots) - \frac{1}{2}(\varepsilon\frac{y_1}{y_o} + \varepsilon^2\frac{y_2}{y_o} + \ldots)^2 \\ &\quad + \frac{1}{3}(\varepsilon\frac{y_1}{y_o} + \ldots)^3 + \ldots \end{aligned} \tag{D4}$$

Plugging Eq's (D3) and (D4) into Eq.(D2), and collecting the terms with the same power of ε, we have

- for the zero order of ε: $y_o = a$
- for the 1st order of ε: $\ln(y_o) + y_1 = 0$

$$y_1 = -\ln(y_o) = -\ln(a)$$

- for the 2nd order of ε: $\frac{y_1}{y_o} + y_2 = 0$

$$y_2 = \frac{\ln(a)}{a}$$

- for the 3rd order of ε: $\frac{y_2}{y_o} - \frac{1}{2}(\frac{y_1}{y_o})^2 + y_3 = 0$

$$y_3 = \frac{\ln(a)}{2a^2}(\ln(a) - 2)$$

.....

Finally, substituting all these y's into Eq.(D3) and setting $\epsilon = 1$, we obtain the asymptotic solution to Eq.(D1):

$$y \approx a - \ln(a) + \frac{\ln(a)}{a} + \frac{\ln(a)}{2a^2}\,(\ln(a) - 2) \qquad \text{(D5)}$$

The error of this asymptotic solution results from the truncation of Eq.(D3) at y_4, which is on the order of $(\frac{\ln(a)}{a})^3$.

Appendix E. Experimental Report

To: A.F. Sarofim, J.P. Longwell & C.A. Mims

From: Zhiyou Du

Date: Aug. 5, 1988

Re: Transient Experiment in EXXON

Experimenter: C.A. Mims, Gary & Z. Du

E1. Objective

E1.1 Measure "active" sites on the soot under oxidation condition, using transient as well as isotope techniques.

E1.2 Test some possible mechanisms of carbon oxidation by transient technique.

E2. Experiment

The whole experimental set-up is shown in Fig. 1. The soot sample was preheated up to 1173K in Ar, and was reacted with $O_2^{16\text{-}16}$ to about 20% conversion; then time was set to t = 0 and reactant was switched from Ar + $O_2^{16\text{-}16}$ mixture to Ar + $O_2^{18\text{-}18}$ mixture. The gas product in this transient process will either go to MS directly (MS experiment) or pass through GC first, then go to MS (GS-MS experiment). Finally, CO and CO_2 concentrations in the product stream. as a function of time, can be obtained from the MS output.

E2.1 MS Experiment

In the MS experiment, the gas product is directly sampled and analyzed by to give the time evolutions of CO and CO_2 from contaminations of filament oxidation in MS chamber (see section E3.1).

E2.2 GC-MS Experiment

In the GC-MS experiment, the gas sample was first separated by GC column in the order of O_2 (1.8 min.), CO (2.7min.) and CO_2 (7.7min.), and then analyzed by MS. The advantage of this method is that any CO_2 generated during the filament oxidation could be distinguished from the CO_2 in the gas sample. (The same statement can not be made for CO, because O_2 and CO peaks are too close in GC. These peaks, however, can be further separated by changing either GC column or temperature control program.). There are two drawbacks in GC-MS method. First, it takes much longer time than MS method to finish the analysis for one gas sample; secondly, it can only take a few gas sample (up to 15) during one transient process.

E3. Results and Discussion

E3.1 Blank Run

Three series of blank runs were conducted in order to understand the features of background signals. Under conditions of all the blank runs, reactor was empty and kept at room temperature. The results of those blank runs are tabulated in Table 1.

From Table 1a and 1b, one can see that the ratio of mass 46 to mass 48 changes from originally 1:10 to 1:3, if some $O_2^{16\text{-}16}$ exists in the

mixture. This indicates clearly that scrambling of O^{16} and O^{18} is significant under our experiment condition. The scrambling may follow mechanisms, such as

$$O^{16} + CO_2^{18\text{-}18} \rightleftharpoons O^{18} + CO_2^{16\text{-}18}$$

and

$$O^{18} + CO_2^{16\text{-}16} \rightleftharpoons O^{16} + CO_2^{16\text{-}18}$$

It is the oxygen scrambling that gives us headaches during the experiment. We still do not know how to get around with this problem right now.

Table 1b also shows that some CO and CO_2, 1.74 & 1.46 units respectively, are generated by oxidation of MS filament. These amounts are large enough to effect the data in MS experiment.

$CO_2^{16\text{-}16}$ impurity (0.393 unit) was found in our Ar + $O_2^{18\text{-}18}$ gas cylinder (see Table 1c.).

E3.2 Transient Experiment

As mentioned above, the artifacts of CO and CO_2 in MS chamber can significantly contaminate MS signals. The results from MS experiment are, therefore, not very useful, and will not be presented here.

Results from GC-MS transient experiment are presented in Fig. 2 and Table 2 (The CO_2 generated in MS chamber is excluded.). The only meaningful observation is that the change in CO_2 concentration follows the change of O_2 in the transient process, which infers that CO_2 production in carbon oxidation process is not due to the desorption of carbon oxygen complex on the carbon surface, rather than directly

reacting with O_2. This behavior suggests some possible routes to produce CO_2 as following:

$$C + O_2 \longrightarrow (C\text{-}O_2)^* \xrightarrow{fast} CO_2$$

or $$C + (C\text{-}O) + O_2 \longrightarrow (C\text{-}O) + CO_2$$

E4. Conclusion

E4.1 CO_2 production in oxidation process is directly related to the O_2 partial pressure.

E4.2 Two kinds of artifacts existed in our experiment: one is the scrambling of oxygen isotopes; the other is the oxidation of MS filament.

E4.3 Oxygen isotope technique can not be employed in our experiment, unless the scrambling problem could be avoided in some smart manner.

Table 1. The Results from Blank Runs

1a) CO_2^{18-18} only

	due to O_2	due to CO_2
mass 28	0.0	0.482
mass 30	0.0	4.33
mass 44	0.0	0.302
mass 46	0.0	5.66
mass 48	0.0	49.2

1b) Ar(80%)+O_2^{16-16}(20%)+CO_2^{18-18}(trace)

	due to O_2	due to CO_2
mass 28	1.74	0.0
mass 30	0.103	0.089
mass 44	1.46	0.0
mass 46	0.0	0.304
mass 48	0.0	0.938

1c) Ar(80%)+O_2^{18-18}(20%)

	due to O_2	due to CO_2
mass 28	2.05	0.0
mass 30	2.63	0.0
mass 44	0.390	0.393
mass 46	0.367	0.036
mass 48	0.066	0.0

Table 2. The Results from GC-MS Transient Experiment

t(sec)	mass16	mass18	mass28	mass30	mass44	mass46	mass48
-10	29.4	1.37	7.51	0.238	6.93	0.0	0.0
-5	25.1	0.473	6.48	0.201	4.31	0.0	0.0
2	22.0	1.43	6.01	0.465	3.23	0.089	0.0
4	1.17	15.4	4.35	3.69	1.31	1.27	0.799
6	0.485	15.5	3.90	3.77	0.828	1.06	0.805
8	0.388	12.8	3.81	3.41	0.767	1.18	0.998
11	0.422	15.3	3.85	3.56	0.837	1.14	0.770
16	0.524	16.6	4.25	3.95	0.800	1.16	0.945
30	0.381	16.4	3.92	4.18	0.606	0.811	0.584
60	0.534	15.8	3.98	4.06	1.10	0.689	0.372
100	0.379	15.2	3.41	4.18	0.656	0.809	0.640
200	0.476	13.3	3.38	4.13	0.590	0.769	0.710

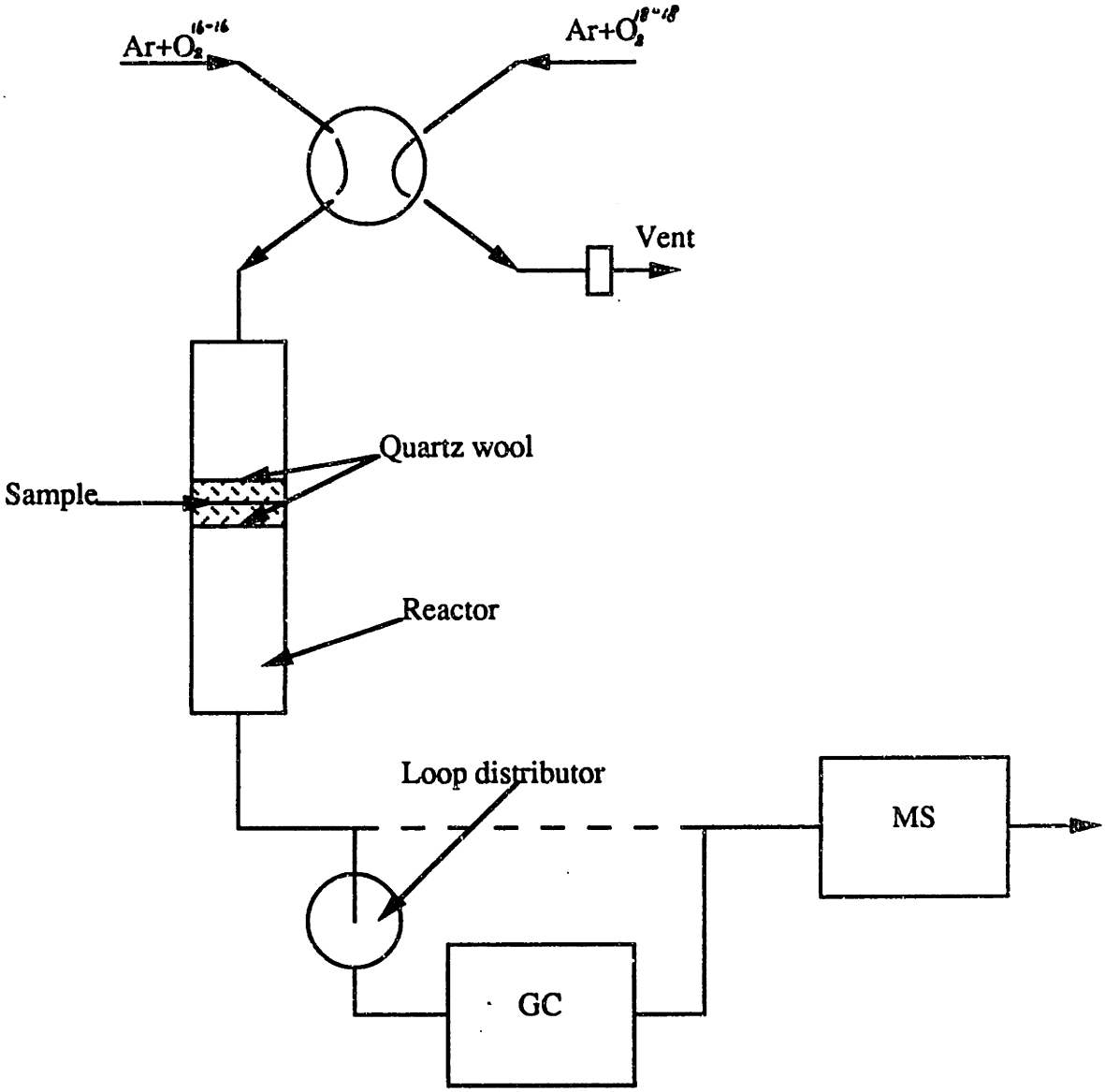

Fig. 1. Experimental set-up

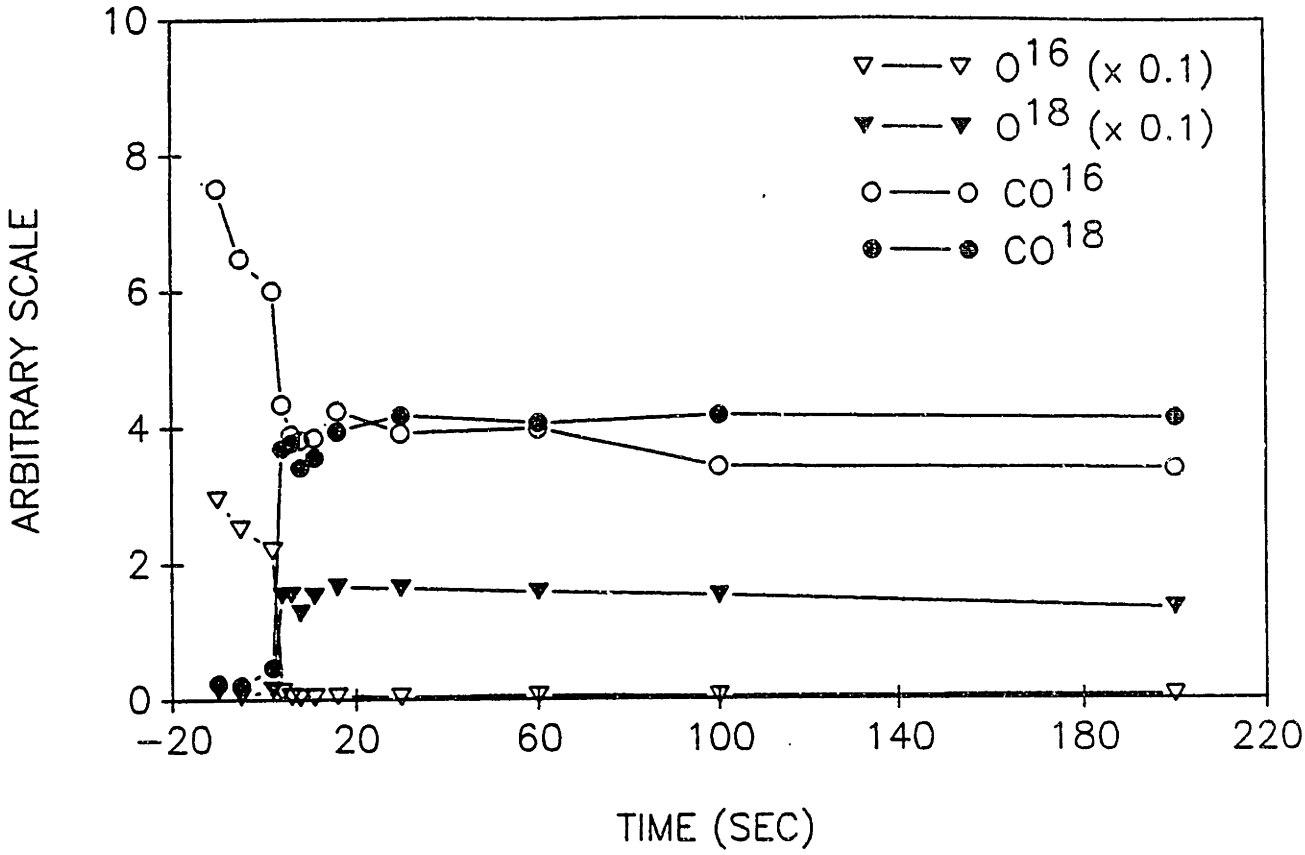

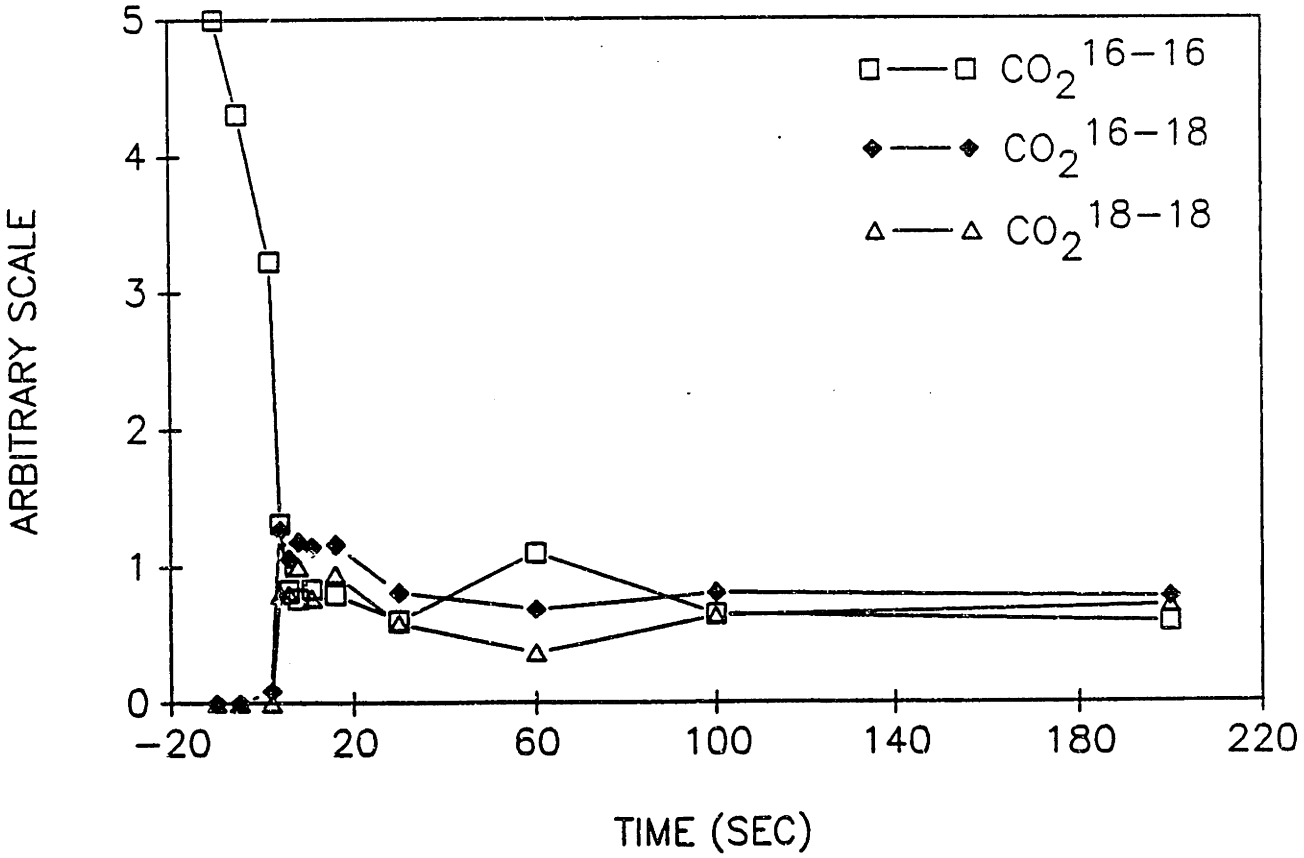

Fig.2. Time Evolution of CO and CO_2 in Transient Process

```
CCCCCCCCCCCCCCCCCCCCCCCCCCCCCCCCCCCCCCCCCCCCCCCCCCCCCCCCCCCCCCCCCCCCCCCCCCCCCCC
C                                                                              C
C     Appendix F.  Fortran Programs                                            C
C                                                                              C
CCCCCCCCCCCCCCCCCCCCCCCCCCCCCCCCCCCCCCCCCCCCCCCCCCCCCCCCCCCCCCCCCCCCCCCCCCCCCCC
C
C
C     F1. Simulation of reaction process
C
C     A atandard Fortran software package D02EBF from Neg Lib. is employed in
C     this program to solve a system of equations, Eq.'s (5.12) to (5.16); and
C     then to calculate carbon weight, product ratio, reactivity etc. as a
C     function of reacton time.
C
C     A more detailed description about the subroutine D02EBF can be found in
C     Neg Lib. user's manual available on the MIT/Athena network.
C
C     NOTE: The parameter b3 used in this program corresponds to b4 defined in
C           Chapter 5 of this thesis.
C
C
C
      implicit double precision (a-h,o-z)
      integer i,j,ifail,ir,iw,mped,n
      dimension w(2825),y(47),c0(23,5),c1(23,5)
      external fcn,out,pederv,int1
      common i,xend,dx,b2,b3,b1,si,sid,sa,dys,
     1     ct0,ct1,ct2,dco,c0,c1,xni,ak4
C
      open(1,file='rex.mat')
      open(2,file='rexe.mat')
      print*, 'xend,dx,1='
      read*, xend,dx,1
      print*, 'ak4,b2,b3,b1,si,sid,sa='
      read*, ak4,b2,b3,b1,si,sid,sa
C
      print*,'t','ratio','ww'
      dys=0.4d0
      x=0.0d0
      n=47
      iw=2825
      mped=0
      ir=0
      tol=10.**(-1)
      print*,'tol=',tol
      do 4 j=1,n
4        y(j)=0.0d0
      i=1
      ifail=0
      call d02ebf(x,xend,n,y,tol,ir,fcn,mped,pederv,
     1     out,w,iw,ifail)
      print*,'ifail=',ifail
      if(tol.lt.0.0) print*,'range too short for tol.'
C
      close(unit=1)
      close(unit=2)
```

```
      stop
      end
C
C
      subroutine fcn(t,y,f)
      implicit double precision (a-h,o-z)
      dimension f(47),y(47),c0(23,5),c1(23,5),cc0(23)
      common i,xend,dx,b2,b3,b1,si,sid,sa,dys,
     1     ct0,ct1,ct2,dco,c0,c1,xni,ak4
C
      ga(x)=sa*(1.0+2.638*
     1     (1.-exp(-4.253*x)))*(1.-x)
      dga(x)=sa*(11.22*exp(-4.253*x)*(1.-x)-
     1     (1.0+2.638*(1.-exp(-4.253*x))))
C
      call int1(y,dys,sid,ct1,ct2,dco)
      ct0=1.0d0-ct1-ct2
      do 50 j=1,23
         ys=(j-1)*dys-4.8d0
         cc0(j)=1.0d0-y(j)-y(j+23)
         f(j)=-y(j)*dga(y(47))*(b3+dco)
     1        +(ct0*y(j+23)+cc0(j)*ct2)/b2-
     2        exp(-(ys+0.5*sid)*sid)*y(j)
         f(j+23)=-y(j+23)*dga(y(47))*(b3+dco)
     1        +b1*exp(-ys*si)*cc0(j)-(ct0/b2)
     2        *y(j+23)
 50      continue
      f(47)=ga(y(47))*(b3+dco)
      return
      end
C
C
      subroutine pederv(x,y,pw)
      return
      end
C
C
      subroutine out(x,y)
      implicit double precision (a-h,o-z)
      dimension y(47),c0(23,5),c1(23,5)
      common i,xend,dx,b2,b3,b1,si,sid,sa,dys,
     1     ct0,ct1,ct2,dco,c0,c1,xni,ak4
C
      ga(x)=sa*(1.0+2.638*
     1     (1.-exp(-4.253*x)))*(1.-x)
C
      call int1(y,dys,sid,ct1,ct2,dco)
      ct0=1.0d0-ct1-ct2
      ww=16./12.*(1.0+ct2-ct0)*ga(y(47))
     1     +(1.0d0-y(47))
      t=x/ak4
 5    ratio=dco/b3
 10   dc=ga(y(47))*(b3+dco)
      call int2(y,dys,si,ads)
      dw=(32.d0*b1*ads-12.d0*b3-28.d0*dco)
     1     *ga(y(47))/(-12.d0)
```

```
      if(i.gt.6) goto 30
      print*, t,ratio,ww
      write(1,110) t,y(47),ratio,ww,dc,dw
      write(2,120) dco,1.0d0
      i=i+1
      x=(float(i-1)*dx)
 40   return
 110  format(1x,f8.3,5e13.4)
 120  format(1x,2e16.6)
      end
C
C     Integration by Simpson's Formula (n=2)
C
      subroutine int1(a1,ds,sid,s1,s2,dco)
      implicit double precision (a-h,o-z)
      dimension a1(47),b(47)
      f(x)=exp(-x*x/2.0)/2.50662
      g(x)=exp(-(x+sid)**2/2.0)/2.50662
C
      s1=0.0d0
      s2=0.0d0
      dco=0.0d0
      do 5 i=1,23
         b(i)=a1(i)*f((i-1)*ds-4.8d0)
         b(i+23)=a1(i+23)*f((i-1)*ds-4.8d0)
 5       continue
C
      do 20 i=1,21,2
         s1=s1+ds/3.*(b(i)+4.*b(i+1)+b(i+2))
         s2=s2+ds/3.*(b(i+23)+4.*b(i+24)+b(i+25))
 20      continue
      do 10 i=1,23
 10      b(i)=a1(i)*g((i-1)*ds-4.8d0)
      do 30 i=1,21,2
         dco=dco+ds/3.*(b(i)+4.*b(i+1)+b(i+2))
 30      continue
      return
      end
C
C
      subroutine int2(a1,ds,si,ads)
      implicit double precision (a-h,o-z)
      dimension a1(47),b(47)
      g(x)=exp((si*si-(x+si)**2)/2.0)/2.50662
C
      ads=0.0d0
      do 10 i=1,23
 10      b(i)=(1.d0-a1(i)-a1(i+23))*g((i-1)*ds-4.8d0)
      do 30 i=1,21,2
         ads=ads+ds/3.*(b(i)+4.*b(i+1)+b(i+2))
 30      continue
      return
      end
```

```
C
C
C     F2.  Fitting Subroutine
C
C
C     This program is to minimize a nonlinear function f(x1,x2,...,xn), using
C     Simplex Downhill Method.  Only the values of f(X), not the derivatives
C     of f(X), are required in the program.
C
      subroutine flesim(x,fx,n,ft,step,it,imos,icovg)
      dimension x(n),a(10,10),f(10)
C
      if(it.eq.1) go to 87
      ft=0.000001
 87   iter=0
      nf=0
      alpha=1.0
      beta=0.5
      gama=2.0
      vn=float(n)
      k1=n+1
      k2=n+2
      k3=n+3
      k4=n+4
C
C     construct initial Simplex
C
      d1=step/vn/sqrt(2.0)*(sqrt(vn+1.)+vn-1.)
      d2=step/vn/sqrt(2.0)*(sqrt(vn+1.)-1)
      do 1 j=1,n
 1       a(1,j)=x(j)
      do 2 i=2,k1
         do 3 j=1,n
 3          a(i,j)=d2+x(j)
         l=i-1
 2       a(i,l)=d1+x(l)
      do 10 i=1,k1
         do 11 j=1,n
 11         x(j)=a(i,j)
         call obf(x,f(i))
         nf=nf+1
 10      continue
 86   if(iter.eq.imos) go to 85
      iter=iter+1
C
C     select the Max of f(X)
C
      fh=f(1)
      ih=1
      do 20 i=2,k1
         if(f(i).le.fh) go to 20
         fh=f(i)
         ih=i
 20      continue
C
C     select the Min of f(X)
```

```
C
      fl=f(1)
      il=1
      do 30 i=2,k1
         if(fl.le.f(i)) go to 30
         fl=f(i)
         il=i
 30      continue
C
C     calculate the centroid of the Simplex except Max f(X)
C
      do 40 j=1,n
         s=0.0
         do 41 i=1,k1
 41         s=s+a(i,j)
         a(k2,j)=1./vn*(s-a(ih,j))
C
C     calculate the reflection of the max f(X) through the center of weight
C
         a(k3,j)=(1.0+alpha)*a(k2,j)-alpha*a(ih,j)
 40      x(j)=a(k3,j)
      call obf(x,f(k3))
      nf=nf+1
      if(f(k3).lt.fl) go to 60
C
C     calculate the 2nd largest f(X)
C
      if(ih.eq.1) go to 51
      fs=f(1)
      go to 52
 51   fs=f(2)
 52   do 53 i=1,k1
         if(ih.eq.i) go to 53
         if(f(i).le.fs) go to 53
         fs=f(i)
 53      continue
      if(f(k3).gt.fs) go to 54
      go to 55
C
C     expansion, if new Min f(X) occurs due to the reflection
C
 60   do 61 j=1,n
         a(k4,j)=(1.-gama)*a(k2,j)+gama*a(k3,j)
 61      x(j)=a(k4,j)
      call obf(x,f(k4))
      nf=nf+1
      if(f(k4).lt.fl) go to 66
      go to 55
C
C     compression, if the new f(X) due to the reflection > 2nd largest F(X)
C
 54   if(f(k3).gt.fh) go to 57
C      do 58 j=1,n
C 58      a(ih,j)=a(k3,j)
      do 59 j=1,n
         a(k4,j)=beta*a(ih,j)+(1.-beta)*a(k2,j)
```

```
 59       x(j)=a(k4,j)
          call obf(x,f(k4))
          nf=nf+1
          if(fh.gt.f(k4)) go to 66
C
C         contraction, if the new f(X) due to the reflection > Max f(X)
C
 57       do 90 j=1,n
             do 90 i=1,k1
 90          a(i,j)=0.5*(a(i,j)+a(il,j))
          do 91 i=1,k1
             do 62 j=1,n
 62             x(j)=a(i,j)
             call obf(x,f(i))
 91          nf=nf+1
          go to 86
 66       do 67 j=1,n
 67          a(ih,j)=a(k4,j)
          f(ih)=f(k4)
          go to 76
 55       do 80 j=1,n
 80          a(ih,j)=a(k3,j)
          f(ih)=f(k3)
 76       do 73 j=1,n
 73          x(j)=a(k2,j)
          call obf(x,f(k2))
          nf=nf+1
          difer=0.0
          do 74 i=1,k1
 74          difer=difer+(f(i)-f(k2))**2
          difer=sqrt(difer/(vn+1.))
          if(difer.ge.ft) go to 86
          fx=f(k2)
          icovg=1
          go to 88
 85       icovg=-1
 88       print*,'nf=',nf
          return
          end
C
C         test f(X) subroutine
C
C          subroutine obf(x,fx)
C          dimension x(2)
C
C          fx=(x(1)+10.*x(2))**2+5.*(x(3)-x(4))**2
C         1   +(x(2)-2.*x(3))**4+10.*(x(1)-x(4))**4
C          fx=100.*(x(2)-x(1)*x(1))**2+(1.-x(1))**2
C          return
C          end
```

Reference

1. Von Fredersdorf C.G. and M. A. Elliott in "Chemistry of Coal Utilization" Supplemental Volume, (H.H. Lowry ed.) John Wiley and Sons Inc. N.Y. p.969 (1963)

2. Hottel H.C. and Howard J.B., "New Energy Technology," MIT Press, Cambridge, MA pp.18-21 (1971)

3. Essenhigh R.H., Chapter 19 in " Chemistry of Coal Utilization" Second Supp. Vol. (M.A. Elliott, ed) John Wiley and Sons Inc. N.Y. (1981)

4. Laurendeau N.M., Progress in Energy and Combustion Science 4 221 (1978)

5. Smith I.W., Nineteenth Symposium (International) on Combustion Institute, 1045 (1982)

6. Mckee, D.W., "The Catalyzed Gasification Reaction of Carbon" in Chemstty and Physics of Carbon, P.L. Walder, Jr. (editor), Vol. 16, 1 Marcel Dekker, New York (1981)

7. Oberlin A., Carbon 22 No. 6 521 (1984)

8. Spiro, C. L., D.W. Mckee, P.G. Kosky, and E.J. Lamby, Fuel 62 180 (1983)

9 Franklin, R.E., Roy. Soc. of London Proc. Ser. A, 209 196(1951)

10 Warren B.E., Phys. Review 59 9 693 (1941)

11 Franklin R.E., Acta Cryst. 3 107 (1950)

12 Cartz L. and P.B. Hirsch, Phil. Rransactions 252 68 (1959)

13 Short M.A. and P.L. Walker Jr., CArbon 1 3 (1963)

14 March H. and H.P. Stakler, Fuel 46 351 (1967)

15 Simons G.A. and M.L. Finson, Comb. Sci. and Tech. 19 217 (1979)

16. Goma, J. and M. Oberlin, Thin Solid Films 65, 221 (1980)

17. Walker P.L. Jr., F. Rusinlo Jr., F. Rakszawaki, and L.M. Liggett, "Proceedings of the Third Conference on CArbon: Pergamon Press N.Y. P. 643 (1958)

18. Smith, W. R. and M. H. Polley, J. Phys. Chem. 60 689 (1956)

19. Essenhigh, R.H., p.1175

20. Walker, P. L. Jr., F. Rusinko Jr., and L.G. Austin, in "Proceedings of the Fourth Conference on Carbon", Pergamon Press Ltd., N.Y. p. 79 (1960)

21. Walker, P.L., Jr., Rusinko, Jr. and Austin, L. G., Gas reactions of carbon, Advances in Catalysis D. D. Eley, P. W. Selwood and P. B. Weisz (Eds) Vol. XI, P. 133, Academic Press, New York (1959)

22. Ayling, A. B. and Smith, I. W., Combust. Flame 18, 173 (1972)

23. Arthur J., Trans. Faraday Soc. 47, 164 (1956)

24. Rossberg M., Z. Elektrochem. 60, 952 (1956)

25. Bonnetain L., Duval X. and Letort M., Proc. Fourth Carobon Conf., p. 107. Pergamon Press, Oxford (1960)

26. Otterbein M. and Bonnetain L., Carbon 6, 877 (1968)

27. Phillips, R, Vastola F. J. and Walker P. L., Jr, Carbon 8 205 (1970)

28. Tognotti, L., Longwell, J. P. and Sarofim, A. F. Sarofim, Summitted to Twenty Third Symposium (International) on Combustion (1990)

29. Mulcahy, M.F.R. and Smith, I.W., Rev. Pure Appl. Chem. 19, 81 (1969)

30. Suuberg, E. M., Wojtowicz and Calo, J. M, Submitted for Presentation at the Twenty-Second International Symposium on Combustion (1988)

31. Blyholder, G. and Eyring, H., J. Phys. Chem. 63, 1004 (1959)

32. Gulbransen, E. A. and Andrew, K. F., Ind. Engng. Chem. 44, 1034 (1952)

33. Marsh, J., O'Hair, T. E. and Wynne-Jones, L. Carbon 7, 555 (1969)

34. Walker, P. L., Jr., Vastola, F. J. and Hart, P. J., Oxygen-18 tracer studies on the cabon-oxygen reaction, Fundamentals of Gas-Surface Reactions, p. 307, Academic Press, New York (1967)

35. Vastola, F. J., Hart, P. J. and Walker, P. L., Jr., Carbon 2, 65 (1964)

36. Laine, N. R., Vastola, F. J. and Walker, P. L., Jr., J. Phys. Chem. 67, 2030 (1963).

37. Hayward, D. O. and Trapnell, B. M. W., Chemisortion, Butterworths, London (1964).

38. Mattson, J. S. and Mark, H. B., Jr., Activated

39. Blackwood, J. D. and McTaggart, F. K., Aust. J. Chem. 12, 533 (1959)

40. Ahmed, S., Back, M. H. and Roscoe, J. M., Combustion and Flame, 70, 1 (1987).

41. Ahmed, S and Back, M. H., Carbon, 23 (5), 513 (1985).

42. Khan, M. R., Combust. Sci. and Tech., 65, 195 (1989)

43. Walker, P. L., Jr., Shelef, M. and Anderson, R. A. "Catalysis of Carbon Gasification" in Chemistry and Physics of Carbon, P. L. Walker, Jr. (editor), 4, 287 Marcel Dekker, New York (1968).

44. Wen, W. Y., Catal. Rev Sci. and Eng. 22 (1), 1 (1980)

45 Wood, B. J. and Sancier, K. M., "The Mechanisms of the Catalytic Gasification of Coal Char: A Critical Review", Final Report to U. S. Dept. of Energy, Morgantown Energy Technology Center, Morgantown, W. Va. (1984)

46. Amariglio, H. and Duval, X., CArbon, 4 323 (1966).

47. March, H. and Adair, R. R., Carbon, 13, 327 (1975).

48. Mckee, D. W., Carbon, 8, 623 (1970)

49. Floess, J. K., Ph. D. thesis, Dept. of Chemical Engineering, MIT, 1986.

50. Radovic, L. R., Walker, P. L., Jr., and Jenkins, Fuel, 62, 209 (1983).

51. Harker, H., Horsley, J. B., and robson, D., J. Nucl. Mater., 37, 331 (1970).

52. Long, F. J. and Sykes, K. W., J. Chem. Phys., 47, 361 (1950).

53. Mckee, D. W., Fuel, 62, 170 (1983).

54. Mckee, D. W., Carbon 17, 419 (1979).

55. Mckee, D. W., Fuel, 59, 308 (1980).

56. Radovic, L. R., Walker, P. L., Jr., and Jenkins, R. G., J. of Catalysis, 82 382 (1983).

57. Mims, C. A. and Pabst, J. K. "Alkali Catalyzed Carbon Gasification II. Kinetics and Mechanism" ACS Div. of Fuel Chem., 25, 258 (1980a).

58. Mims, C. A. and Pabst, J. K. "Alkali Catalyzed Carbon Gasification II. Kinetics and Mechanism" ACS Div. of Fuel Chem., 25, 263 (1980b).

59. Mims, C. A., Rose, K. D., Melchior, M. T. and Pabst, J. K., J. Amer. Chem. Soc. 104, 6886 (1982)

60. Kimberly Ellen Ritrievi, Sc. D. Thesis, Dept. of Chem. Eng., MIT, 1984.

61. Hurt, R., Personal Communication (1986).

62. Eckert, E. R. and Drake, R. M., "Analysis of Heat and Mass Transfer" McGraw Hill, New York (1972).

63. Wigmans, T. V., Cranenburgh, H., Elfring, R., and Moulijn, J. A., Carbon, 21 (1983).

64. Hurt, R. H., Ph. d. Thesis, Dept. of Chemical Eng., MIT, 1987

65. Spencer, W. B., Amberg, C. H. and Beebe, R. A., J. Phys. Chem., 62, 719 (1958).

66. Wicke, B. G. and Grady, K. A., Carbon, 25 (6), 791 (1987).

67. Heckman, F. A. and Harling, D. E., Rubber Chemical Technology, 39, 1 (1966).

68. Kelemen, S. R. and Freund, H., ENERGY & FUELS, 2 (2), 111 (1988).

69. Kyotani, T., Zhang, Z. G., Hayashi, S. and Tomita, A., ENERGY & FUELS, 2 (2), 136 (1988).

70. Kapteijn, F., Porre, H. and Moulijn, J. A., AIChE. J., 32 (1986).

71. Hermann, G. and Huttinger, K. J., FUEL, 65, 1410 (1986).

72. Howard, J. B., "Chemistry of Coal Utilization", 2nd Supplementary Volume, Edited by Elliott, Ch. 12, 733 (1962).

73. Pitt, G. J., FUEL, 41, 267 (1962).

74. Suuberg, E. M., COMBUSTION & FLAME, 50, 243 (1983).

75. Wornat, M. J., M. S. Thesis, Dept. of Chemical Eng., MIT, 1983.

76. Gavalas, G. R., Cheong, P. H., and Jain, R., Ind. Eng. Chem. Foundam, 20, 113 (1981).

77. Niksa, S. and Kerstein, A. R., COMBUSTION & FLAME, 66, 95 (1986).

78. Bender, C. M., and Orszag, S. A., "Advanced Mathematical Methodes For Scientists and Engineers" , 266 (1978).

79. Mims, C., Personal Communication, (1988).

80. Smith, I., Personal Communication, (1989).

81. Lussow, R. O., Vastola, F. J., and Walker, P. L., Jr., Carbon, 5, 591 (1967).

82. Froment, G. F. and Bischoff, K. B., "Chemical Reactor Analysis and Design", John Wiley & Sons, New York, 1979.